ADVANCED HEALTHCARE MATERIALS
www.advhealthmat.de

The Progress and Prospect of Zeolitic Imidazolate Frameworks in Cancer Therapy, Antibacterial Activity, and Biomineralization

Aziz Maleki, Mohammad-Ali Shahbazi, Vajiheh Alinezhad, and Hélder A. Santos**

The progressive development of zeolitic imidazolate frameworks (ZIFs), as a subfamily of metal-organic frameworks (MOFs), and their unique features, including tunable pore size, large surface area, high thermal stability, and biodegradability/biocompatibility, have made them attractive in the field of biomedicine, especially for drug delivery and biomineralization applications. The high porosity of ZIFs gives them the opportunity for encapsulating a high amount of therapeutic drugs, proteins, imaging cargos, or a combination of them to construct advanced multifunctional drug delivery systems (DDSs) with combined therapeutic and imaging capabilities. This review summarizes recent strategies on the design and fabrication of ZIF-based nansystems and their exploration in the biomedical field. First, recent developments for the adjustment of particle size, functionality, and morphology of ZIFs are discussed, which are important for achieving optimized therapeutic/theranostic nanosystems. Second, recent trends on the application of ZIF nanocarriers for the loading of diverse cargos, including anticancer medicines, antibiotic drugs, enzymes, proteins, photosensitizers, as well as imaging and photothermal agents, are investigated in order to understand how multifunctional DDSs can be designed based on the ZIF nanoparticles to treat different diseases, such as cancer and infection. Finally, prospects on the future research direction and applications of ZIF-based nanomedicines are discussed.

1. Introduction

Unprecedented advantages of nanomaterials have introduced them in recent decades as a potent platform in biomedicine, which can play a vital role in the therapy and diagnosis of many diseases.[1] For example, biomedical applications of porous materials, such as metal-organic frameworks (MOFs) have extensively been explored with the aim of fabricating novel drug formulations with better biological performance as compared to conventional medicines.[2–4] Zeolitic imidazolate frameworks (ZIFs) are a subfamily of MOFs with desirable properties, including high porosity, excellent thermal and mechanical stability, tunable surface properties, and exceptional chemical stability as a result of high resistance to alkaline water and organic solvents.[5] These features have made ZIFs excellent candidates for many applications, such as gas capture,[6] separations,[7] chemical sensors,[8] drug delivery,[9] and catalysis.[10] From a structural point of view, ZIFs are constructed by coordination between M^{2+} cations and imidazole (Im) anions, in which Im acts as a linker to create connecting bridges among the metal centers of $M(Im)_4$ tetrahedral units.[5,11] ZIFs are mainly prepared by solvothermal methods in both organic[5,12] and aqueous solutions.[13] Linker modifications or encapsulation of guest species (e.g., nanoparticles (NPs)) within ZIFs have been commonly employed to control the functionality of ZIFs. In addition, the pore size of ZIFs is simply tunable

Dr. A. Maleki, Dr. M.-A. Shahbazi, V. Alinezhad
Department of Pharmaceutical Nanotechnology
School of Pharmacy
Zanjan University of Medical Sciences
Zanjan 45139-56184, Iran
E-mail: maleki@zums.ac.ir
Dr. A. Maleki
Zanjan Pharmaceutical Nanotechnology Research Center (ZPNRC)
Zanjan University of Medical Sciences
Zanjan 45139-56184, Iran

Dr. M.-A. Shahbazi, Prof. H. A. Santos
Drug Research Program
Division of Pharmaceutical Chemistry and Technology
Faculty of Pharmacy
University of Helsinki
Helsinki FI-00014, Finland
E-mail: helder.santos@helsinki.fi
Prof. H. A. Santos
Helsinki Institute of Life Sciences
HiLIFE
University of Helsinki
Helsinki FI-00014, Finland

The ORCID identification number(s) for the author(s) of this article can be found under https://doi.org/10.1002/adhm.202000248

DOI: 10.1002/adhm.202000248

that, in turn, results in adjustable molecular diffusion/mass transfer and loading of large cargoes.[14,15] This unique property has greatly expanded the application of ZIFs in catalysis science and drug delivery.[16,17] The crystal size and morphology of ZIFs can also be controlled by the type of solvent and metal salt during the synthesis process, the ratio of metal salt to Im linker, the mixing order of the ZIF precursors, and the addition of surfactants.[16] The stability of ZIFs under physiological conditions and their pH-dependent degradability under acidic conditions make this type of MOFs highly attractive for the construction of pH-responsive drug delivery systems (DDSs).[17,18] As a result of the mild acidic condition of the tumor microenvironment (TME), ZIFs, especially ZIF-8, have been extensively investigated as nanocarrier both in vitro and in vivo for cancer ablation.[9,19–21] Furthermore, plenty of research efforts have been devoted to designing novel multifunctional ZIF-based composites both in cancer therapy[22–25] and also in antimicrobial applications,[26–28] bioimaging,[29–31] and theranostics (**Scheme 1**).[24] In the case of ZIF-8, as one of the main subgroups of ZIF nanomaterials, its versatile applications is mainly due to the facile polymerization of Zn^{2+} and 2-methylimidazole (2-MeIm) around various objects, including drugs,[19,32,33] NPs,[34–38] and bio-macromolecules[39,40] to render them multifunctionality while preserving structural crystallinity and porosity of ZIF shell.[39,41]

It deserves to be pointed out that there are many excellent reviews summarizing the state of the art of the development of MOFs and their applications for therapeutic, imaging, and sensing purposes.[4,17,42–47] However, there is no comprehensive literature review with a focus on the biomedical applications of ZIFs.[11,21,48] In this review, we discuss the synthesis and functionalization of ZIFs and then highlight the most recent progresses on DDSs developed by this type of porous nanostructures for chemotherapy (CT), photothermal therapy (PTT), photodynamic therapy (PDT), antimicrobial applications, development of theranostic nanomedicines, and biomimetic mineralization (Scheme 1). In addition, recent remarkable advances on ZIF-derived nanocomposites with particular emphasis on the multifunctional property of the nanocomposites in the treatment and diagnosis of hard-to-treat diseases are discussed, along with addressing critical challenges and perspectives of these materials. We expect that this review can boost the knowledge of the research community on the potential of ZIFs in biomedicine and its further exploration to introduce novel nanomedicines.

2. An Overview on the Synthesis, Properties, and Functionalization of ZIFs

ZIFs, which are very similar to aluminosilicate zeolites, are built up tetrahedral transition metals ions, i.e., Co^{2+}, Zn^{2+}, Cu^{2+}, or Fe^{2+}, and Im linkers where Im units make the bridges for connecting the metal centers.[5,11,48–51] For example, ZIF-8[5,48] and ZIF-67[52] have been constructed by the coordination between 2-MeIm and cationic ions of Zn^{2+} and Co^{2+}, respectively. ZIF-4,[5] ZIF-7,[5] and ZIF-90[53] have also been prepared by Zn^{2+}-Im, Zn^{2+}-benzimidazole, and Zn^{2+}-imidazole-2-carboxaldehyde, respectively.

Aziz Maleki received his Ph.D. degree in organic chemistry from the Institute for Advanced Studies in Basic Sciences, Zanjan, Iran. He then worked as a postdoctoral fellow in Zanjan University of Medical Sciences. Currently, he is an assistant professor at Department of Pharmaceutical Nanotechnology, School of Pharmacy, Zanjan University of Medical Sciences, Iran. His research interests focus on the fabrication and characterization of novel mesoporous and 2D materials for catalytic and biomedical applications.

Mohammad-Ali Shahbazi received his Ph.D. in 2015 from University of Helsinki, Finland, where he worked on porous materials for drug delivery to cancer tissues. He is currently a postdoc scientist at Faculty of Pharmacy, University of Helsinki, working on therapeutic microdevices for autoimmune diseases. He is an expert in oral peptide delivery and fabrication of cell-mimicking carriers. His current research interest lies in nano-based regenerative hydrogels for wound healing, bone repair and long-term drug delivery.

Hélder A. Santos obtained his Doctor of Science in Technology (Chemical Engineering) in 2007 from the Helsinki University of Technology. Currently, he is an associated professor at the Faculty of Pharmacy, University of Helsinki, and Head of the Nanomedicines and Biomedical Engineering research group. His scientific expertise lies in the development of nanoparticles/nanomedicines for biomedical applications, particularly porous silicon and polymeric-based nanomaterials, for simultaneous controlled drug delivery, diagnostic, and therapy for cancer, diabetes, and cardiovascular diseases.

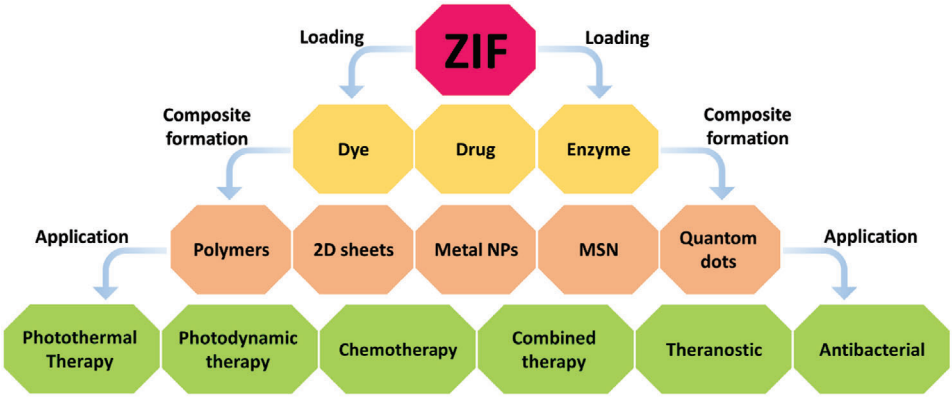

Scheme 1. An overview of the ZIF-based DDSs for biomedical applications. ZIF NPs can be used for the loading of the various molecules or the fabrication of nanocomposites. For example, polymers or mesoporous silica NPs (MSNs) can be used for the preparation of core-shell nanosystems.

These porous nanostructures have been prepared by hydrothermal or solvothermal methods in organic solvents, such as dimethylformamide (DMF)[5] and methanol,[12] or even in aqueous solutions[13] with reaction temperatures ranging from room temperature up to 200 °C, and reaction times from hours to days.[50] Although hydrothermal/solvothermal methods are commonly used to prepare ZIF-based nanostructures, which are simple and easy, scaling-up of such methods is hard and yield of the products is low.[49] To overcome the shortcomings, sonochemical[54] and mechanochemical[55] methods have been used to increase the yield of ZIF production. Nevertheless, due to a high variety of controllable parameters, including synthesis routes, concentration, and molar ratio of reactants, reaction temperature, solvents, and reaction time, there is a long way to industrialize the production of ZIF-8 and other members of the large family of ZIFs. In addition, the synthesis factors for the scale-up production of ZIFs are so far only partially investigated.[49] Green and sustainable production of ZIFs under mild synthesis conditions and the use of nontoxic solvents[13] and solvent free methods[56,57] are very crucial from environmental protection point of view. For example, in 2017, a fast and scalable method for the synthesis of hierarchical ZIFs, i.e., ZIF-8 and ZIF-67, and one-pot encapsulation of dyes or proteins cargoes using an organic base trimethylamine (TEA) was reported by Zou and co-workers[58] The addition of TEA into the solution of $Zn(NO_3)_2 \cdot 6H_2O$ promoted the formation of ZnO NPs, which rapidly transformed to ZIF-8 NPs after the addition of the 2-MeIm as the linker.

It should be noted that among the family of ZIFs, ZIF-8 is one of the main members that has been intensively used in many applications, such as adsorption, catalysis, electrochemical energy storage, gas separation, drug delivery, sensing, and electronics.[11,21] It has a sodalite-type framework with Zn^{2+} linked by 2-MeIm containing cages of 11.6 Å in diameter, which are accessible through a narrow six-ring pore (3.4 Å), creating an intrinsic porosity, which subsequently renders very large surface area of 1630–1700 $m^2\ g^{-1}$ to the ZIF-8.[5] As a result of the ultrahigh thermal stability (stable up to 550 °C under an inert atmosphere), ZIF-8 is capable of maintaining its original structure in boiling water/organic solvents for 7 days, and even it is stable in 8 M of NaOH (aq) at 100 °C for 24 h.[5]

The functionality of ZIF-based nanomaterials can be controlled by different strategies, including the modification of linker or encapsulation of guest species, such as diverse drugs, imagining agents, metal and metal oxide NPs or biomolecules within ZIFs.[11,59] As an example, Lu et al.[38] reported a controlled encapsulation strategy to incorporate various surfactant-capped NPs with different sizes, shapes, and compositions into the ZIF-8 NPs. Interestingly, by adjusting the time of NP addition during the ZIF formation, the spatial distribution of the NPs within ZIF-8 crystals was tunable. **Figure 1** shows how adjusting the addition time and sequence (at the beginning (T_0) or after a certain time (T) during the growth process of ZIF-8) can affect the spatial distribution of polyvinylpyrrolidone (PVP)-modified Au nanoparticles (AuNPs) inside the ZIF-8 crystals. A similar concept has been applied for the fabrications of various core/shell nanocomposites as nanotheranostic systems to simultaneously diagnose and treat hard-to-treat diseases that have been discussed in the next sections.[60,61]

It is also possible to coat the surface of ZIFs with stimuli-responsive gatekeepers to precisely control the release of encapsulated drugs in response to pH, light or reducing agents to improve therapeutic efficiency of ZIFs.[21] Ren et al. developed a pH- and redox-responsive DDS with doxorubicin (DOX)-loaded ZIF-8 as core and disulfide-doped organosilica as the shell.[62] The degradation of organosilica shell was confirmed via the breaking down of S–S bond in the presence of tripeptide glutathione (GSH) as a reducing agent, which is at elevated concentrations in the cytoplasm of tumor cells. In vivo studies showed that this DDS exhibited negligible hemolytic toxicity and significantly enhanced therapeutic efficiency against tumor growth compared to the free DOX. This work also stands as a pioneering strategy that opens new opportunities in design and fabrication of multifunctional and stimuli-responsive DDSs based on ZIFs in cancer treatment and diagnosis.

Although flexibility, structural diversity, mechanical and thermal stability, as well as control over shape and size of the ZIFs have held great promise in many applications, microporous pores of ZIFs unfavorably restrict fast molecular diffusion and mass transfer, thus limiting their utilities in catalysis, drug delivery, and other applications.[11] Therefore, the fabrication of mesopores or hierarchical porosity (a mixture of micro and mesopores) in ZIFs would markedly expand their applications as hosts to accommodate larger bulky molecules via quick diffusion inside the porous structures.[63–69] For example, hierarchical ZIF-8 NPs based on surfactant–amino acid co-templating

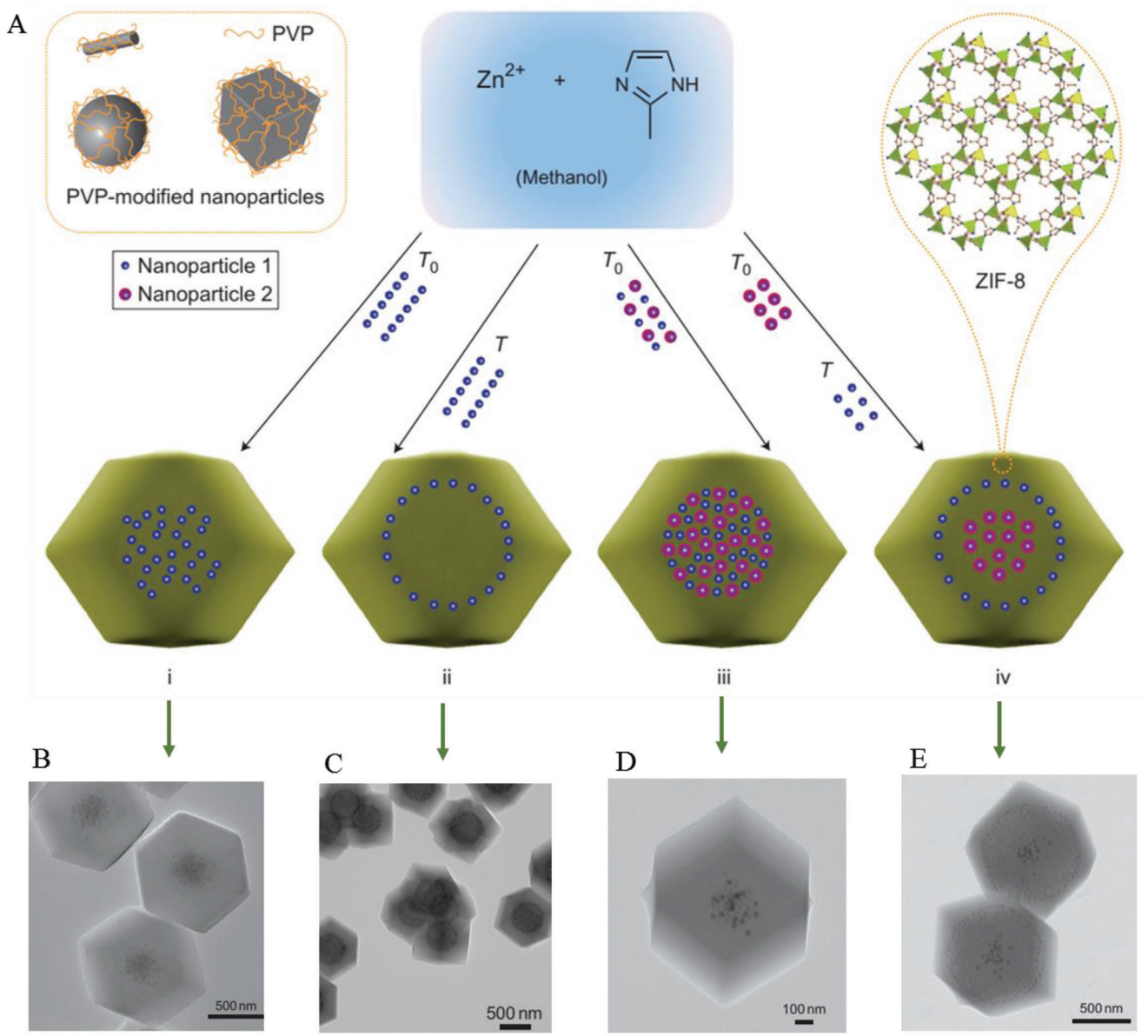

Figure 1. A) Schematic representation of controlled encapsulation of PVP-functionalized NPs with various sizes, shapes, and compositions into ZIF-8 crystals. The spatial distribution of the NPs within ZIF-8 crystals can be controlled by their addition sequence (i.e., addition at the beginning (T_0) or after a certain time (T) during the ZIF-8 synthesis). Spatial distributions of i) a single NP in the central areas ii) or off the central areas of the ZIF crystals, iii) two types of NPs in the central areas, or iv) one type in the central area but the other type in the transition layers of the ZIF crystals. B) The TEM image of the intermediate product of AuNP/ZIF-8 crystals collected after 3 h of reaction (case (i) in (A)). C) Hybrid crystals obtained when AuNPs were introduced 15 min after the initiation of the reaction (case (ii) in (A)). D) The hybrid crystal that consists of homogeneously distributed 13 nm Au and 34 nm AuNPs in the central area, prepared by simultaneously adding of two types of the NPs at the beginning of the reaction (case (iii) in (A)). E) Hybrid crystals that contain 34 nm AuNP-rich cores, 13 nm AuNP-rich transition layers and NP-free shells obtained by sequentially adding 34 nm AuNPs at the beginning of the reaction and 13 nm AuNPs after 40 min (case (iv) in (A)). Reproduced with permission.[38] Copyright 2012, Springer Nature.

strategy were prepared in aqueous solution by Wu et al.[68] They showed that cetyltrimethylammonium bromide (CTAB), as structure-directing agent to form micelles, was not inducing the generation of mesoporous structure, because the hydrated zinc ions were unable to produce strong interactions with the micelles. In contrast, in the presence of histidine aminoacid, the interaction between the ZIF-8 precursors and CTAB micelles was mediated by the amino acid, thus promoting the formation of ZIF-8 network, which had mesopores interconnected by micropores. Encapsulation of NPs within ZIFs and subsequent etching is another strategy to create hierarchical macro-microporous structures.[67,69] Based on this, polystyrene spheres (PSs) as sacrificial NPs, which can dissolve in the methanolic solution, were utilized to synthesize macro-microporous ZIF-8 with cheese-like morphology. The concentration and addition time of the encapsulated PSs were detrimental in controlling the ratio of the

macropores. The introduction of the NPs into the ZIF matrix did not change the well-defined crystal structure of the synthesized ZIF-8.[69]

For many biomedical applications, the crystal size and morphology of ZIFs are detrimental factors.[4,11,70] The type of solvent,[53,71] metal salts,[72–74] the ratio of metal salt to 2-MeIm,[75] the mixing order of the ZIF precursors,[74] and the addition of surfactants or capping agents[76] have been reported as important factors to control the crystal size of ZIFs.[16] It has been shown that the reactivity of the zinc salt in the growth solution has had a significant impact on the size of the ZIF-8 crystals.[73,74] Small size ZIF-8 crystals (≈50–200 nm) have been harvested by using reactive zinc salt precursors, including zinc(II) acetylacetonate [$Zn(acac)_2$], zinc nitrate ($Zn(NO_3)_2$), zinc sulfate ($ZnSO_4$) or zinc perchlorate ($Zn(ClO_4)_2$), while nonreactive salts, such as zinc chloride ($ZnCl_2$), zinc acetate ($Zn(OAc)_2$) or zinc iodide (ZnI_2) produced ZIF-8 crystals with larger sizes ranging from ≈350 to 650 nm.[72] This was mainly due to the nucleation rate of ZIF crystals, which was controlled by the coordination speed between the metal ions and the 2-MeIm linker.[74] In fact, the solvation of reactive salts (e.g., $Zn(NO_3)_2$) in methanolic solution is relatively weak. Therefore, the Zn^{2+} ions can be rapidly coordinated by 2-MeIm, leading to fast nucleation and subsequent generation of small-sized NPs. Pan et al.[76] used the surfactant of CTAB as a capping agent to control the size of ZIF-8 nanocrystals. The particle sizes were precisely tuned from ≈100 nm to 4 µm by tuning of the CTAB concentration. This was attributed to the CTAB molecules that were adsorbed on the surface of ZIF-8 crystals in the growth solution and acted as capping agents to prevent further crystal growth.

In order to control the morphology of ZIF NPs, two strategies, i.e., nontemplated and template-mediated methods, have been developed.[11] In the nontemplated methods, different parameters, such as solvent, metal ion to 2-MeIm ratio, and reaction time have been determinant parameters in the morphology of ZIF NPs.[77–81] For example, ordered hierarchical ZIFs with nest-like morphology were prepared using a mixed solvent of methanol (CH_3OH) and aqueous ammonia ($NH_3 \cdot H_2O$).[77] The architectures with diameters of ≈2–3 µm were formed by self-assembly of numerous nanoplates with a thickness of ≈20–40 nm. Such structures were not produced in the presence of a single solvent. This study demonstrated that the type of solvent had a vital effect on the morphology of ZIFs. In contrast to the template-free approach, the template-mediated methods employ soft (e.g., CTAB[76]) or hard templates (e.g., PSs[82]) to control the crystal morphology of ZIF particles. CTAB, as a capping agent, was not only used to control the crystal size of ZIF-8,[76] but also showed that the increase in its concentration changed the crystal morphology from rhombic dodecahedron to truncated rhombic dodecahedron and then to truncated cubes. In fact, the CTAB molecules were adsorbed much more strongly on {100} faces of ZIF-8 than the other two faces, i.e., {110} and {111}, leading to the decrease of growth rate on the {100} face, thereby resulting in the transformation of crystal morphology.[76] Similarly, Hu et al.[83] obtained ZIF-67 nanocubes instead of the commonly observed polyhedrons in the presence of CTAB as a morphological modifying agent. Again, the formation of the new morphology was attributed to the preferential adsorption of CTAB on the hydrophobic surfaces.

Given that hollow metal–organic frameworks (HMOF) have hierarchical porous structures, accessible metal sites, and rapid mass transport property, these types of nano/microstructures have received great attention in many research fields, including catalysis, gas sensors, etc.[84] Generally, three main synthetic strategies have been developed for the construction of HMOFs, including the exterior-templating approach (sacrificial template fabrication technique), the self-templating method, and the two-phase interface method. There is a comprehensive review article describing the synthesis of HMOFs and their derivatives using the above-mentioned approaches.[84] Inspired by HMOFs, hollow ZIFs (HZIFs) have also been constructed utilizing the same strategies. For example, different types of HZIFs have been produced by the sacrificial template fabrication technique, in which the ZIF growth on the surface of a core template was followed by a removing step to eliminate the internal template.[82,85–87] In addition, it is imperative to functionalize the surface of the template prior to the ZIF growth process to enhance interaction between the ZIF precursor and the template surface and also to inhibit the competitive homogeneous self-nucleation of ZIFs in the solution. For example, carboxylate-terminated PSs have been utilized as a template for the construction of core–shell PS@ZIF-8 composites, followed by removing the PS cores using DMF as an etchant to obtain HZIF-8 microspheres.[85] This promising strategy will create great opportunities for fabricating novel HZIFs with diverse morphologies and unique properties in the near future.

In the self-templating method, which is carried out in the absence of any exterior template, the generated intermediate products during ZIF synthesis can act as a template and direct the formation of HZIFs.[84] In order to have better control over the formation process of HZIFs via the self-templating method, it is necessary to perform a surface protective modification on the intermediate products prior to the subsequent transformation reaction.[84] For example, Hu et al.[88] prepared HZIFs using phenolic acids (PAs), i.e., gallic acid and tannic acid (TA). They demonstrated that PAs not only acted as the surface protecting agents, but also served as an etching agent to create HZIF-8 without destroying the crystallinity of the parent ZIF. In fact, the outer shell of the ZIF-8 was protected by the PAs that blocked the exposed surface of ZIF-8 and the inner part was etched by free H^+ ions released by the PAs.[89] The HZIFs produced heat upon irradiating to the near-infrared (NIR) light (808 nm), potentially endowing them with photothermal therapy capability.[89] In the two-phase interface method, which is more convenient, the interface of two different phases is employed as a template for growing of ZIF at the interface. This method is classified into three categories: liquid–liquid, solid—liquid, and gas–liquid interface systems, which all have been reported for the synthesis of HZIFs.[66,90,91]

Although, there are successful achievements on controlling the pore size, diameter, morphology and surface properties of ZIFs, the reaction parameters have not been systematically optimized and there is no clear guideline for controlling the particle diameter, pore size, and morphology. In addition, most of the current studies have focused only on the ZIF-8. Therefore, further studies are needed on the physicochemical properties of other ZIFs rather than ZIF-8, because the developed techniques are still at an infancy stage. In this context, reproducibil-

ity, cost-effective preparation and environmental considerations of the synthesis methods must receive more attention in future studies.

3. ZIF NPs for pH-Responsive Therapy

The design and construction of novel DDSs have been grown in recent years with central attention devoted to new methods for developing stimuli-responsive DDSs.[92,93] Among different types of stimuli, such as temperature, electric field, light, and magnetic field,[94] pH-sensitive DDSs have been the main core of numerous investigations to develop responsive nanosystems, specifically for cancer therapy goals.[92] This is mainly due to the pH of tumor tissue (pH 5.5–6.0), which is more acidic than the blood and normal tissues (pH 7.4). Such nanosystems have been employed to transport toxic chemotherapeutic drugs to cancer site via blood circulation with minimum undesired drug release before reaching the cancer tissue.[92,95] However, many of the systems suffer from low drug-loading capacity, poor biocompatibility, undesirable biodegradability, and complicated synthesis procedures. As a result of the unique properties of MOFs, this type of porous materials has attracted great attention for achieving a controllable drug release.[4,17] Generally, the encapsulation of drug of interest into MOFs involves several steps, including synthesis of MOF carriers, removal of solvents from their pores, and finally loading of the cargos, which all together make the whole process costly and complicated.[96] Furthermore, the small pore apertures of MOFs limits the entering of large cargoes within the network of MOF.[42,44,97] Recently, ZIFs have successfully been used as drug carriers in the construction of varied DDSs that can load a range of cargos from small molecule drugs to large bio-macromolecules, such as enzymes and proteins for pH-responsive drug delivery (**Table 1**).[9,18,21,98]

In this section, we provide the most significant signs of progress in the development of simple ZIF-based DDSs in cancer therapy, antibacterial applications, and biomineralization. ZIFs loaded by a cargo, and/or in some cases functionalized by small molecules and polymers, e.g., polyethylene glycol (PEG), are discussed. The components, structures, and properties of ZIFs are highlighted in different examples. In addition, the impact of the ZIF framework, especially the degradation of the network in acidic environments, is discussed along with benefits and critical challenges of each system. In contrast, Section 4 has a focus on the complex multifunctional DDSs derived from ZIF-based composites, integrated/functionalized by some metal NPs, nanorods, mesoporous silicas, quantum dots, polymers, or graphene to form core@shell or hybrid structures for various biomedical applications.

3.1. Applications of ZIF NPs in Cancer Therapy

For the first time, Sun et al.[9] demonstrated that ZIF-8 could be used for the delivery of anticancer drugs in vitro. Remarkable loading of 660 mg of 5-FU in 1 g of ZIF-8, and pH-triggered controlled release of the drug, which was much faster in acidic condition (pH 5) than neutral one (pH 7.4), were observed, suggesting ZIF-8 as an excellent pH-sensitive DDS.[9] However, as the pore window of ZIF-8 is 3.4 Å, this structural feature limits the entrance of large molecules inside the pores, thus leading to low cargo loading within the pores and burst release, as a result of drug adsorption on the surface of the particles.[37,119] In order to tackle this hurdle, a simple process that combined ZIF synthesis and cargo encapsulation in a one-pot manner was reported by Zheng et al.[100] In this process, the anticancer drug DOX and three organic dyes, were successfully encapsulated within ZIF-8 and ZIF-67 with high cargo loading (14–20 wt%). Firstly, the metal ion and dye/drug molecules self-assembled to form coordination polymers. After the addition of the organic linkers, the coordination polymers disassembled, and thus, the subsequent generation of ZIF network caused to encapsulating of target molecules within the ZIF hosts. The drug/dye-loaded crystals possessed hierarchical pore structures containing ordered micropores and homogeneously distributed mesopores filled by the guests. Interestingly, hierarchical micro and mesoporous ZIF-based structures were harvested by the removal of the organic drug/dyes from the pores. DOX-loaded-ZIF-8 showed pH-responsive release behavior, in which the drug was not released under physiological condition (pH 7.4), while the release of the drug occurred in a controlled manner at lower pH values of 5.0–6.5. Cytotoxicity assays on breast cancer cell lines showed that the DOX@ZIF-8 had higher toxicity than that of free DOX.[100] In a different study on the controlled release behavior of DOX-loaded into ZIF-8 and ZIF-7, it was shown that ZIF-8 released the drug in a more controlled manner than ZIF-7 under acidic condition, demonstrating that ZIF-7 was more stable at acidic pH than the ZIF-8 carrier, highlighting the effect of ZIF type in the design of controlled DDSs.[20]

Despite excellent advantages of ZIFs, low dispersity, cytotoxicity, and aggregation of the MOFs under physiological condition, nonactive targeting capability, and concerns related to its favorable biocompatibility have seriously limited their in vivo applications.[102,120,121] In order to overcome these limitations, several studies have been demonstrated the surface functionalization of the ZIFs by folic acid (FA)-PEG,[108,110] hyaluronic acid (HA),[105] phenolic lipid,[120] peptide,[122] and phospholipid bilayer.[102] HA, a targeting ligand of the CD44 receptor, is overexpressed in many growing tumor cells. This ligand was attached on the surface of curcumin (CCM)-loaded ZIF-8 through coordinative interaction to promote the cellular uptake of NPs. The surface modification endowed the nanocomposite (CCM@ZIF-8/HA) with active targeting ability and enhanced its biocompatibility. The CCM@ZIF-8/HA showed enhanced dispersity in phosphate buffer saline (PBS) and a long-term pH-responsive drug release behavior and successfully delivered CCM into cancer cells.[105] Efficient autophagy inhibition was observed by chloroquine (CQ), as autophagy inhibitor, -loaded ZIF-8 (CQ@ZIF-8) after functionalization by methoxy FA-PEG. Compared to healthy cells (HEK293 cells), the cancer cells (HeLa cells) showed lower viabilities when treated with FA-PEG/CQ@ZIF-8 NPs, demonstrating targeting ability of FA and inhibiting the process of autophagy flux in the cancer cells, as well as the formation of autophagosome more effectively than the free CQ and CQ@ZIF-8.[108]

Table 1. Summary of ZIF-based pH-responsive DDSs.

Type of ZIF and surface ligand	Encapsulated Cargo	Size [nm/μm]; Zeta potential [mV]	Cells and animal models	Main conclusion	Ref.
ZIF-8	5-FU	Before loading: <200 μm	ND	– The first example of the application of ZIFs in DDSs. – Remarkable capacity for the 5-FU loading. – pH-triggered 5-FU release for cancer chemotherapy.	[9]
ZIF-8	CPT and FES	Before FES loading: 70 nm; +31.4 mV After FES loading: 70 nm; +31.0 mV	In vitro: Epithelial MCF-7 breast cancer cells	– Moderate cytotoxicity of the ZIF-8 NPs which was comparable to other organic and inorganic drug carriers. – pH-triggered disintegration of the ZIF-8 NPs in acidic condition. – The versatility of the fabrication method for the encapsulation of the organic dyes, anticancer drugs, and magnetic NPs within the ZIF-8 NPs. – Increased cell death by CPT-loaded ZIF-8 as compared to the free CPT.	[18]
ZIF-8	Caffeine	Before loading: 200–300 nm; ND After loading: 200–300 nm; ND	ND	– One-step, in situ encapsulation of caffeine within ZIF-8 NPs – High caffeine loading (≈28 wt% in only 2 h at 25 °C).	[99]
ZIF-8	CCM	Before loading: ND; +4.4 mV After loading: 119.3 ± 13.6 nm; +4.3 mV	In vitro: HeLa cell line In vivo: U14 cervical cancer model	– CCM-loaded ZIF-8 NPs possessed good chemical stability, high drug encapsulation efficiency (88.2%), and fast drug release in tumor acidic media. – Higher cytotoxicity of CCM-loaded ZIF-8 NPs than free CCM both in vitro and in vivo.	[19]
ZIF-8 and ZIF-67	DOX and dye molecules	Before loading: ND After DOX loading within ZIF-8: nm 70–300 nm; +30.1–+31.1 mV	In vitro: Epithelial MCF-7 breast cancer cells, epithelial MDA-MB-231, and MDA-MB-468	– A novel approach combining ZIF synthesis and cargo (large drugs and dye molecules) encapsulation in a one-pot step. – Efficient cancer therapy using DOX-loaded ZIF-8 through a pH-responsive drug release.	[100]
ZIF-7 and ZIF-8	DOX	ND	ND	– Successful encapsulation of DOX within ZIF-7 and ZIF-8. – When pH increased from physiological condition to acidic condition, ZIF-7 remained intact whereas ZIF-8 released DOX in acidic condition.	[20]
ZIF-8	5-FU	Before loading: ≈200 nm; +21.0 mV	In vitro: Epithelial HepG2 cells, epithelial 4T1 cells, and epithelial MCF-7 breast cancer cells In vivo: 4T1 mammary gland breast cancer model	– Concentration and time-dependent cellular uptake of ZIF-8 NPs was affected by the particle size of the NPs, but not by drug loading. – Clathrin and macropinocytosis-mediated pathways were involved in the cellular uptake of the ZIF-8-NPs. – The unexpected high concentration of ZIF-8 NPs was found in lung, probably due to the particle size. – At the normal doses, ZIF-NPs exhibited acceptable biocompatibilities, and minimal effects on the renal and liver functions, inflammatory factors, and immune cells. – 5-Fu-loaded ZIF-8 NPs significantly improved the therapeutic outcome in a mouse model with tumor lung metastasis.	[70]
ZIF-8	CCM	Before loading: 140 ± 5 nm; +7.40 mV After loading: 145 ± 5 nm; +7.22 mV	In vitro: HeLa cell line	– ZIF-8 NPs exhibited ultrahigh CCM encapsulation efficiency (≈83.33%) and good chemical stability. – Cellular internalization of CCM-ZIF-8 in HeLa cells was confirmed by CLSM.	[101]
ZIF-4@DOPC	CCM	Before loading: 120 nm; −20.5 mV After loading: 141 nm; ND	ND	– The CCM-loaded ZIF-4@DOPC showed remarkable water dispersity and stability in PBS. – The ZIF-4@DOPC possessed high drug entrapment efficiency (80.8%) and the release of CCM from the carrier was pH-responsive.	[102]

(*Continued*)

Table 1. Continued.

Type of ZIF and surface ligand	Encapsulated Cargo	Size [nm/μm]; Zeta potential [mV]	Cells and animal models	Main conclusion	Ref.
ZIF-8	6-MP	Before loading: 516 nm; ND After loading: 566 nm; ND	ND	– Owing to the pH-degradability of ZIF-8 NPs in acidic condition, much faster 6-MP release occurred from the 6-MP@ZIF-8 in acidic pH as compared to the release medium with the pH value of 7.4.	[103]
PEG-FA-modified ZIF-8	DOX and VER	After loading: 185 nm; −34.5 ± 7.43 mV	In vitro: B16F10 melanoma cells and epithelial MCF-7 breast cancer cells In vivo: B16F10 melanoma model	– Successful co-delivery to overcome multidrug resistance (MDR) cancer. – Prolonged blood circulation and active targeting. – Desirable NIRF imaging	[33]
ZIF-8	CpG ODNs	Before loading: 342 nm; ≈+20 mV After loading: 396 nm; ≈+5 mV	In vitro: RAW264.7 macrophage cells In vivo: quantification of inflammatory cytokines in blood samples	– CpG ODNs-ZIF-8 complexes showed good stability in physiological condition and effective release of CpG ODNs in an acidic environment. – Intracellular uptake of CpG ODNs was significantly increased by ZIF-8 NPs in RAW264.7 cells, thus enhancing the secretion of immune cytokines both in vitro and in vivo, confirming potent immunostimulatory activity of the nanosystem.	[104]
HA/IM-modified ZIF-8	CCM	After loading: 159.2 nm; −28.1 mV	In vitro: HeLa cell line	– CCM-loaded HA/IM-modified ZIF-8 NPs exhibited enhanced dispersity in PBS, promoted cellular uptake, and higher growth inhibition against HeLa cells than the bare CCM@ZIF-8 NPs.	[105]
ZIF-8	MLT	Before loading: ≈100 nm; +13.8 mV After loading: ≈100 nm; +14.4 mV	In vitro: Epithelial A549 Cells and HeLa cell line In vivo: U14 cervical cancer model	– Loading into ZIF-8 NPs could reduce the undesirable hemolytic activity of the MLT. – Mechanistic investigations through transcriptome analysis showed that MLT@ZIF-8 NPs could regulate the expression of 3383 genes, and the PI3K/Akt-regulated p53 pathway, which involved in the apoptosis of A549 cells. – The MLT@ZIF-8 NPs showed enhanced anticancer activity than the free MLT in vivo.	[106]
AS1411 aptamer-modified ZIF-8	DOX	After loading: 100 nm; −10 mV	In vitro: HeLa and epithelial HEK 293T cells lines	– The DOX-loaded AS1411 aptamer-modified ZIF-8 DDSs could effectively escape from the endo/lysosomal vesicles due to the pH-triggered release of zinc ions and the ROS production, synergistically enhancing the cancer therapy.	[32]
RGD-modified ZIF-8	CPT	After loading: 100 nm; ≈+12 mV	In vitro: HeLa cell line	– The CPT-loaded RGD-modified ZIF-8 NPs exhibited favorable biocompatibility and excellent pH-responsive CPT release. – Intracellular ROS generation of the DDS enhanced cancer cell death in vitro.	[107]
PEG-FA-modified ZIF-8	CQ	After loading: 250 nm; −6.05 mV	In vitro: HeLa and epithelial HEK 293 cells lines	– Due to the targeting property of FA, the CQ-loaded PEG-FA-modified ZIF-8 (FA-PEG/CQ@ZIF-8) NPs reduced the viabilities of HeLa cells compared to the nontargeted counterparts. – The pH-responsive PEG-FA/CQ@ZIF-8 NPs could control the CQ release and enhanced the efficiency of the autophagy inhibition.	[108]
ZIF-8	3-MA	Before loading: 90 nm; 24.1 ± 5.5 mV After loading: 80 nm; 3.2 ± 2.2 mV	In vitro: HeLa cell line In vivo: cervical cancer HeLa model	– An effective autophagy inhibition and tumor targeting was mediated by encapsulating 3-MA, an autophagy inhibitor, into the ZIF-8 (3-MA@ZIF-8). – Compared to free 3-MA, the 3-MA@ZIF-8 NPs severely blocked autophagosome formation and autophagy flux. – More control over precise drug release and more efficient antitumor effect and autophagy inhibition was observed in the xenograft tumor model for the 3-MA-loaded ZIF-8 NPs.	[109]

(*Continued*)

Table 1. Continued.

Type of ZIF and surface ligand	Encapsulated Cargo	Size [nm/μm]; Zeta potential [mV]	Cells and animal models	Main conclusion	Ref.
PEG-FA-modified ZIF-8	PEGCG	After loading: 220 nm; −21.9 ± 0.36 mV	In vitro: Hela and epithelial HEK 293 cells	– Compared to free PEGCG, PEGCG-loaded PEG-FA-modified ZIF-8 NPs showed higher anticancer effect via excellent induction of autophagic death on tumor cells.	[110]
ZIF-8	Ceftazidime	ND	In vitro: Bacteria killing effect on *E. coli*	– Antibacterial properties of ceftazidime@ZIF-8 NPs were observed against *E. coli*. – Taking the advantage of the intrinsic emission properties of ZIF-8 NPs, for the first time, this study showed the internalization of the NPs using CLSM via 3D reconstructions of z-stacks.	[111]
ZIF-8	RFP and o-NBA	Before loading: ≈100 nm; +30.5 mV After loading: ≈200 nm; +27.0 mV	In vitro: killing effect of the NP on ampicillin-resistant *E. coli* and MRSA In vivo: Infected wound	– pH and light-triggered drug delivery. – High antibacterial effect through combination therapy. – Accelerated wound healing in vivo.	[26]
ZIF-8	Physcion	Before loading: 157 nm; +6.5 mV After loading: 165 nm; +6.5 mV	In vitro: Bactericidal effects on *P. Putida*, *E. coli*, engineered *E. coli* (QH4), and *S. Aureus*	– Compare to free PHY, PHY-loaded@ZIF-8 NPs showed maximum growth inhibition zones against both Gram-negative and Gram-positive strains.	[112]
ZIF-67 and Co-SIM-1	ND	Before loading for both ZIF-67 and Co-SIM-1: ≈2 μm; ND	In vitro: Bactericidal effects of the drug-loaded NPs on *S. cerevisiae, P. putida*, and *E. coli*	– The control release of metal endowed the DDSs with excellent antibacterial activities against gram negative bacteria.	[113]
FA-modified ZIF-8	Vancomycin	Before loading: 50 nm; ND After loading: 75 ± 10 nm; ND	In vitro: killing effect of the drug-loaded NPs on MDR *S. aureus* and *E. coli*	– The presence of FA on the surface of the vancomycin-loaded ZIF-8 NPs could significantly increase the effective uptake of the NPs into MDR *S. aureus* through endocytosis, thus enhancing antibacterial activity.	[114]
ZIF-8	Iodine	Before loading: 550 ± 103 nm; ND After loading: 530 ± 105 nm; ND	In vitro: Bactericidal effects of the drug-loaded NPs on *S. epidermidis*, *S. aureus*, and *E. coli*	– Due to the acid degradability of the ZIFs, both the Gram-negative and Gram-positive bacteria could be very effectively killed by the iodine-loaded ZIF-8 at pH 6.0, while at pH < 7.0, no appreciable antibacterial activity was observed.	[115]
ZIF-8	SQ	Before loading: 180 nm; ND After loading: 170 nm; ND	In vitro: Killing effect of SQ-loaded ZIF-8 (SQ-ZIF-8) NPs on MRSA	– SQ-ZIF-8 NPs produced cytotoxic ROS under red light irradiation (650 nm) through a pH-sensitive manner to kill MRSA bacteria, leading to complete loss of adherence of structurally robust bacterial biofilms.	[116]
ZIF-8	Indocyanine green	Before loading: ≈40 nm; ND After loading: ≈100 nm; ND	In vitro: Bactericidal effects of the drug-loaded NPs on MRSA In vivo: Infected skin	– Zinc ions released from ZIF network could inhibit bacterial growth by increasing the permeability of bacterial cell membrane. – Remarkable bactericidal activity was observed by the chemo-photothermal therapy in vivo.	[117]
Cu^{2+}-modified ZIF-8	CCM	Before loading: ≈100 nm; ND After loading: ≈200 nm; ND	In vitro: Killing effect of the drug-loaded NPs on *E. coli*	– ROS generation was boosted due to combined interactions of Zn^{2+} and Cu^{2+}. – CCM-loaded ZIF-8 NPs exhibited greater anti-biofilm and anti-bacterial effects than free CCM.	[118]

Abbreviations: 3-MA: 3-methyladenine; 5-FU: 5-fluorouracil; 6-MP: 6-mercaptopurine; CCM: curcumin; CDT: chemodynamic therapy; Co-SIM-1: cobalt-based substituted imidazolate material; CpG ODNs: CpG oligodeoxynucleotides; CPT: camptothecin; CQ: chloroquine diphosphate; DOPC: 1,2-dioleoyl-sn-glycero-3-phosphocholine; *E. coli*: *Escherichia coli*; FA: folic acid; FA-PEG: methoxy poly(ethylene glycol)-folate; FES: fluorescein; HA: hyaluronic acid; HA/IM: imidazole substituted hyaluronic acid; HeLa cell line: human epithelial carcinoma cells; MDR: multidrug resistance; MLT: melittin; MRSA: methicillin-resistant *Staphylococcus aureus*; ND: not determined; NIRF: near infrared fluorescent imaging; o-NBA: 2-nitrobenzaldehyde; PBS: phosphate buffer saline, *P. Putida: Pseudomonas putida*; PEGCG: epigallocatechin-3-gallatea palmitate; PEG-FA: methoxy poly (ethylene glycol)-folate; RGD: Arg-Gly-Asp; ROS: reactive oxygen species; *S. cerevisiae: Saccharomyces cerevisiae*; *S. aureus: Staphylococcus aureus*; *S. epidermidis: Staphylococcus epidermidis*; SQ: squaraine; VER: verapamil hydrochloride.

Surface chemical functionalization of ZIFS with safe materials can increase their biocompatibility; however, it might reduce pore sizes or even block the pores. Zhao and co-workers, used a mechanical ball-milling method to develop a surface defection strategy on the external surface of ZIF-8 to tune the hydrophobic–hydrophilic balance of ZIF-8, resulting in significantly higher cell viability without decreasing its cargo loading and release capacity.[123] In the mechanical ball-milling method, unsaturated Zn-sites and N-sites were created on the external surface of ZIF-8, leading to the binding of H_2O molecules on the surface and generating a hydrophilic surface that significantly improved cell viability of ZIF-8.

Horcajada and co-workers evaluated the cytotoxicity of a series of MOF NPs on two cell lines (J774 and HeLa) by the MTT assay and indicated that the cytotoxicity was strongly depended on the MOF composition since Fe-based MOFs exhibited less toxicity than the Zn- or Zr-MOF NPs.[121] Recent toxicological investigations suggested that toxicity of Zn was related to the high solubility of Zn^{2+} cations.[124] Therefore, the research group proposed that ZIF-8 NPs were progressively degraded into Zn^{2+} and 2-MeIm in cell culture media containing phosphates ions and in the acidic endosomal environment. The high toxicity of ZIF-8 was related to the competition of the released/dissolved Zn^{2+} with Fe^{2+} and Ca^{2+} ions through ion channels and/or DNA damage.[121] These observations highlighted the importance of surface modification of the ZIFs to overcome the toxicological concerns.

A series of pharmacokinetics and biodistribution studies of ZIF-8 NPs were conducted by Zhang and co-workers to understand biofate of the NPs within the body.[70] After intravenous administration to rats (32 mg kg^{-1}), the serum zinc concentration steadily declined over time and elimination half-life was 3.6 h with a clearance of 0.187 L h^{-1} g^{-1}. Low accumulation of Zn was detected in tissues, including the kidney, heart, brain, and testis (up to ≈25 µg g^{-1}). In contrast, ZIF-8 NPs were captured much more by reticuloendothelial system (RES) organs (up to ≈210, ≈35, and ≈32 µg g^{-1} in the lung, liver, and spleen, respectively). Unexpected accumulation of Zn in the lung was probably due to the particle size of the NPs. However, after 7 days, the concentration of Zn in the RES tissues decreased dramatically, suggesting the fast degradation and elimination of the NPs. In addition, around 65% and 12% of the NPs were eliminated by feces and urine within 7 days, respectively. Interestingly, due to the high pulmonary accumulation and fast elimination of the NPs, the 5-Fu-loaded ZIF-8 NPs had a significant therapeutic effect on a tumor lung metastasis bearing mouse model. Significant accumulation of ZIF-8@DOX in the lung was also reported by Cheng et al., which can be used for the chemotherapy of lung cancer.[125] This phenomenon was related to the aggregation of the NPs in the blood circulation, leading to the entrapment of the nanosystem in abundant capillaries of the lung. Interestingly, after coating of the NPs with 4T1 cancer cell membrane, accumulation in the lung was remarkably decreased, highlighting importance of the biomimetic coating in enhanced biocompatibility of the ZIF-based DDSs.

Although there are extensive studies on the applications of ZIFs in cancer diagnosis and treatment, the most attention has mainly focused on ZIF-8. In order to exploit other members of the ZIF family, Jiang et al.[126] synthesized nanoscale ZIF-90 with a negative zeta-potential, which exhibited better cell biocompatibility, mitochondria targetability, and in vivo survival rate compared to the ZIF-8 NPs with positive zeta-potential. In addition, in vivo toxicity studies confirmed the excellent biocompatibility of ZIF-90 and minimal side effects on the renal and liver functions. The surface of DOX-loaded ZIF-90 NPs was surface-modified by Y1 receptor ligand [Asn^6, Pro^{34}]-NPY (AP) to realize targeted adenosine triphosphate (ATP) and induce in vivo pH-responsive triple-negative breast cancer treatment. ATP-responsive property of the nanosystem was due to the stronger coordination between ATP and Zn^{2+} than the Im and Zn^{2+}, enhancing the therapeutic efficacy of the nanosystem in the killing of cancer cells. Naturally, the concentration of ATP in the tumor cells is ≈100 times higher than the normal cells, allowing the targeting of ATP for cancer therapy.[127,128]

Multidrug resistance (MDR) is one of the important hurdles inhibiting effective cancer chemotherapy.[129] This phenomenon mainly originates from either an acquired resistance in cancer cells by the stimulus of anticancer drugs to overexpress ATP-binding cassette (ABC) transporter (e.g., *p*-glycoprotein (*p*-gp)) or intrinsic high expression of ABC transporter proteins. This overexpressed transporter can efflux the chemotherapeutic drugs from the cytoplasm of cancer cells to reduce their accumulation within the cells, resulting in an extremely low therapeutic outcome.[130,131] To circumvent MDR, the combination of small molecule anticancer drugs or chemosensitizers with macromolecular therapeutic genes, in a single DDS is an efficient way to treat cancer.[130] As a result of the inherent biocompatibility and pH-degradability of ZIF-8, this porous material was employed to construct a co-delivery nanosystem containing DOX and verapamil (VER) to overcome MDR in tumor cells for achieving efficient in vivo cancer therapy.[33] The (DOX+VER)@ZIF-8 was further functionalized by methoxy poly FA-PEG to avoid aggregation of (DOX+VER)@ZIF-8 particles, and thus, prolonging its blood circulation as an active DDS (**Figure 2**A). VER, as a *p*-glycoprotein inhibitor, could reverse the drug resistance associated with *p*-glycoprotein, resulting in increased local concentrations of DOX in MDR tumor cells and improving the efficiency of the formulation. Transmission electron microscope (TEM) images showed that PEG-FA/(DOX+VER)@ZIF-8 particles had uniform spherical-like morphology and the diameter of the NPs was determined to be 185 nm with narrow size distribution (Figure 2B). For both DOX and VER, faster drug release in acidic condition (pH ≈ 5.0) compared to the neutral release medium (pH ≈ 7.4) was observed from the (DOX+VER)@ZIF-8 NPs, confirming the degradation of ZIF-8 in the acidic environment and drugs release acceleration. Cytotoxicity assay on B16F10 and MCF-7/A cells showed that the inhibition rates of PEG-FA/(DOX+VER)@ZIF-8 were higher than that of free drug of DOX and DOX@ZIF-8 NPs (Figure 2C). This fact was attributed to the targeting property of the folate ligand and the role of VER in overcoming the drug efflux mediated through the overexpressed *p*-gp in MDR cancer cells, i.e., MCF-7/A cells. Fluorescence inverted microscopy showed that PEG-FA/(DOX+VER)@ZIF-8 NPs have a higher intensity of red fluorescence than (DOX+VER)@ZIF-8 NPs in MCF-7 cells, confirming the specific binding between folate ligand and overexpressed FA receptors on the cancer cells. In agreement with fluorescence inverted microscopy, flow cytometry analy-

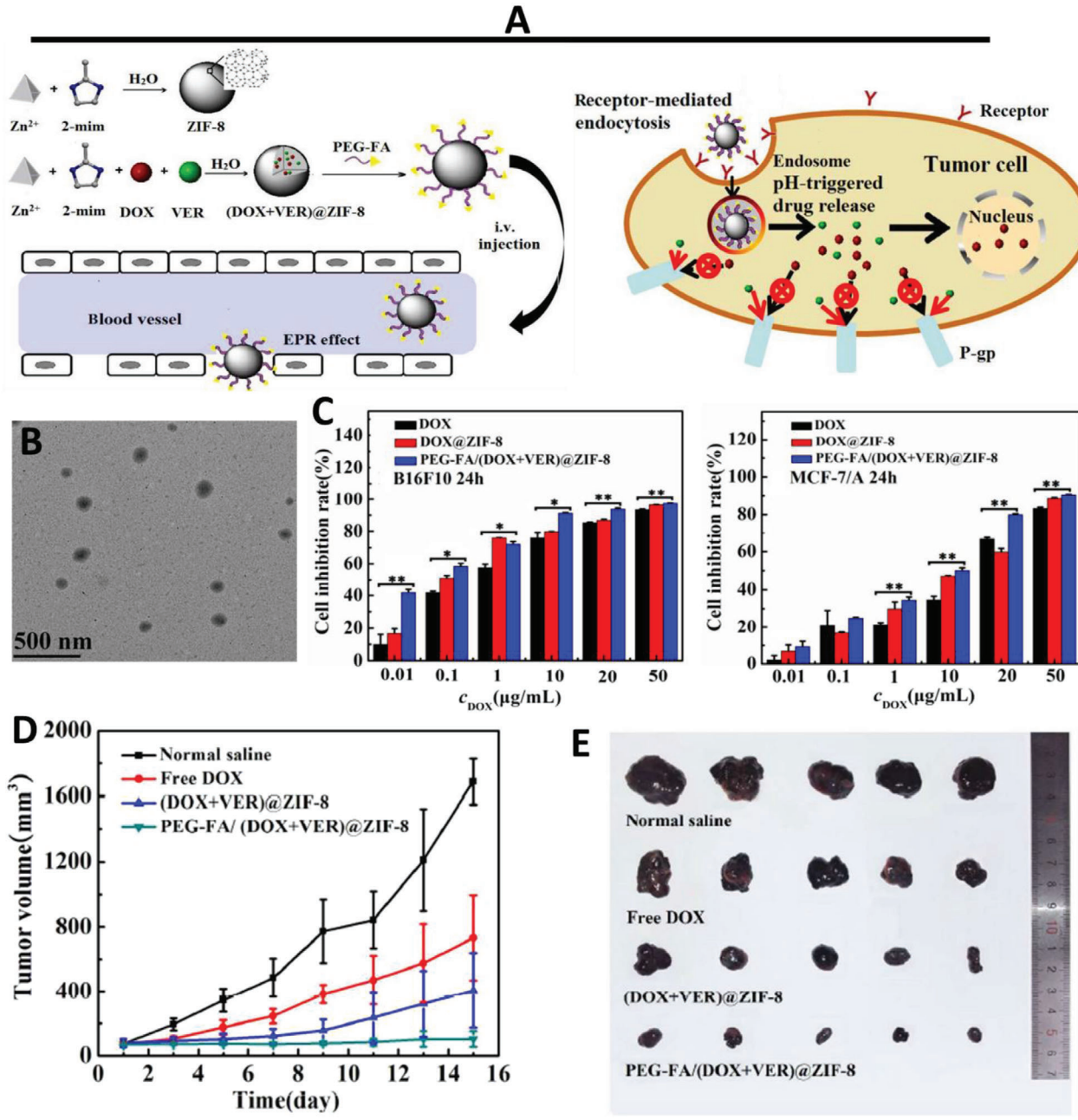

Figure 2. A) Schematic depiction of PEG-FA/(DOX+VER)@ZIF-8 synthesis and accumulation in tumor site via the enhanced permeability and retention (EPR) effect are shown in the left. The uptake of the DDS by tumor cells via folate receptors, pH-degradability of the DDS under the acidic tumor microenvironment, and MDR reversal mediated by VER are shown in the right schematic. B) The TEM image of PEG-FA/(DOX+VER)@ZIF-8 NPs. C) The cell inhibition rates (%) of different formulations to B16F10 and MCF-7/A cells after treatment for 24 h ($0.01 \leq *p < 0.05$, $**p < 0.01$, $n = 3$). D) Time-dependent tumor growth curves after different treatments. E) Photographs of excised tumors of mice bearing melanoma and treated with different formulations. Reproduced with permission.[33] Copyright 2017, American Chemical Society.

sis proved that the cellular uptake of (DOX+VER)@ZIF-8 NPs into *p*-gp-overexpressed MCF-7 cells was higher than free DOX and DOX@ZIF-8, demonstrating the inhibitory effect of VER on drug efflux induced by *p*-gp. As shown in Figure 2D, different formulations were studied in vivo. Among all the formulations, the mice treated by PEG-FA/(DOX+VER)@ZIF-8 NPs exhibited the best tumor inhibition effect. This behavior was also confirmed by the tumors dissected and photographed after the last injection (Figure 2E), ascribed to the pH-responsive property of the NPs, active targeting capability via FA and the MDR reversal mediated by VER. Altogether, this DDS broadened the applications of ZIFs in the biomedical field and was an efficient formulation in reversing the MDR for targeted cancer therapy goals.

3.2. Antibacterial Applications of ZIFs

MOFs have extensively been used as bactericidal agents through the release of antimicrobial metal ions (e.g., Ag^+, Zn^{2+}, and Co^{2+}) or antimicrobial agents from their framework.[43] It has been shown that particle size, shape, zeta-potential and chemical properties of NPs have a significant impact on their antibacterial activity.[132,133] As particle size, morphology, and composition of the MOFs are tunable, there is a great opportunity to treat various microbial infections by adjusting their physicochemical properties, a unique benefit that is difficult to achieve by conventional antibiotics.[27,43] Although MOFs have huge surface area and high porosity, their small pore size limits the loading of large molecules via post-synthetic methods. The access to MOFs containing large pore apertures is challenging yet and needs complicated synthesis procedures.[15,64,134–136] As mentioned above, ZIFs can encapsulate many organic/inorganic cargos via growing around the guests, while maintaining the functionality of the cargos.[100] ZIFs have been successfully employed to encapsulate antibiotics, such as ciprofloxacin,[137] gentamicin,[138] physcion,[112] ceftazidime,[111] and vancomycin (Van)[114] for antimicrobial therapy. For example, Song et al.[26] prepared 2-nitrobenzaldehyde (o-NBA) and rifampicin (RFP)-loaded ZIF-8 (o-NBA-RFP@ZIF-8) through a one-pot method for light-controlled antibacterial therapy. Under UV-light treatment (365 nm), o-NBA was converted to 2-nitrosobenzoic acid, thus serving as pH-jump reagent to generate an acidic environment and degrade the ZIF-8 network, leading to burst release of RFP antibiotic and Zn^{2+} and, ultimately, resulting in synergistic antibacterial therapy to inhibit bacteria-induced wound infection and promoting wound healing (**Figure 3**A). In the presence UV-light, TEM images proved the pH-dependent degradation of o-NBA-RFP@ZIF-8 NPs (Figure 3B). Light-triggered antibiotic release studies revealed no drug release from RFP@ZIF-8 NPs in the absence of o-NBA (Figure 3C). In contrast, a maximum of 80 wt% of RFP was released within 150 min upon UV-light irradiation of the o-NBA-RFP@ZIF-8 NPs, confirming pH dependency of the drug release by in situ light-mediated acid generation (Figure 3C) and subsequent ZIF network dissolvation and, thus, pH decreasing and production of Zn^{2+} ions in the release medium (Figure 3D,E).

As shown in Figure 3F, in vitro antibacterial assays showed that o-NBA-RFP@ZIF-8 had higher antibacterial activity against both the Gram-positive methicillin-resistant *Staphylococcus aureus* (MRSA) and Gram-negative ampicillin-resistant *Escherichia coli* than the other samples under UV-light treatment. This was attributed to the synergistic effect between the antibiotic and Zn^{2+} ion released from the o-NBA-RFP@ZIF-8. In vivo antibacterial efficacy was evaluated by MRSA and ampicillin-resistant *E. Coli*-induced wound infection model on the back of BALBc mice. As shown in Figure 3G, the wound size using o-NBA-RFP@ZIF-8 as a treatment agent under UV-light irradiation decreased much faster (80%) than the other groups. In the group treated with the o-NBA-RFP@ZIF-8 + light, well-established collagen fibers and dermal layer formation was confirmed by Masson's trichrome staining, demonstrating high efficacy of the synergistic treatment to eradicate the infection, promote derm generation, and modulate the collagen alignment, thus leading to accelerated wound healing.[26]

3.3. ZIFs for Biomimetic Mineralization

Biomimetic mineralization (bio-min) with MOFs is an emerging and robust strategy to shield sensitive biological materials toward enhanced thermal stability, protection against denaturing proteolytic agents/mechanical stress/UV radiation and extended shelf-life time.[41,139–143] Using this strategy, many encapsulated bio-macromolecules including enzymes,[39,41,144–152] proteins,[40,153–159] vaccines,[160–162] antibodies,[163] or even more complex living systems[139,164–167] (e.g., bacteria, viruses, and eukaryotic cells) have been made with enhanced bioactivity and stability. For the first time, a rapid and low-cost bio-min method was introduced by Liang et al.[143] as a protective approach for the coating of bio-macromolecules. They showed that a wide variety of bio-macromolecules, including enzymes, proteins, and DNA could successfully be encapsulated within MOFs framework. The resulting biocomposites were stable and kept their activity even after exposure to harsh conditions. The change of pH was used to control the release of the cargos from the MOF-coated bio-macromolecules. For the bio-min process, ZIF NPs, especially ZIF-8, have been shown to be a superior candidate to protect bio-macromolecules under the mild condition of the biomineralization process.[41] For example, the bio-min of ZIF-8 can be performed within a few minutes in aqueous solutions and under ambient temperature without using toxic organic solvents.[158] However, despite many examples available on bio-min of diverse bio-macromolecules, the mechanism of such bio-min has not fully been investigated.[143]

Enzymes are efficient and environmentally benign catalysts that can selectively catalyze different biological processes to produce various chemicals and pharmaceutically active medicines.[168] However, their unfavorable stability against heat and organic solvents and undesirable recyclability have limited the use of enzymes toward practical applications.[41] Therefore, the immobilization of enzymes within a porous matrix is a straightforward and efficient method to solve the above-mentioned problems and improve the performance of enzymatic reactions.[41,141] ZIFs have been able to encapsulate various enzymes, such as lipase,[144,169] horseradish peroxidase,[145,147] catalase,[38,148,149,170] glucose oxidase,[39,145–147] chloroperoxidase,[146] lysozyme,[143] cytochrome *c*,[156] and *β*-galactosidase,[147] to render them high stability. In this condition, the porous shell allowed substrates to diffuse through the pores and undergo catalysis by the caged enzyme, while keeping the inlaid enzyme from denaturation by various chemicals. It should be added that two or even three enzymes have been simultaneously embedded in ZIF NPs, acting as nanoreactors in biocatalytic cascades transformations.[145–147]

In 2018, Chen et al.[39] fabricated two smart glucose-responsive DDSs based on ZIF-8 NPs. In the first system, glucose oxidase (GOx) enzyme and insulin protein were loaded within ZIF-8 NPs in a one-pot method, while the second nanosystem was composed of anti-vascular endothelial growth factor (VEGF) aptamer and GOx co-encapsulated into the ZIF-8 NPs. In the presence of glucose, GOx-mediated aerobic oxidation of glucose to H_2O_2/gluconic acid and subsequent creation of an acidic microenvironment occurred. As a result, insulin and VEGF were released from the particles, known as acid-degradable sense-and-treat systems. Both of these DDSs were potentially suggested as

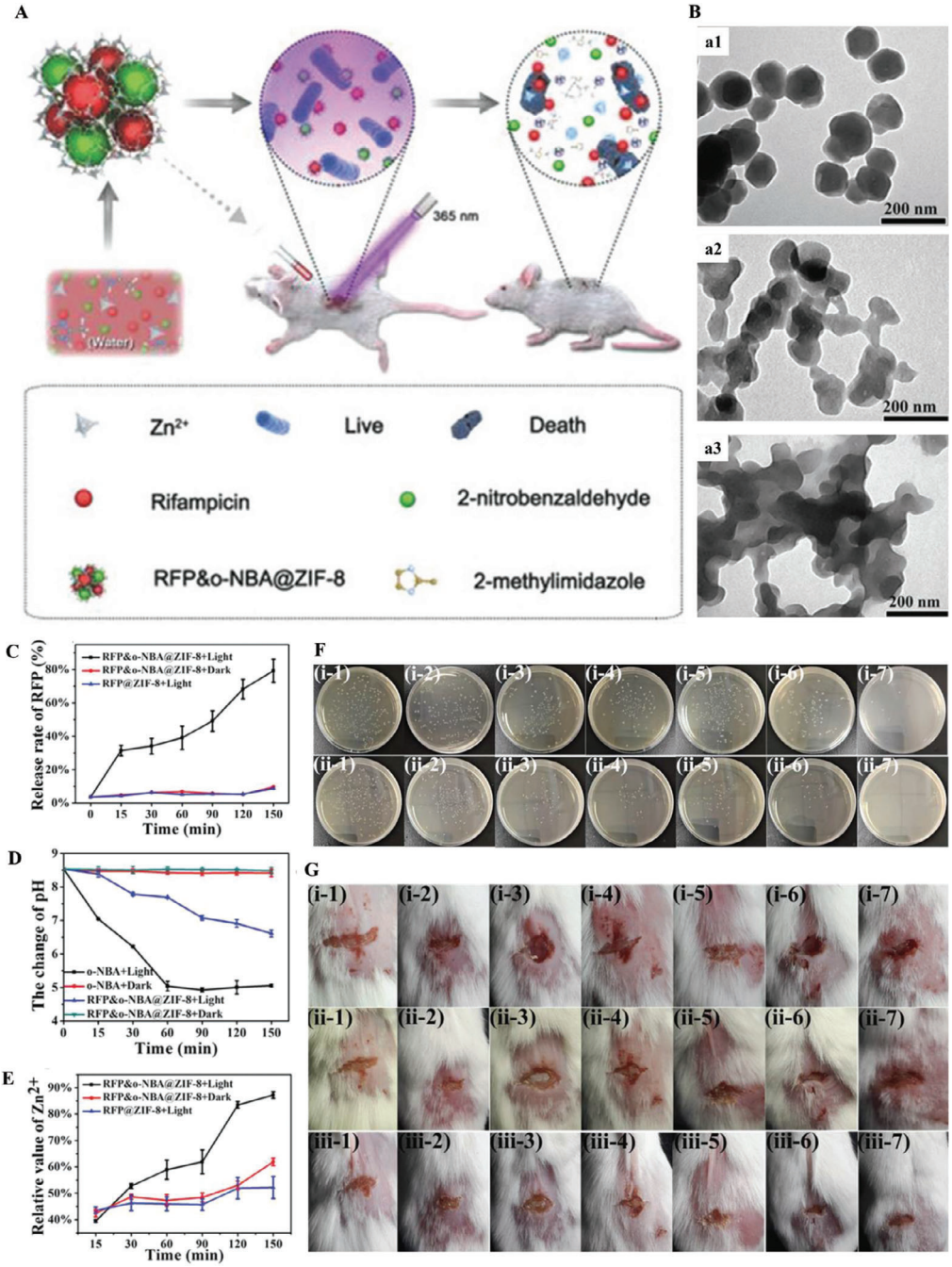

Figure 3. A) Schematic illustration of the o-NBA-RFP@ZIF-8 synthesis and in the application of the DDS in the light-controlled synergistic antibacterial therapy to inhibit bacteria-induced wound infection. B) a) TEM images of o-NBA-RFP@ZIF-8 NPs treated with UV irradiation at different exposure times of a1 = 15, a2 = 60, and a3 = 120 min. C) The release of RFP; D) pH change; and E) Zn^{2+} ion release at different time periods and conditions. F) Panels (i) and (ii) refer to ampicillin-resistant *E. coli* and MRSA, respectively, treated at different conditions of: 1) PBS + UV-light, 2) ZIF-8 + UV-light, 3) o-NBA@ZIF-8 + dark, 4) o-NBA@ZIF-8 + UV-light, 5) RFP@ZIF-8 + UV-light, 6) o-NBA- RFP@ZIF-8 + dark, and 7) o-NBA-RFP @ZIF-8 + UV-light. G) Photographs of infected wound infected by MRSA 1) PBS + UV-light, 2) ZIF-8 + UV-light, 3) o-NBA@ZIF-8 + dark, 4) o-NBA@ZIF-8 + UV-light, 5) RFP@ZIF-8 + UV-light, 6) o-NBA-RFP@ZIF-8 + dark, 7) o-NBA-RFP @ZIF-8 + UV-light, and 8) healthy mice. i) 0 day, ii) 1 day, and iii) 3 day. Reproduced with permission.[26] Copyright 2018, Wiley-VCH.

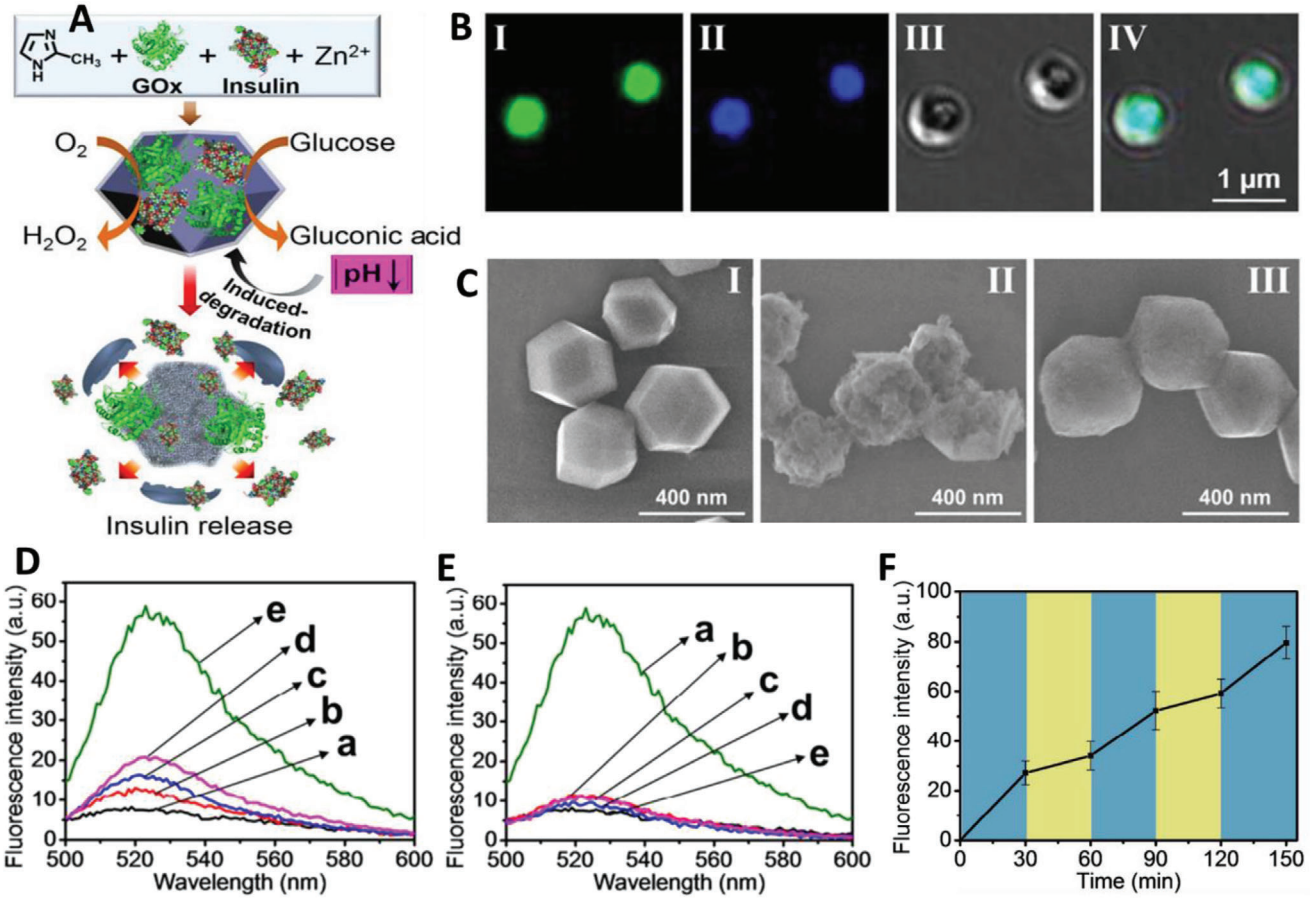

Figure 4. A) Schematic illustration of the IG@ZIF-8 synthesis and the pH degradable property of the nanosystem triggered by glucose through the encapsulated GOx. B) Confocal laser scanning microscopy images of the FITC-labeled insulin- and coumarin-modified GOx-loaded ZIF-8 (I and II, respectively) and the bright field and merged image of the developed DDS (III and IV, respectively). C) SEM images of I) the insulin and GOx-loaded ZIF-8, II) glucose-treated insulin/GOx-loaded ZIF-8 for 1 h, and III) treatment of the DDS with a buffer solution pH 7.4 for two days. D) Glucose concentration-dependent release study of the IG@ZIF-8 at different concentrations of glucose: a) 0, b) 1×10^{-3} M, c) 5×10^{-3} M, d) 10×10^{-3} M, e) 50×10^{-3} M for 1 h. E) The release study of FITC-labeled insulin from the IG@ZIF-8 in the presence of different carbohydrates, including a) glucose (50×10^{-3} M), b) galactose (50×10^{-3} M), c) β-lactose (50×10^{-3} M), d) sucrose (50×10^{-3} M), and e) pure buffer solution, for 1 h. F) Switchable release of insulin from the IG@ZIF-8 in the presence of high (15×10^{-3} M, blue) and low (5×10^{-3} M, yellow) concentration of glucose. Reproduced with permission.[39] Copyright 2012, American Chemical Society.

"intelligent" carriers for the therapy of diabetes and macular disease, respectively. In the case of controlled release of insulin from the insulin and GOx-coloaded ZIF-8 (IG@ZIF-8) NPs, loading of the two cargos was performed in a one-pot method, as shown in **Figure 4**A. Glucose acted as a key player to control the local pH at the nanoenvironment of the IG@ZIF-8 NPs. In fact, the local acidic nanoenvironment created by the conversion of glucose to gluconic acid via the biocatalytic effect of GOx led to the degradation of the IG@ZIF-8 and, in turn, induced the release of insulin. In the confocal laser scanning microscopy images of the ZIF-8 NPs loaded with FITC-labeled insulin (green) and the coumarin-functionalized GOx (blue) (Figure 4B, panel I and panel II, respectively), the overlapped turquoise color was related to the internal integration of the two cargos in the ZIF-8 NPs (Figure 4B, panel IV), confirming the successful co-immobilization of the proteins within the porous ZIF. Scanning electron microscope (SEM) image of the IG@ZIF-8 NPs with rhombic dodecahedral shape and particle size of ≈300–350 nm, are shown in Figure 4C panel (I). This morphology was retained when the IG@ZIF-8 NPs were treated with the buffer solution without glucose (Figure 4C, panel III). Interestingly, after treatment with glucose solution (50×10^{-3} M), the corrosion of the protein-loaded ZIF-8 occurred, proving the degradation of the IG@ZIF-8 due to local acidic nanoenvironment, generated by the GOx-mediated oxidation of glucose (Figure 4C, panel II). Release study of FITC-labeled insulin from the IG@ZIF-8 showed that when the concentration of glucose increased, the release of the insulin was accelerated for a fixed time of 1 h, again confirming the glucose-dependent degradation of the IG@ZIF-8 to control the insulin release (Figure 4D). In addition, among different saccharides, only glucose triggered the release of insulin from the IG@ZIF-8 (Figure 4E). A switchable ON/OFF release of insulin was also observed when an increase/decrease of the glucose concentration was applied (Figure 4F). All these observations clearly proved that the intelligent controlled DDS of insulin could potentially be developed for the treatment of diabetes. The same results were ob-

tained when VEGF aptamer and GOx were encapsulated within ZIF-8 (VG-ZIF-8). The authors showed that the release of VEGF aptamer was glucose-dependent in the VG-ZIF-8 NPs, which was consistent with the increased local acidity at the aptamer-loaded ZIF-8 due to the GOx-catalyzed conversion of glucose to gluconic acid, and thus, degradation of ZIF-8 matrix and accelerated release of the VEGF aptamer. These results hold a great promise for the potential application of the VG-ZIF-8 as an "intelligent" system for the inhibition of VEGF-induced angiogenesis in macular disease.[39] Recently, GOx and hemoglobin encapsulated-ZIF-8 NPs were prepared in which GOx and hemoglobin acted as nutrient starvation and radical generation agents respectively, endowing the nanosystem anti-cancer property in vitro.[171] Although great results were obtained in the in vitro phase of this study, the in vivo studies in animal models were missing and seems to be imperative in future studies with similar concept.

Cell membrane coating nanotechnology has emerged as a promising approach to facilitate the delivery of therapeutic agents through the camouflagation of NPs within a layer of a specific cell membrane. Utilizing such bio-inspired technology could enhance the colloidal stability of the NPs and minimize their non-specific tissue accumulation.[172,173] Using distinctive advantages of neutrophils, including inflammation targeting ability and antitumor/antibacterial properties, artificial super neutrophils were constructed by encapsulating two enzymes, i.e., GOx and chloroperoxidase (CPO) into ZIF-8 NPs, and further coverage of neutrophil membrane (NM) on the surface of GOx/CPO-caged ZIF-8 NPs. It has been shown that the neutrophil-mimicked nanosystem produced seven-fold higher reactive hypochlorous acid (HClO) than the natural neutrophils through GOx/CPO-mediated cascades reactions for eliminating tumors and infections.[146] The encapsulation of vaccines into MOFs, i.e., ovalbumin and attaching the cytosine-phosphate-guanine oligodeoxynucleotides (CPGO) in/on ZIF-8 (OVA/CPGO-ZIF-8), was carried out by Qu's research group.[161] Their results showed that the OVA/CPGO-ZIF-8 had pH-responsive property, efficiently enabling the system to release the antigen and CPGO in the same antigen presenting cells, inducing potent humoral and cellular immune responses. This study sheds light on producing novel/effective MOF-based vaccines against a range of ailments.

In addition to the embedding of a wide variety of drugs, enzymes, proteins, and vaccines, living cells[165] and viruses[164,167] were used to encapsulate/cage within the ZIF frameworks.[139] For the first time, biomimetic mineralization of tobacco mosaic virus (TMV) using ZIF-8 precursors as a robust MOF for encasing and protecting the virus against foreign denaturing environmental stressors was investigated by Gassensmith's research group.[167] They showed that discrete rod-shaped TMV-encapsulated ZIF-8 with good uniformity could be obtained. They also demonstrated that the metal concentration and ligand to metal molar ratio affected distinct morphologies of the core–shell composites and the size of ZIF-8 NPs, which greatly influenced the stability of the core–shell hybrid particles.[164] On the encapsulation of living cells, i.e., yeast, it has been shown that mechanical constraints imposed by the ZIF-8 coating prohibited the living cells from reproducing, while cell metabolic processes were maintained due to the microporous shell of ZIF-8 that allowed the transfer of small molecules like oxygen and glucose to the cell. Interestingly, this biomimetic mineralization, i.e., the ZIF-shell, was easily be removed by mildly acidic pH or ethylenediaminetetraacetic acid (EDTA), leading to a "switching-OFF" effect and the recovery of the full functionality of the encapsulated cells or bio-macromolecules.[143,165]

4. Biomedical Applications of Multifunctional ZIF-Based Composites

As mentioned in the introduction section, ZIF-based composites, especially the ones prepared by ZIF-8, have extensively been applied in many biomedical applications, including cancer therapy[22–25] and antimicrobial purposes.[26–28] Nevertheless, the poor water disparity of ZIF-8 has limited its advanced applications.[174] On the other hand, the integration of functional materials (e.g., metal NPs/nanorods, mesoporous silicas, photosensitizers (PS), light-absorbing dyes, quantum dots, polymers, graphene, proteins, and enzymes) with ZIFs is a necessity to combine the merits of both the components, including the flexibility and high porosity of ZIFs with unique imaging, targeting properties and dispersiblity of functional materials (Scheme 1). Thus, the unique features of the composites, resulting from the synergistic combination of both ZIFs and other active components, have made them as highly attractive hybrid materials for many biomedical applications, which are not attainable with an individual component. Table 2 summarizes the recent biomedical applications developed by ZIF-based composites. In this section, we have classified the applications of ZIF-8 into three categories of monotherapy, combined therapy, and theranostics applications, and discuss them in detail.

4.1. Monotherapy by ZIF Nanocomposites

Chemotherapy using nanoscale DDSs is one of the most effective monotherapeutic approaches in cancer ablation in vivo.[208,209] As discussed in the previous section, ZIF-8 intrinsically possess the properties of large surface areas, high porosities, and well-defined structures, making this material capable of loading and releasing different chemotherapeutic agents.[21] However, its small pore size (3.4 Å) and poor dispersity in aqueous solution have limited its wide application in chemotherapy. Therefore, many attempts have been made on the design and fabrication of hybrid structures to overcome these problems.[21] Thorough a facile and simple method, polyacrylic acid@ZIF-8 (PAA@ZIF-8) NPs were fabricated by Ren et al.[37] with ultrahigh DOX loading capability (1.9 g of DOX g^{-1} composite), successfully employed as a pH-dependent DDS in cancer treatment in vitro. As shown in **Figure 5**A, PAA@ZIF-8 composite was prepared by ion-exchange between Zn^{2+} and Na^{+} on the surface of poly(acrylic acid sodium salt) (PAAS) NPs followed by dropping the resultant NPs into a methanol solution of 2-MeIm to form the hybrid PAA@ZIF-8 nanostructure, showing an particle size of 128 nm measured by SEM (Figure 5B). The NPs were highly dispersed in serum and water with no obvious aggregation, confirming their good stability and dispersity. As a result of the pH-dependent degradability of the nanosystem, a faster drug release rate was observed in acidic medium (pH 5.5) rather than

Table 2. Summary of multifunctional ZIF-based nanocomposites for diverse applications.

Type of composite and surface ligand	Encapsulated Cargo	Size [nm/μm] and Zeta potential [mV]	Imaging modality	Cells and animal models	Main conclusion	Ref
PAA@ZIF-8	DOX	Before loading: 128 nm; ND	–	In vitro: Epithelial MCF-7 breast cancer cells	– PAA@ZIF-8 NPs exhibited pH-sensitive DOX release property and ultrahigh loading capacity. – Drug release from the DOX-loaded PAA@ZIF-8 NPs was much faster in an acidic environment (pH 5.5) than at neutral pH 7.4. – The MTT assay showed that the nanocomposite was nearly nontoxic to live cells.	[37]
FA-BSA-modified CuS@ZIF-8	QT	After loading: 45.1 ± 15.0 nm; −27.9± 6.0 mV	NIR-FI	In vitro: B16F10 melanoma cells In vivo: B16F10 melanoma model	– The FA-BSA-modified nanocomposite was successfully utilized for overcoming the drawbacks of QT, including poor bioavailability and low water solubility, as well as synergistic combination of chemotherapy and PTT of cancer in vitro and in vivo.	[175]
CuS@ZIF-8	DOX	Before loading: 125 nm; ND	ITI	In vitro: Epithelial MCF-7 breast cancer cells In vivo: Epithelial MCF-7 breast cancer model	– For the first time, it was demonstrated that the ZIF-8 network could be disintegrated at pH 7.4 upon NIR irradiation. – DOX-loaded CuS@ZIF-8 nanocomposites was successfully used in synergistic CPTT of cancer both in vitro and in vivo.	[176]
ZIF-8-PAAS	DOX	Before loading: 30–200 nm; ND		In vitro: HeLa cell line In vivo: Mammary gland 4T1 model	– Different sizes of ZIF-8-PAAS nanocomposites, ranging from 30 to 200 nm were constructed, while keeping their crystallinity and pH sensitivity. – Compared to free DOX, DOX-loaded and PEG functionalized ZIF-8-PAAS greatly enhanced cancer chemotherapy both in vitro and in vivo. – After PEG functionalization and DOX loading of the nanosystem, biodistribution studies showed that DOX could be effectively delivered to the tumor area within 24 h. After 48 h, the fluorescence intensity of DOX in the tumor site further increased, while the fluorescence intensities in major organs, including spleen, lung heart, liver, and kidney, started to decrease.	[34]
ZnPc@ZIF-8	–	255 nm; + 26 mV	FI	In vitro: Epithelial HepG-2 cell line	– Excellent photodynamic activity for cancer treatment was observed using the ZnPc@ZIF-8 nanocomposite in vitro. – ZnPc@ZIF-8 was completely degraded after PDT.	[177]
ZnPc-COOH@ZIF-8	–	97.2 nm; ND	–	In vitro: Epithelial HepG-2 cell line	– The ZnPc-COOH@ZIF-8 NPs showed high singlet oxygen quantum yield and intracellular ROS generation. – Cell viability demonstrated good anticancer efficacy of the NPs with low IC50 values (4.2–4.9 μg mL^{-1}) under laser light irradiation.	[178]

(*Continued*)

Table 2. Continued.

Type of composite and surface ligand	Encapsulated Cargo	Size [nm/μm] and Zeta potential [mV]	Imaging modality	Cells and animal models	Main conclusion	Ref
Fe_3O_4@ZIF-8	–	120 nm; −25.7 mV	MRI	In vitro: Endothelial HUVEC and epithelial 4T1 cells In vivo: Mammary gland 4T1 model	– Very high contrast for tumor detection.	[31]
RSA-conjugated Fe_3O_4@ZIF-90	5-FU	Before loading: 90 nm; −18 mV	MRI	ND	– Remarkable 5-FU release from the RSA-conjugated Fe_3O_4@ZIF-90 NPs was realized under extremely low frequency alternating magnetic field. – The nanocomposite served as an effective MRI contrast tracer for potential visualization of drug delivery, paving way for precise construction of DDSs under MRI surveillance.	[179]
g-C_3N_4@ZIF-8	DOX	Before loading: 60 nm; +31.9 mV After loading: ≈60 nm; ND	FI	In vitro: Epithelial A549 cell	– The C_3N_4@ZIF-8 NPs exhibited good biocompatibility and generated singlet oxygen efficiently. – The DOX-loaded g-C_3N_4@ZIF-8 NPs were successfully utilized in dual-color fluorescence imaging-guided photo-chemo therapy of tumor cells in vitro.	[180]
MSN-COOH@ZIF-8	Bcl-2 siRNA and DOX	Before loading: ≈80 nm; + 31.12 ± 2.13 mV	–	In vitro: Epithelial MCF-7/ADR and epithelial SKOV-3/ADR cells	– The thin film on the surface of DOX-loaded MSN-COOH had three functions: – It acted as a pore blocker to prevent premature release of DOX. – It converted the charge of MSN-COOH from negative to positive to improve the efficient adsorption of the siRNA via electrostatic interactions and its protection from nuclease degradation. – It was decomposed in the acidic endo-lysosome and led to the intracellular release of the siRNA and DOX, paving an efficient way to overcome MDR cancer cells in vitro.	[35]
ZnO@ZIF-8	DOX	After loading: 270 nm; ≈−2 mV	–	In vitro: HeLa cell line	– The mesoporous ZnO core acted as a DOX storage reservoir and ZIF-8 shell served as pore blocker to prevent premature release of DOX at the physiological environment. – Significant cytotoxicity of the DOX-loaded ZnO@ZIF-8 was attributed to synergistic ROS production of the ZnO@ZIF-8 carrier, generated in acidic condition, and the chemotherapeutic effect of the released DOX.	[181]
PEG-modified Mn-Zn-ZIF-8	–	≈250 nm; ND	FI MRI	In vitro: Epithelial 4T1 cells	– The bimetallic Mn-Zn-ZIF composite showed pH-responsive T1-weighted MRI contrast effect.	[182]
PANI@ZIF-8	5-FU	Before loading: 200 nm; ND	–	In vitro: Epithelial MCF-7 breast cancer cells	– The 5-FU-loaded PANI@ZIF-8 exhibited excellent CPTT effect against breast cancer cells in vitro.	[183]

(*Continued*)

Table 2. Continued.

Type of composite and surface ligand	Encapsulated Cargo	Size [nm/μm] and Zeta potential [mV]	Imaging modality	Cells and animal models	Main conclusion	Ref
Poloxamer 188-modified ZIF-8	NaClO	Before loading: 140.1 ± 6.3 nm; ≈+8.0 mV After loading: 177.9 ± 13.2 nm; <+8.0 mV	FI	In vitro: Epithelial 4T1 and fibroblast 3T3 cells In vivo: mammary gland 4T1 model	– As a proof of concept, concurrent delivery of ascorbate (as H_2O_2 generator in the tumor site) and hypochlorous ion-loaded poloxamer 188-modified ZIF-8 NPs could produce ROS at the tumor site, leading to efficient CDT both in vitro and in vivo without noticeable side-effects. – During the treatment, no obvious body weight loss of mice was observed, confirming no serious systemic toxicity in spite of nonspecific biodistribution of the nanosystem to healthy organs.	[184]
GQD@ZIF-8	DOX	Before loading: 50–100 nm; ND After loading: 50–100 nm; ND	–	In vitro: Epithelial 4T1 cells	– The embedded GQD NPs could efficiently convert NIR irradiation into heat. – Compared to chemotherapy and PTT alone, synergistic CPTT strategy significantly killed breast cancer 4T1 cells in vitro.	[185]
PEG-PUSeSe-PEG@ZIF-8	DOX	After loading: 200 nm; ND	–	In vitro: Epithelial MDA-MB-231 cells	– DOX-loaded PEG-PUSeSe-PEG@ZIF-8 could successfully release the encapsulated drug in the presence of external redox agents and acidic environment in vitro.	[186]
HA-modified IR820@ZIF-8	Cytarabine	After loading: 132.0 ± 9.5 nm; ND	FI ITI	In vitro: Epithelial 4T1 cells In vivo: Mammary gland 4T1 model	– Indocyanine green (IR820) was employed to conjugate with cytarabine for the formation of a prodrug in order to increase drug loading. – A successful fluorescence imaging-guided CPTT was realized through a pH-responsive release behavior in vitro and in vivo. – Biodistribution studies showed that the HA-modified IR820@ZIF-8 can accumulate at the tumor area within 1 h post-administration, which was faster than the nonmodified NPs. The HA-modified nanosystem kept high concentration at tumors during 24 h.	[187]
PDA-PCM@ZIF-8	DOX	After loading: 130 nm; −5.1 mV	ITI	In vitro: Epithelial HepG2 cells In vivo: Hepatocellular carcinoma model	– The biocompatibility of ZIF-8 was greatly improved by PDA modification. – The PDA, as a photothermal agent, caused thermal response switch of phase change materials for NIR-controlled DOX release. – Compared to chemotherapy or PTT alone, a remarkable anti-tumor effect was observed using synergistic thermo-chemotherapy method.	[22]
PDA-MSN@ZIF-8	DOX and CCM	Before loading: ≈100 nm; +28.7 ± 1.1 mV	–	In vitro: Epithelial MCF-7/ADR cancer cells	– The CCM and DOX were successfully loaded within the ZIF shell and PDA-MSN core, respectively. – CCM was released upon ZIF-8 shell degradation which had a strong effect on the inhibition of *p*-gp, and, subsequently, the sustained release of DOX from PDA-MSN core caused efficient therapeutic function, potentially opening new ways for reversing the MDR of cancer cells.	[188]

(*Continued*)

Table 2. Continued.

Type of composite and surface ligand	Encapsulated Cargo	Size [nm/μm] and Zeta potential [mV]	Imaging modality	Cells and animal models	Main conclusion	Ref
ZIF-8@PDA	CCM	After loading: 350 nm; −25.4 mV	ITI PAI	In vitro: Epithelial MCF-7 breast cancer cells and HeLa cell line In vivo: Cervical cancer HeLa model	– The 2D nanosheets of ZIF-8@PDA structures exhibited ultrahigh CCM loading content (59.6%) and excellent stability in water. – Efficient and precise CPTT of cancer was accomplished in vitro and in vivo.	[189]
PDA@ZIF-8	MB and catalase	After loading: ≈100 nm; + 13.2 mV	ITI	In vitro: HeLa cell line In vivo: Cervical cancer HeLa model	– Successful synergistic PDT and PTT was implemented for effective anti-cancer treatment in vitro and in vivo. – The study demonstrated improved PDT through catalase enhanced self-sufficient O_2 generation and ROS production with the aid of MB as photosensitizer. – PDA acted as a photothermal agent for PTT.	[190]
Galactose-modified ZIF-8@WP6	DOX	After loading: 203.5 nm; ND	–	In vitro: Epithelial HepG2 cells	– DOX-loaded galactose-modified ZIF-8@WP6 exhibited excellent pH-sensitive drug release behavior and water dispersibility. – Cell cytotoxicity studies confirmed that the DOX-loaded NPs had selective toxicity for hepatoma cancer cells.	[174]
HMS@ZIF-8	DOX	After loading: ≈700 nm; +31.2 mV	–	In vitro: Epithelial MCF-7 breast cancer cells	– Compared to free DOX, the DOX-loaded HMS@ZIF-8 NPs showed much higher cytotoxicity against MCF-7 cells. – The drug was not released under the physiological environment (pH 7.4) and released at acidic condition (pH 4–6) from the carrier.	[191]
HMS@ZIF-8	DOX	Before loading: ≈350 nm; ND	–	In vitro: Human hepatocarcinoma SMMC-7721 cells	– ZIF-8 acted as both a self-sacrificial template to prepare monodisperse and size-controllable HMS and as a pore blocker to construct a pH-responsive DDS. – Remarkable efficiency in the killing of cancer cells was observed by the DOX-loaded HMS@ZIF-8	[192]
C-dots@ZIF-8	5-FU	Before loading: 110 nm; +10.9 mV	FI	In vitro: HeLa cell line	– The particle size and fluorescence intensity of C-dots@ZIF-8 NPs was tunable. – The NPs not only acted as a pH-responsive drug carrier but also used as a fluorescence imaging agent.	[61]
AuNR@ ZIF-8	DOX	Before loading: 140 nm; ND	ITI	In vitro: Epithelial 4T1 cells In vivo: Mammary gland 4T1 model	– High DOX loading capacity and pH/NIR light-responsive DOX release occurred by the AuNR@ ZIF-8 drug carriers. – Effective synergistic CPTT was implemented both in vitro and in vivo.	[60]
PVP-modified Au@ ZIF-8	Ce6	After loading: 106 ± 7.3; ND	–	In vitro: Epithelial EMT-6 cells In vivo: Epithelial EMT-6 breast cancer model	– Highly efficient PDT was achieved using the Ce6-loaded PVP-modified Au@ ZIF-8 in vivo. – AuNPs acted as nanozyme to catalyze H_2O_2 to generate O_2 for alleviating tumor hypoxia. The in situ generated O_2 boosted the production of $^1O_2$ through the PDT route under irradiation to kill tumor cells.	[193]

(*Continued*)

Table 2. Continued.

Type of composite and surface ligand	Encapsulated Cargo	Size [nm/μm] and Zeta potential [mV]	Imaging modality	Cells and animal models	Main conclusion	Ref
HA-modified ZIF-8-Fe-PDA	DOX	After loading: ≈150 nm; −30.2 mV	MRI	Prostatic PC-3 epithelial and L929 fibroblast cell lines	– Compared to free DOX, DOX-loaded HA-modified ZIF-8-Fe-PDA showed enhanced chemotherapeutic efficacy due to targeting ability of the NPs toward CD44 overexpressed PC-3 cells, which improved intracellular uptake of the DDS and increased their killing effect on the cells.	[194]
ZIF-8/GO	FES	After loading: 50–100 nm; ND	ITI	In vitro: Epithelial 4T1 cells	– Upon NIR irradiation (808 nm), FES-loaded ZIF-8/GO NPs had an excellent PTT effect to kill cancer cells in vitro. – The FES-loaded NPs showed negligible cytotoxicity against 4T1 cells.	[195]
Polyoxometallate@ ZIF-8	5-FU and MB	–	–	ND	– Three ZIF-based nanocomposites were constructed by $H_3PW_{12}O_{40}$, $H_4SiW_{12}O_{40}$ and $H_3PMo_{12}O_{40}$ polyoxometallates using a simple one-pot method. – MB and 5-FU-loaded $H_3PW_{12}O_{40}$ @ZIF-8 showed 80% cargo release over 32 days and 93% cargo release over 50 h for MB and 5-FU, respectively, in a simulated body fluid.	[196]
Fe_3O_4@PAA/AuNCs/ ZIF-8	DOX	Before loading: 130 nm; ND	MRI CT FI	In vitro: Epithelial HepG2 cells In vivo: Hepatocarcinoma H-22 model	– The Fe_3O_4@PAA/AuNCs/ZIF-8 NPs were biocompatible and possessed an ultrahigh loading capacity for DOX (1.54 g DOX g^{-1} NPs). – Simultaneous DOX delivery and trimodal (CT, MR, and fluorescence) imaging was achieved by the NPs in vitro and in vivo. – DOX-loaded NPs suppressed tumor growth effectively via the EPR effect.	[23]
CaO_2@ZIF-67	DOX	After loading: 200 nm; +30.1 mV	PAI	In vitro: Epithelial MCF-7 breast cancer cells In vivo: Epithelial MCF-7 breast cancer model	– Excellent chemo/chemodynamic therapy of tumors was achieved by CaO_2@DOX@ZIF-67 NPs in vitro and in vivo. – In the acidic TME, the DDS was degraded to rapidly release DOX and the Co^{2+} (as Fenton-like catalyst). Then, the exposed CaO_2 reacted with H_2O to simultaneously generate O_2 and H_2O_2, to relieve the hypoxia in TME and to produce ROS through the Fenton reaction of Co^{2+} and H_2O_2.	[197]
Catalase-modified UCNPs@ZIF-8	MB	ND	FI	In vitro: Epithelial PL45 cells	– The UCNPs/MB@ZIF-8@catalase nanocomposite acted as an efficient NIR/H_2O_2-responsive PDT agent against hypoxic tumor cells.	[198]
Si-Gd@PDMAEMA and PEG-FA-modified ZIF-8	DOX and Ce6	After loading: 70 nm; ≈ +5 mV	FI MRI	In vitro: Epithelial MCF-7 breast cancer cells and epithelial A549 cell In vivo: Epithelial MCF-7 breast cancer model	– In the nanocomposite, Si-Gd NPs and Ce6 were used for MRI and FI, respectively. Also, Ce6 was utilized as a PDT agent. In addition, due to the pH-responsive capability of PDMAEMA, it effectively prevented DOX leakage. – Excellent CPDT was obtained by the DOX and Ce6-loaded Si-Gd@PDMAEMA and PEG-FA-modified ZIF-8 guided by the dual-modal imaging in vivo.	[199]

(*Continued*)

Table 2. Continued.

Type of composite and surface ligand	Encapsulated Cargo	Size [nm/μm] and Zeta potential [mV]	Imaging modality	Cells and animal models	Main conclusion	Ref
PEGFA-modified UC@mSiO_2-RB@ZIF-90	DOX, RB, and O_2	ND	Upconversion and MRI	In vitro: HeLa and epithelial 4T1 cells In vivo: Hepatocarcinoma H-22 model	– ZIFs were used as an O_2 carrier to overcome tumor hypoxia. – Successful CPDT was achieved using DOX, RB, and O_2-loaded PEGFA-modified UC@mSiO_2-RB@ZIF-90 nanosystem through degradation of the outmost ZIF-90 shell under acidic condition, which accelerated the release of O_2 and DOX in the acidic TME to overcome tumor hypoxia and improve chemotherapy.	[200]
FA-modified UCNPs@ZIF-8	5-FU	Before loading: ≈200 nm; ND	FI	In vitro: HeLa cell line	– Due to the folate receptor-mediated endocytosis, the 5-FU-loaded FA-modified UCNPs@ZIF-8 DDS exhibited greater cytotoxicity against HeLa cells in vitro. – The FA-modified UCNPs@ZIF-8 nanocomposite not only used as a targeted anticancer drug carrier but also acted as a cellular imaging agent.	[201]
Fe_3O_4@carbon@ ZIF-8	DOX	Before loading: 220 nm; ND	FI MRI	In vitro: Epithelial A549 cell In vivo Lung A549 cell model	– The Fe_3O_4@carbon@ ZIF-8 NPs exhibited good biocompatibility, high drug loading content, pH-triggered drug release behavior as a DDS, and effective cellular uptake in vitro. – Compared to the free drug of DOX, remarkable inhibition of tumor growth was observed by the DOX-loaded NPs in vivo.	[202]
$CoFe_2O_4$@PDA@ZIF-8	DOX and CPT	Before loading: 150 nm; ND	MRI ITI	In vitro: Epithelial HepG2 cells In vivo: liver HepG2 cell model	– Compared to the single-drug chemotherapy system, the DOX and CPT-loaded DDS improved tumor therapeutic efficiency significantly. – PTT and accelerated drug-release were achieved using NIR irradiation. – Successful T2-weighted MR imaging-guided synergistic PTT and multidrug chemotherapy were achieved in vitro and in vivo.	[203]
ZGGO@ZIF-8	DOX	Before loading: 100–200 nm; ND	Autofluorescence-free NIR PersL imaging	In vitro: Epithelial 4T1 cells In vivo: Mammary gland 4T1 cells model	– The DOX-loaded ZGGO@ZIF-8 DDS possessed pH-responsive drug delivery behavior and the autofluorescence-free NIR PersL imaging capability, thus causing long-term PersL imaging without autofluorescence and effective tumor suppression in vivo. – Strong PersL signals of the NPs were found in the lung and liver, while weak signals were found in the kidney, spleen, and stomach.	[204]
Pd-Au@ZIF-8	DOX	Before loading: 253.7 nm; + 6.15 mV	–	In vitro: SMMC-7721 cell	– The Pd@Au core could effectively convert NIR laser into heat, causing not only accelerating the DOX release from Pd-Au@ZIF-8 NPs, but also synergistic CPTT in vitro.	[36]

(*Continued*)

Table 2. Continued.

Type of composite and surface ligand	Encapsulated Cargo	Size [nm/μm] and Zeta potential [mV]	Imaging modality	Cells and animal models	Main conclusion	Ref
ZIF-8@MPN	GOx	Before loading: ≈150 nm; ≈−16 mV After loading: ≈170 nm; −17.9 mV	MRI, FI	In vitro: Epithelial 4T1 cells In vivo: Mammary gland 4T1 cells model	– Synergistic CDT and starvation therapy was implemented by the ATP-responsive GOx@ZIF@MPN nanosystem to suppress tumor growth in vivo. – GOx reacted with the endogenous glucose in the TME to increase H_2O_2 concentration for Fenton reaction. – The released TA from the MPN degradation accelerated the conversion of Fe(III) into Fe(II) to generate ROS through the Fenton reaction of H_2O_2 and Fe(II).	[25]
ZIF-8@ZrO_2@IL	DOX	–	CT FLIRI	In vitro: Hepatoma H22 cells	– The DOX-loaded ZIF-8@ZrO_2@IL DDS exhibited effective chemo-microwave thermal tumor therapy. – The biocompatibility of ZIF-8 NPs was significantly improved by ZrO_2 modification and the ZrO_2 served as an excellent CT contrast agent. – IL acted as microwave hyperthermia agent.	[205]
ZnO@ZIF-8	–	ND	–	In vitro: Antimicrobial effects of the composite on the *E. coli*, *P. mirabilis*, *S. aureus*, and *K. pneumonia* microorganisms	– The ZnO@ZIF-8 composite was used as an antimicrobial additive in antimicrobial catheters to kill bacterial cells on the surface of the medical silicone devices. It showed promising anti-biofilm effect as well.	[206]
HMS@ZIF-8	GM	After loading: 50–200 nm; +30.1 mV	–	In vitro: Cellosaurus HEI-OC1 cells	– The GM-loaded HMS@ZIF showed a good cellular uptake in HEI-OC1 cells and good biocompatibility. – GM was released within 10 h under acidic conditions, and thus, the DDS was introduced for the therapy of Ménière's disease.	[207]
CdSNPs@ZIF-8	–	≈230 nm; ND	–	In vitro: Bactericidal effects of the NPs on the *S. aureus*, and *GFP E. coli* microorganisms	– Compared to ZIF-8 and CdSNPs alone, the CdSNPs@ZIF-8 NPs exhibited significant antibacterial activity against both GFP *E. coli* and *S. aureus*, confirming synergetic bactericidal effects of the nanocomposite.	[28]

Abbreviations: AgNPs: silver NPs; AlgDA: dopamine-modified alginate; Aln: amine-containing alendronate; AuNCs: Au nanoclusters; AuNR: gold nanorod; BSA: bovine serum albumin; C-dots: fluorescent carbon nanodots; Ce6: chlorin e6; CPDT: chemo-photodynamic therapy; CpG: cytosine phosphate-guanine; CPTT: chemo-photothermal therapy; CT: computed X-ray tomography; EGCG: epigallocatechin-3-gallate; FLIR: forward-looking infrared; FLIRI: forward-looking infrared imaging; FI: fluorescent imaging; GFP *E. coli*: green fluorescent protein-expressing *E. coli*; GM: gentamicin; GQD: graphene quantum dots; HEI-OC1: House Ear Institute-Organ of Corti 1; HMS: hollow mesoporous silica; HUVEC: human umbilical vein endothelial cell; IL: ionic liquid; IR820: indocyanine green; ITI: infrared thermal imaging; *K. pneumonia*: *Klebsiella pneumoniae*; MPN: metal polyphenol network; MRI: magnetic resonance imaging; NIR-FI: near-infrared (NIR) fluorescent imaging; *P. mirabilis*: *Proteus mirabilis*; PAA: polyacrylic acid; PAAS: poly(acrylic acid sodium salt); PAI: photoacoustic imaging; PANI: polyaniline; PDA: polydopamine; PDMAEMA: poly(2- (diethylamino)ethyl methacrylate); PEGFA: NH_2-poly(ethylene glycol)-modified FA; PEG-FA: folic acidpolyethylene glycol- maleimide; PEG-PUSeSe-PEG: polyethylene glycol-dialkyl diselenide containing polyurethane-polyethylene glycol; PersL: persistent luminescence; PMA: poly[isobutylene–alt–maleic anhydride]–graft–dodecyl; PpIX: protoporphyrin IX; QT: quercetin; RB: Rose Bengal; RSA: rat serum albumin; SERS: surface enhanced Raman spectroscopy; Si-Gd: Gd doped silicon; SiRNA: small interfering RNAs; UCNPs: upconversion NPs; WP6: carboxylated pillar[6]arene; ZnPc: zinc(II) phthalocyanine.

at the neutral pH of 7.4 after 60 h (Figure 5C). The 3-(4,5-dimethylthiazol-2-yl)-2,5-diphenyltetrazolium bromide) (MTT) cell assay on MCF-7 cells showed that DOX-loaded PAA@ZIF-8 composite had similar toxicity with the free drug at different loadings. The results also confirmed that the PAA@ZIF-8 NPs were nearly nontoxic to live cells, proving the biocompatibility of the NPs (Figure 5D). Although excellent results were obtained in vitro, the assessment of the developed NPs in vivo was not performed to identify its translational potential.

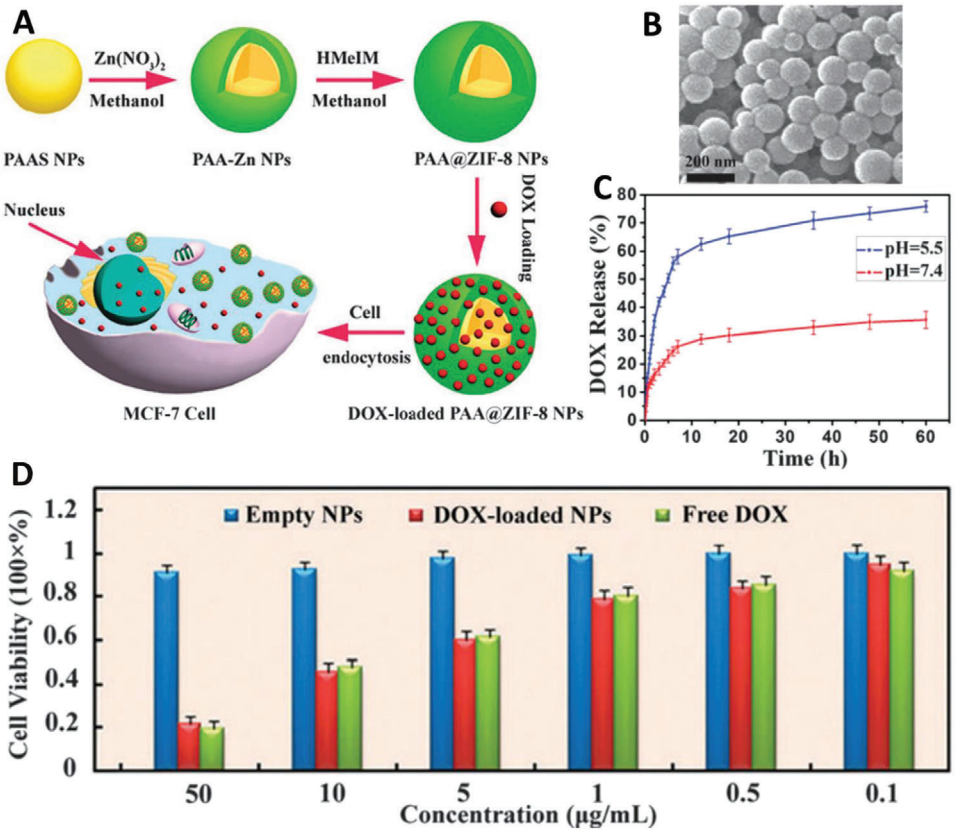

Figure 5. A) Schematic depiction of preparing PAA@ZIF-8 composite as a drug vehicle for loading and pH-controlled release of DOX. B) SEM image of PAA@ZIF-8. C) The release behavior of DOX at pH 5.5 and 7.4 at 37 °C from DOX-loaded PAA@ZIF-8 NPs. D) Cytotoxicity assessment of MCF-7 cells using different concentrations of PAA@ZIF-8 NPs, DOX-loaded PAA@ZIF-8 NPs and free DOX for 24 h. Reproduced with permission.[37] Copyright 2014, The Royal Society of Chemistry.

In 2017, the same nanocomposite was prepared by Yan et al.[34] and successfully applied as vectors to deliver DOX for anticancer therapy in mice model, greatly enhancing drug therapeutic efficacy. Toxicity assessments, including hematoxylin and eosin staining analysis on tumor and major organs, blood chemistry tests, and hematology analysis, confirmed that the nanocomposites were highly biocompatible.

As mentioned in the sections above, the MDR is one of the major challenges in the treatment of cancer chemotherapy. Co-delivering chemotherapeutic drugs and MDR gene silencing siRNAs paves a rational and effective way to circumvent the MDR shortcomings in conventional cancer chemotherapy.[210–212] In 2018, Pan et al.[35] in situ synthesized an ultrathin ZIF-8 film on carboxylated mesoporous silica (MSN-COOH) surface and prepared a novel DDS for dual delivery of siRNAs and DOX. The mesoporous channels of MSN-COOH acted as a reservoir to load DOX drug and the positively charged ZIF-8 shell was exploit for efficient loading of siRNA via electrostatic interactions and, in turn, protected siRNA from nuclease degradation. The microporous shell also acted as pore blocker to overcome premature release of DOX from the mesoporous silica channels. In vitro studies demonstrated that the positively charged ZIF-8 film promoted the uptake of the dual drug-loaded NPs in MDR cancer cells of MCF-7/ADR and SKOV-3/ADR. In fact, decomposition of the ZIF thin layer in the acidic endo-lysosome, and subsequently, the intracellular release of siRNAs and chemotherapeutic DOX, significantly enhanced chemotherapeutic efficacy. Although in vivo studies were not investigated, this study highlighted the power of ZIF-8 as a pore blocker of porous materials and an excellent platform to adsorb/control the delivery of siRNAs and its protection against nuclease degradation.[35]

As a result of the dissolution of ZIF-8 in acidic media and EDTA, various hollow structures, including hollow TiO_2,[213] polyphenol-metal networks,[214,215] ZnS nanocages,[216] and hierarchical-pore MOFs[136] have been successfully synthesized. Size and morphology-controllable hollow MSNs (HMSN), including cubic and dodecahedral morphologies ranging from ≈80 to ≈3000 nm in particle size, were fabricated by acid-degradable ZIF-8 as a self-sacrificial template (**Figure 6**A).[192] After encapsulating the HMSNs with DOX (HMSN@DOX) and subsequent coating of HMSN@DOX with ZIF-8 layer as pore blocker, the resulting pH-responsive DDS showed remarkable efficiency in killing SMMC-7721 cancer cells (human liver cancer cell lines) (Figure 6B,C).

As above-mentioned, the pore diameter of ZIF-8 is very small (3.4 Å), which is even smaller than most of the anticancer drugs.[14] Such small pores impede the high drug loading potential of NPs, and subsequently hinder highly efficient chemotherapy.[100,217] In 2018, Zhao and co-workers[181] constructed ZnO@ZIF-8 nanocomposites containing mesoporous

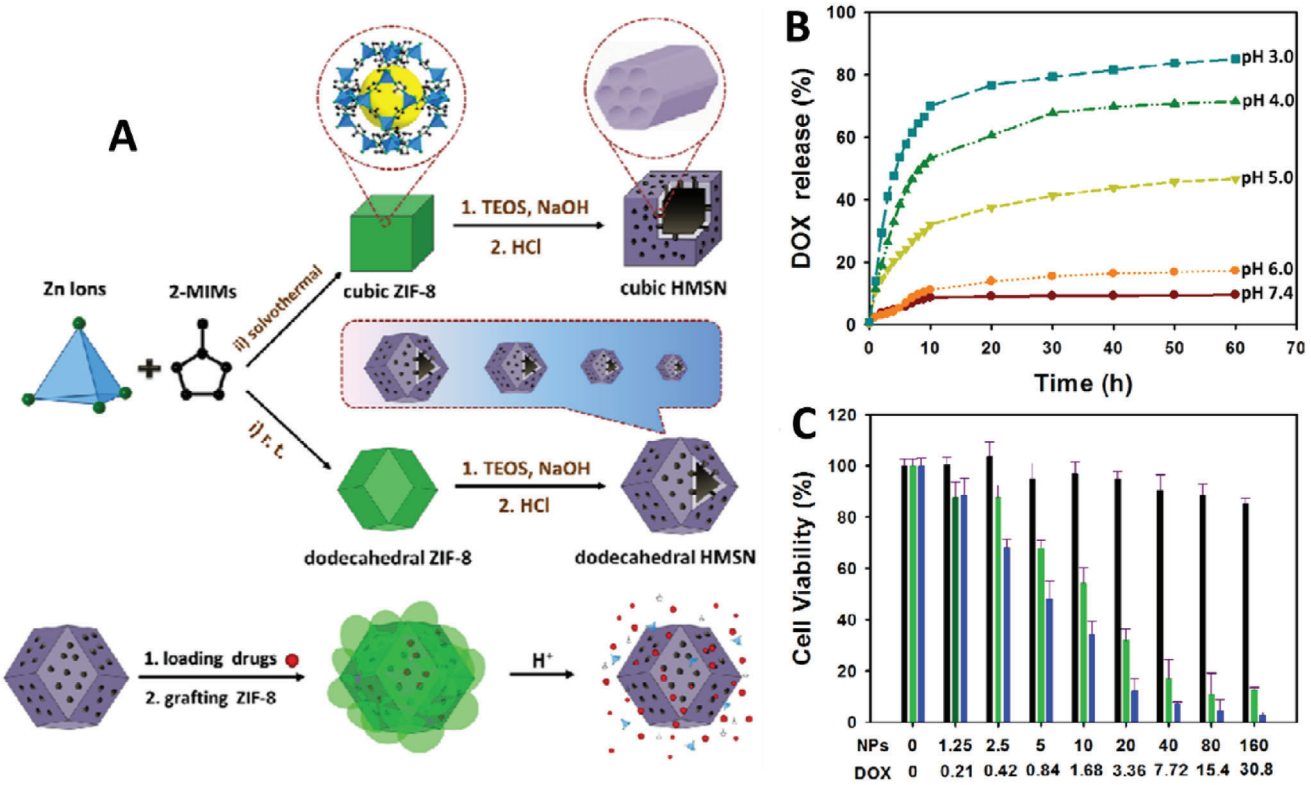

Figure 6. A) Schematic illustration of a) synthesis of size and morphology tunable HMSN, employing ZIF-8 as template and b) HMSN@DOX coated ZIF-8 as pH-responsive DDS. B) DOX release profiles from DOX encapsulated HMSN@ZIF-8 system at different pH values. C) Cell viability of SMMC-7721 cancer cells when incubated with HMSN@ZIF-8 (black), DOX (green), and DOX encapsulated HMSN@ZIF-8 (blue) for 24 h with different concentrations. Reproduced with permission.[192] Copyright 2017, The Royal Society of Chemistry.

ZnO core and ZIF-8 shell. In the mesoporous/microporous composite, the ZnO core acted as drug carrier to easily load anticancer drug, DOX, at the mesoporous channels of ZnO core and the microporous shell served as a cap to prevent premature release of chemotherapeutic DOX at physiological environment. In addition, the ZnO core not only functioned as a drug carrier, but also used as a Zn ion source to create the ZIF-8 shell. The authors showed that more than 80% of the anticancer drugs were released at the pH value of 5.5. This was mainly attributed to the dissolution of ZnO core and ZIF-8 shell in acidic conditions, endowing the composite with good pH-responsive drug release behavior. The MTT assay in HeLa cells showed that the toxicity of DOX-encapsulated ZnO@ZIF-8 was significantly higher than that of the composite alone and free DOX, which was mainly due to the synergistic toxic effect of released anticancer DOX and ZnO@ZIF-8 decomposition under acidic TME.[181] A similar approach was reported by Zhou et al.[186] in which diselenide-containing triblock copolymer (PEG-PUSeSe-PEG) was employed as a drug carrier and ZIF-8 acted as a gatekeeper to delay drug release from the copolymer micelles. The selenium-containing polymers not only served as DOX storage agent, but also it was disassembled in the presence of redox agents (H_2O_2/GSH), which are overproduced in cancer cells. Although their cancer therapy studies were conducted in vitro, the design/fabrication of such redox/pH-sensitive nanocomposite with good loading capacity, controllable drug release property and excellent biocompatibility paved a rational way to fabricate multiresponsive DDSs in cancer treatment.

As above-mentioned, another limitation of ZIF-8 is the poor water dispersibility and inaccessibility of its free surface functional groups, preventing its further applications toward advanced biomedical goals. Therefore, the construction of water-dispersible targeted ZIF-8 based DDSs is of particular importance, especially in chemotherapy applications.[102] Macrocyclic water-soluble carboxylated pillar[6]arene (WP6) was used to functionalize ZIF-8@DOX via the coordination between metal nodes of the drug-loaded ZIF-8 and the carboxyl group of WP6 to improve water dispersibility of the DDS.[174] In addition, through host-guest complexation between the WP6 and a galactose derivative as targeting ligand, a highly dispersed/targeted DDS was prepared to increase the anticancer efficiency of ZIF-8@DOX NPs toward galectin overexpressing hepatoma cancer cells. Confocal laser scanning microscope studies and flow cytometry showed that the pH-responsive DDS took up by HepG2 cells and DOX were released efficiently within the cells. This study was a pioneering work on the fabrication of rational targeted pH-responsive water dispersible drug carriers using the combination of supramolecular hybrid structures and ZIF-8 for potential cancer therapy.

Chemodynamic therapy (CDT) as an emerging and unique therapeutic strategy has also been recently developed for cancer therapy through reactive oxygen species (ROS) generation

mediated by Fenton reaction.[218] In this process, •OH radicals can directly be generated by the Fenton reaction of overproduced endogenous H_2O_2 and metal ions catalysts, e.g. Fe(II) or Cu(I), in tumor sites, leading to apoptosis induction and tumor growth inhibition.[218–220] However, one of the main obstacles of cancer CDT is the insufficient concentration of H_2O_2 in the TME that causes poor anticancer performance of this technique.[221] In 2019, the proof-of-concept of singlet oxygen-based CDT for selective tumor eradication using hypochlorous ion (ClO^-)-loaded ZIF-8 was proposed by Zhao co-workers (**Figure 7**A).[184] ClO^- could react with H_2O_2 in TME to stoichiometrically generate singlet oxygen and kill cancer cells.[222] On the other hand, the enrichment of H_2O_2 in TME was achieved by simultaneous intraperitoneal (i.p.) administration of the ascorbate (Asc) to enhance the efficiency of CDT. It was shown that Asc could promote H_2O_2 accumulation in the extracellular fluids of solid tumors at its pharmacological concentration.[223,224] They showed combinational ClO^- and Asc delivery via intravenous (i.v.) and i.p. administration, respectively, is a potent CDT system for selective cancer therapy in vivo (Figure 7A). The ClO^--loaded ZIF-8 (ClO@MOF) was prepared in a one-pot reaction and further coated with poloxamer 188 (Pluronic F68) to increase the stability of the nanosystem. The hydrodynamic size of the F68-modified ClO@MOF (ClO@MOF/F68) NPs was 177.9 ± 13.2 nm (Figure 7B). As shown in Figure 7C, the prepared NPs exhibited a slightly positive surface charge. Significant amounts of ROS even at the absence of Asc was observed in murine mammary carcinoma 4T1 cells treated by ClO@MOF/F68 NPs (Figure 7D), attributed to the reaction of ClO^- with intracellular H_2O_2. Interestingly, the cells co-treated by ClO@MOF/F68 NPs plus free Asc generated the highest level of ROS, confirming Asc-mediated elevation of intracellular H_2O_2 level to boost the ROS concentration. Compared to ClO@MOF/F68 alone, the co-supplement of ClO@MOF/F68 with Asc remarkably reduced the cell viability of 4T1 cells due to the enhanced ROS production (Figure 7E). In addition, significant GSH reduction was observed using the combination of ClO@MOF/F68 and Asc in vitro (Figure 7F). GSH is a major antioxidant inside the tumor cells, which hinders the performance of ROS-based nanomedicines to treat cancer. In agreement with the in vitro cytotoxicity experiments, in vivo antitumor studies on 4T1 tumor-bearing xenograft mice showed that the combinational formulation, i.e., ClO@MOF/F68 plus Asc, exhibited significant anti-tumor activity than the other groups (Figure 7G). Altogether, this study paves new ways to overcome the side effects of traditional PDT and sonodynamic therapy (SDT), including the limited tissue penetration of light in PDT, low quantum yield of singlet oxygen in SDT, and the toxicity of photosensitizers/sonosensitizers, to develop effective ROS-based antitumor therapy with lower side-effects.

4.2. Combined Therapy by ZIF Nanocomposites

Although monotherapy of cancer by novel DDSs enhances therapeutic efficiency and decreases side effects of toxic chemotherapeutic drugs, still the MDR of cancer cells in chemotherapy is a big hurdle, remaining as an important challenge in effective cancer treatment.[131,225] Therefore, the construction of multifunctional cancer treatment systems, combining multiple therapeutic modalities, including chemotherapy, PTT and PDT in a single system for more effective cancer treatment has been an imperative goal.[3,17,21,226–229] Herein, we will discuss about the ZIF-based multifunctional nanocomposites developed very recently for combined cancer therapy.

PTT, a light-induced method, is a minimally invasive treatment that employs the photothermal agents located in tumors to convert NIR energy into heat, leading to irreversible cellular damage and subsequent tumor killing.[230] Various photothermal agents including gold NPs,[231] MXenes,[232,233] bismuth-containing nanomaterials,[234–236] organic NPs,[237] liquid metal nanodroplets,[238] and 2D noncarbonaceous materials[239] have been developed for PTT. Simultaneous chemo-photothermal therapy (CPTT) can be realized by combining photothermal agents and chemotherapeutic drugs within ZIFs. Tian et al.[185,195] developed DOX-encapsulated ZIF-8/graphene quantum dot (GQD) nanocomposites, utilizing a one-pot method with a particle size of 50–100 nm, to achieve synergistic photothermal therapy and controlled drug delivery (**Figure 8**A). Since ZIF-8 is stable under neutral conditions (pH 7.4) and can disintegrate under acidic environment, DOX release was much faster at acidic condition than in neutral environment from the DOX@ZIF-8/GQD (Figure 8B). The drug-loaded NPs efficiently converted NIR irradiation into heat, which was attributed to the high photothermal conversion efficiency and excellent thermal conductivity of GQD as a photothermal agent (Figure 8C). In vitro studies on the viability of 4T1 breast cancer cell line showed a synergistic effect to kill the cancer cells, owning to the photothermal effect of GQDs and the pH-dependent DOX release from the multifunctional DDS, holding great promise for CPTT of cancer (Figure 8D).

Wang et al.,[176] for the first time, demonstrated that copper sulfide (CuS)-incorporated ZIF-8 (CuS@ZIF-8) NPs decomposed under physiological conditions, i.e., pH 7.4, while exposed to NIR laser irradiation, which was related to the uneven thermal expansion of ZIF-8. The CuS@ZIF-8 nanosystem was prepared by PVP-mediated in situ growth of ZIF-8 around the CuS NPs. The incorporation not only did not alter the low pH-degradability of ZIF-8 NPs, but also boosted a synergistic chemo-photothermal therapeutic effect on tumor cells killing after DOX loading into the CuS@ZIF-8 nanocomposite.

Recently, noble bimetallic nanomaterials have gained great interest as promising photothermal agents owing to the advantages of facile synthesis, chemical inertness, and high photothermal conversion efficiency.[240,241] However, their unstable structures and shapes, and potential biotoxicity have limited their biomedical applications.[242] As a result of the low toxicity of palladium (Pd) at concentrations required for photothermal therapy, DOX-loaded Au-Pd bimetallic nanocomposites encapsulated within ZIF-8 (Au-Pd/DOX@ZIF-8) were used to fabricate a multifunctional DDS for synergistic in vitro CPTT of cancer cells (**Figure 9**A).[36] Pd NPs were first prepared and then covered by Au nanosheets. To obtain Au-Pd/DOX@ZIF-8 nanocomposites, the Au-Pd NPs and DOX were synchronously encapsulated by ZIF-8 in a single step. The Pd-Au was able to convert NIR light into heat and accelerate the release of chemotherapeutic DOX through local hyperthermia. Furthermore, the ZIF-8 shell was degraded at acidic tumor microenvironment, leading to the release of encapsulated DOX. Such a synergistic scenario introduced a cytotoxic nanosystem against SMMC-7721 cells, which was not attainable

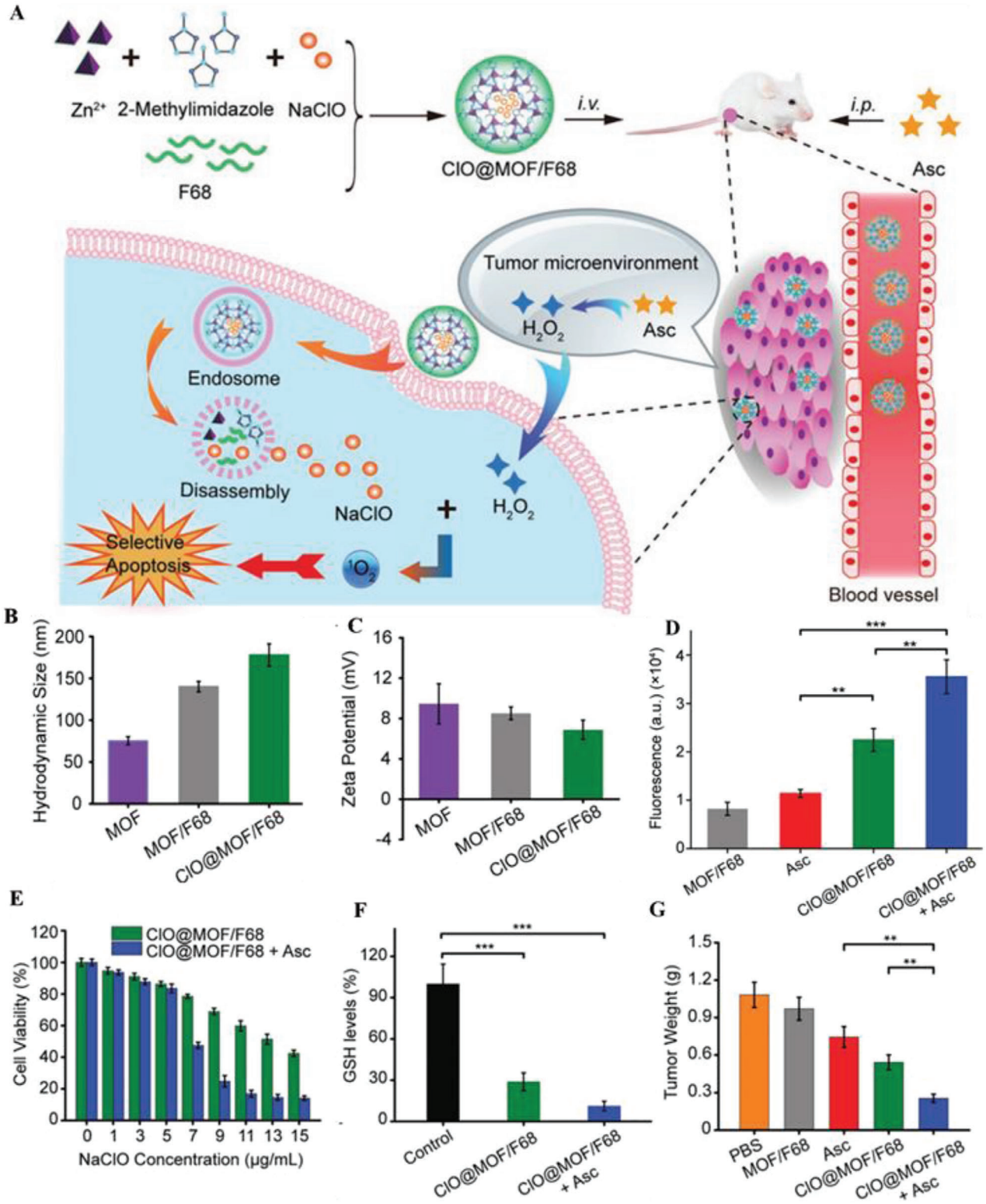

Figure 7. A) Schematic illustration of ClO@MOF/F68 synthesis and depiction of singlet oxygen-based CDT through the i.v. delivery of ClO@MOF/F68 NPs plus concurrent i.p. administration of Asc and singlet oxygen production by hypochlorous ion for selective apoptosis. B) Hydrodynamic size and C) zeta potential of MOF, MOF/F68, ClO@MOF/F68 NPs. D) The intracellular singlet oxygen generation in 4T1 cells treated with the different NPs using fluorescence intensity measurement. E) Cell viability of 4T1 cells incubated with the NPs. F) The relative GSH level in the 4T1 cells treated by different NPs. G) Measurement of tumor weight in 4T1 tumor-bearing mice treated with different formulations at the end of treatment. Reproduced with permission.[184] Copyright 2019, Wiley-VCH.

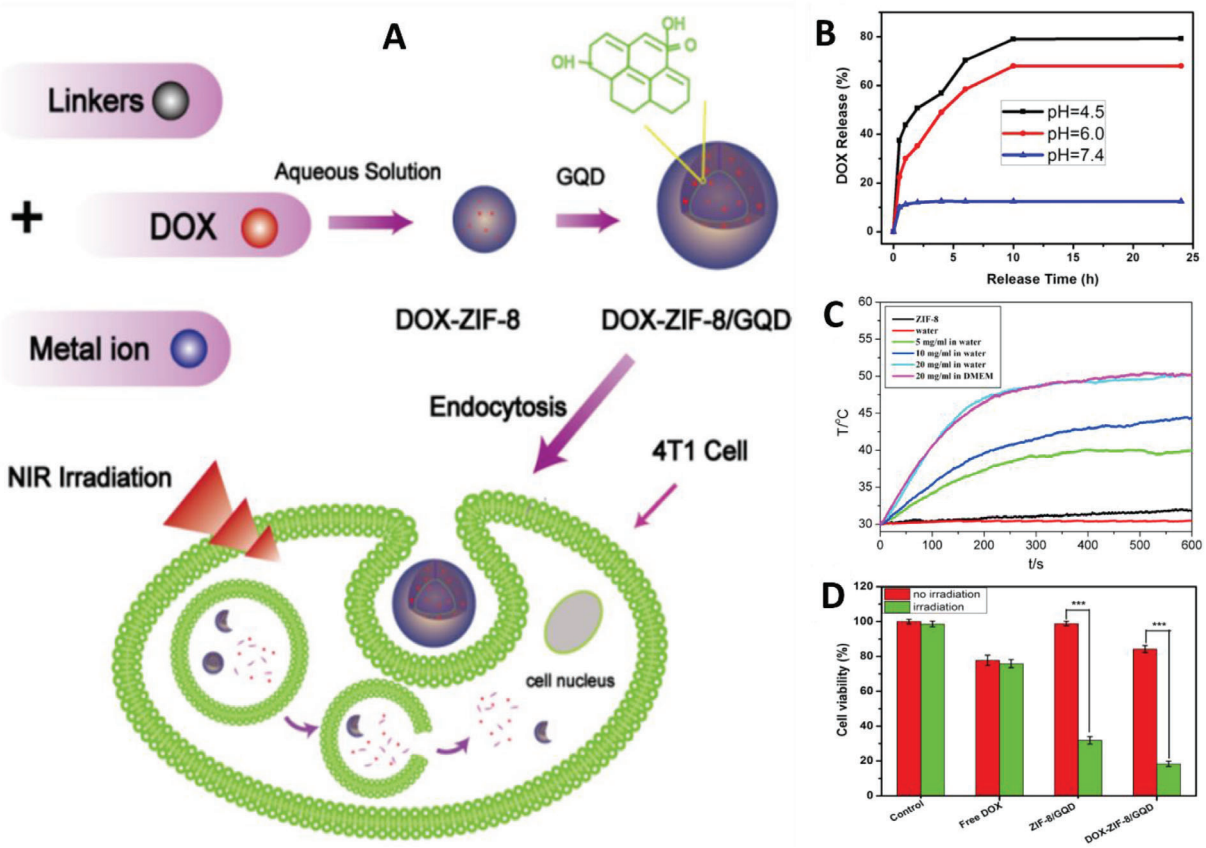

Figure 8. A) Schematic illustration of the preparation of DOX@ZIF-8/GQD and synergistic photothermal therapy and DOX delivery. B) DOX release profiles of DOX@ZIF-8/GQD at different pHs. C) Photothermal effects of DOX@ZIF-8/GQD in water and Dulbecco's Modified Eagle Medium (DMEM) at different concentrations employing 808 nm laser irradiation at 1.5 W cm^{-2}. D) Cell viability of 4T1 cells after 8 h of incubation with free DOX, ZIF-8/GQD, and DOX-ZIF-8/GQD without and with 808 nm laser irradiation. Reproduced with permission.[185] Copyright 2017, American Chemical Society.

via a single modality. Cancer cell viability reached 11% after pretreating with Au-Pd/DOX@ZIF-8 (80 μg mL^{-1}) for 24 h under irradiation of NIR laser for 10 min, which the viability was lower when no pretreatment was used, confirming the accelerated release of the encapsulated DOX under laser irradiation.

Although metal-based NIR adsorbing agents have extensively been utilized for PTT, they are expensive and suffer from low photostability under long-term laser irradiation.[36,233,243–245] Organic polymers, such as polyaniline (PANI)[243,246–248] and polypyrrole[249–252] have good biocompatibility, low cost, high mechanical flexibility and strong NIR absorption.[243,249] These features endow them with excellent capacities to be exploited as alternative photothermal agents in PTT.[253] In 2018, Silva et al.[183] synthesized PANI-decorated ZIF-8 NPs (PANI@ZIF-8) and after 5-FU drug loading, this multifunctional DDS was used as an efficient CPTT platform for in vitro cancer therapy (Figure 9B). The authors showed that the release of 5-FU from the polymer-coated ZIF-8 reached to 68% at pH 5.2, while at the same condition and upon NIR laser irradiation (980 nm, 0.8 W cm^{-2}), the drug release was ≈80%. Therefore, the PANI not only accelerated the drug release, but also served as NIR-light to heat conversion agent to kill cancer cells.

It has been reported that unmodified ZIF-8 has high toxicity, which limits its in vivo applications in the design/fabrication of advanced DDSs.[22,100] Therefore surface modification of ZIF-8 is an imperative task to tune/improve the biocompatibility of this carrier. Using cytotoxicity and in vivo acute toxicity assessments, Wu et al.[22] demonstrated that the biosafety of ZIF-8 NPs was significantly improved by PDA coating. The PDA also acted as photothermal agent to achieve PTT. To precisely control the rate of drug release from the DOX-loaded ZIF-8/PDA NPs, the authors used a phase-change material (PCM), i.e., tetradecanol, for NIR-mediated drug release. As the melting point of tetradecanol is 38–40 °C and it does not dissolve under physiological conditions, a more control on DOX release was obtained upon NIR irradiation via tetradecanol dissolvation by increasing local temperature through light-to-heat conversion effect of PDA. Therefore, a controlled CPTT was successfully achieved by the biocompatible DOX-loaded PDA-PCM@ZIF-8 in vivo. The cytotoxicity studies in HepG2 cells indicated that the ZIF-8 itself has high cytotoxicity, while the PDA@ZIF-8 and PDA-PCM@ZIF-8 had favorable biocompatibility. When 15 mg kg^{-1} of ZIF-8 was injected to the mouse through the i.v. route, the survival rate was only 60% and an abnormality was seen in the liver of the mouse after dissection. In contrast, in the case of PDA@ZIF-8, the survival rate was 80% for the administration dose of 75 mg kg^{-1}, again proving increased biocompatibility after surface modification.

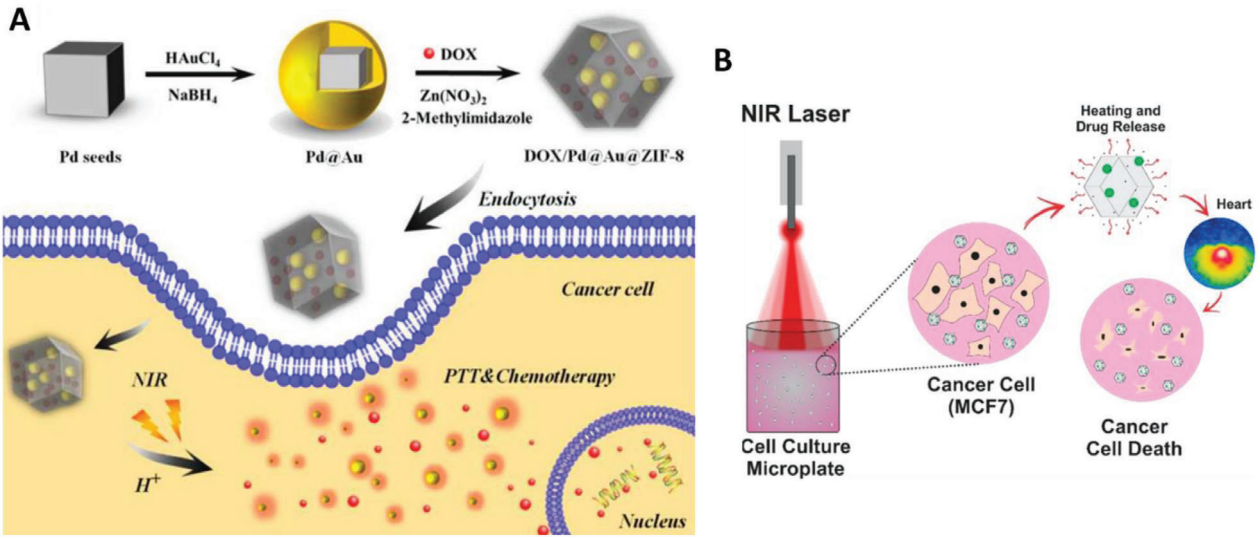

Figure 9. A) Schematic illustration of the fabrication of Au-Pd/DOX@ZIF-8 and its application in synergistic CPTT of cancer cells. Reproduced with permission.[36] Copyright 2017, The Royal Society of Chemistry. B) Schematic application of 5-FU-loaded PANI@ZIF-8 in CPTT. Reproduced with permission.[183] Copyright 2018, American Chemical Society.

The same group used ZrO_2 coating onto the surface of ZIF-8 NPs to improve the biocompatibility of the NPs.[205] The ZrO_2 shell not only boosted biocompatibility of ZIF-8, but also served as an excellent CT contrast agent, owning to the high atomic number of Zr element. In addition to DOX loading, ionic liquid was also loaded on the surface of ZIF-8@ ZrO_2 for synergistic chemo/microwave thermal therapy of cancer.

Successful in vitro and in vivo synergistic CPTT was reported by loading DOX into AuNR coated ZIF-8 (AuNR@ZIF-8-DOX) NPs, and controlled release under NIR irradiation (**Figure 10**A). In this study by Li et al.,[60] the authors showed NIR and pH dual stimuli-responsive DOX release from AuNR@ZIF-8-DOX (Figure 10B,C). The core–shell nanostructures significantly induced photothermal anticancer effect both in vitro and in vivo (Figure 10D,E). As a result of the high light-to-heat conversion capability of AuNR, the AuNR@ZIF-8-DOX NPs possessed the highest toxicity at cellular and animal models as compared to the single therapeutic treatment approaches, i.e., separate chemotherapy and PTT. This study introduced the AuNR@ZIF-8-DOX NPs as a powerful multifunctional DDS for combined CPTT of cancer.[60]

The combination of CDT and PDT (CPDT) has emerged as a new strategy for cancer treatment.[200,254–256] However, overexpression of GSH and hypoxia in TME are two main obstacles that severely affect the successful treatment of cancer through the combined strategies.[257] Recently, O_2-Cu/ZIF-8@Ce6/ZIF-8@F127 nanocomposite was prepared to simultaneously decrease hypoxia and GSH level for enhanced CPDT.[258] It is noteworthy that one of the important features of ZIFs is its gas storage capability.[6] ZIF-90 as a member of ZIFs has been reported as an O_2 carrier to overcome tumor hypoxia for efficient PDT.[200] However, in the O_2-Cu/ZIF-8@Ce6/ZIF-8@F127 nanocomposite, ZIF-8 acted as O_2 carrier and the doped Cu^{2+} in the ZIF network doubled the O_2 loading capacity of ZIF-8 to increase the amount of ROS generated by PDT using Ce6 photosensitizer under 650 nm laser irradiation. Moreover, the released Cu^{2+} reduced GSH through oxidation reaction and the produced byproduct, i.e., Cu^{+} acted as CDT agent and generates cytotoxic •OH via Fenton-like reaction by reacting with H_2O_2, which was overexpressed in tumor cells.[259,260]

In addition to cancer therapy, ZIF-mediated combined therapy has been proposed for other diseases.[26,261,262] For example, endophthalmitis is a disease that occurs in many intraocular surgeries, particularly cataract surgery due to the localization of the pathogenic microorganisms in the damaged tissue. This infection leads commonly to intraocular inflammation, uveitis, and damage to the vitreous cavity within the eyeball.[263,264] Recently, the combination of chemotherapy and PDT was used for successful inhibition of infectious endophthalmitis by ZIFs.[262] To this end, ammonium methylbenzene blue (MB)-loaded ZIF-8-PAA (ZPM) was first prepared, followed by AgNPs incorporation, using dopamine as reducing agent and then further modification with Van/NH_2-PEG to give NIR and pH-responsive ZIF-8-PAA-MB@AgNPs@Van-PEG (ZPMAVP) nanocomposite for the treatment of bacterial endophthalmitis (**Figure 11**A). The MB acted as photosensitizer antibacterial agent and PAA endowed the nanocomposite with higher pH-responsive properties and better drug loading capacity. The bactericidal and antiadhesive activities of the NPs were investigated by agar plate counting method and SEM imaging. In the case of ZPM NPs, treating with three kinds of bacteria, i.e., *S. aureus*, *E. coli*, and MRSA, resulted in no apparent decrease of bacterial growth when laser treatment was not applied. In contrast, an obvious reduction of bacteria was observed under laser irradiation at 650 nm, confirming the high efficiency of the PDT. As a result of the antibacterial property of AgNPs, the Ag-incorporated-ZPM (ZPMA) showed higher bactericidal effects. It has been reported that Van, which is a highly efficient antibiotic can act as a targeting molecule, especially towards Gram-positive bacteria.[265] As shown in Figure 11B–D, the grafting of the targeting molecule and hydrophilic PEG chain on ZPMA further increased the bacteria-killing efficiency in all three

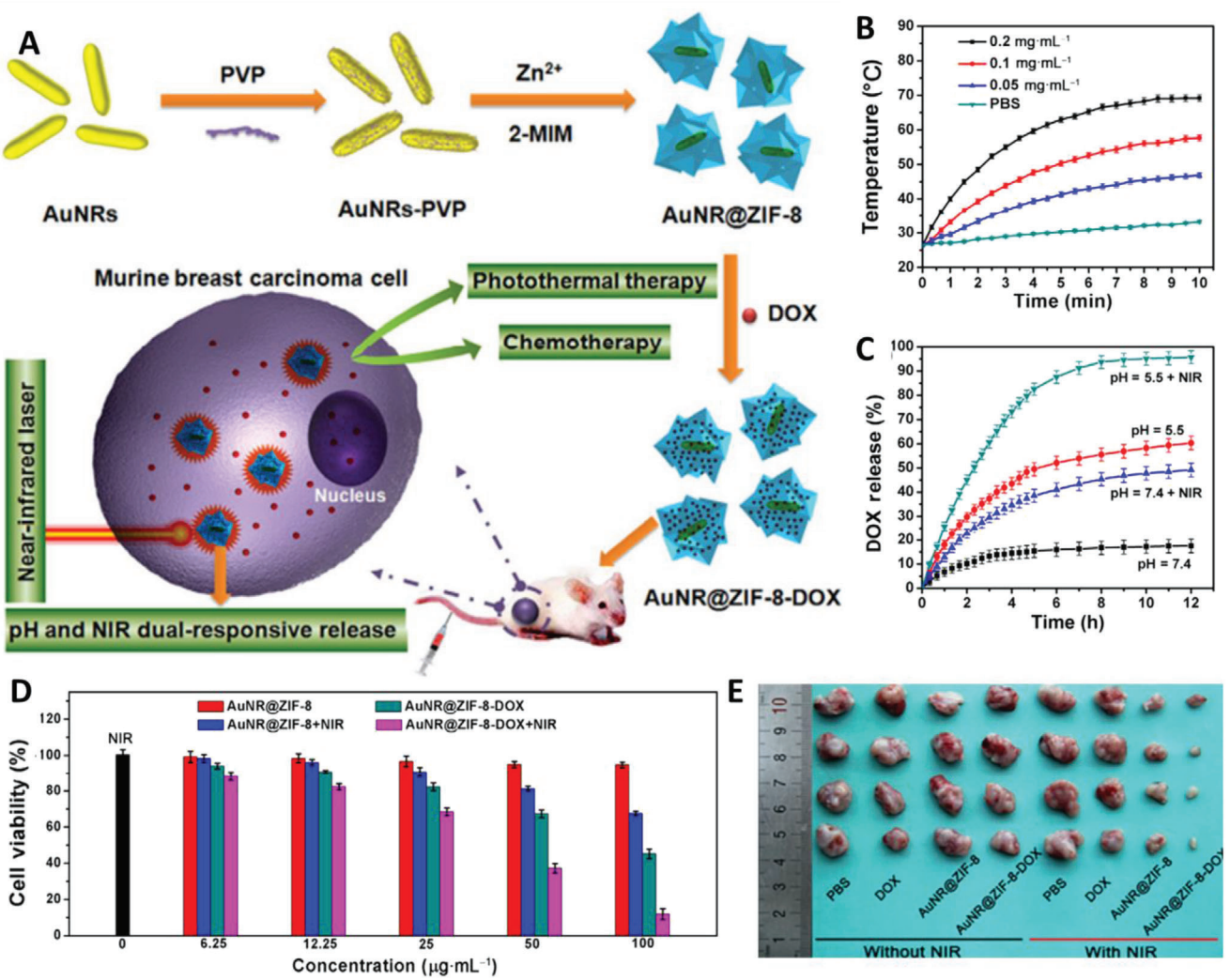

Figure 10. A) Schematic illustration of AuNR@ZIF-8-DOX for synergistic cancer CPTT. B) Photothermal heating curves of AuNR@ZIF-8 core–shell nanostructures at different concentrations of the NPs in PBS solution under NIR laser irradiation (1 W cm^{-2}). C) pH- and NIR-dependent DOX release profiles from AuNR@ZIF-8-DOX NPs with and without NIR laser irradiation. D) CCK-8 viability assay of 4T1 cells under different treatment conditions. E) In vivo synergistic chemo-photothermal efficiency of AuNR@ZIF-8-DOX. Digital photo of excised tumors from sacrificed mice in 4T1 tumor-bearing mice with different treatments. Reproduced with permission.[60] Copyright 2018, The Springer Nature.

kinds of bacteria. SEM imaging of the remaining/corpse bacteria on silicon wafers confirmed the positive impact of laser treatment, i.e., PDT, on biofilm eradication function of ZPM, ZPMA, and ZPMAVP to decrease the number of adhered bacteria on the surface. The antibacterial mechanism of the ZPMAVP NPs was attributed to the generation of ROS by Ag^+ released from the NPs and also through the PDT. In vivo antibacterial tests were carried out on bacterial endophthalmitis model constructed in the eyes of New Zealand White Rabbit. Compared to the eyes treated by Van, the symptoms of endophthalmitis in the groups treated by ZPMAVP NPs under laser irradiation were mild and conjunctival congestion and anterior chamber empyema were not obviously observed (Figure 11E,F). The number of bacteria after 7 days in the vitreous humor of the eyeball of the rabbit cultured on an agar plate and administrated with Van and ZPMAVP/laser groups was less than 1×10^5 and 1×10^3 CFU mL^{-1}, respectively, while this number in the control group was more than 1×10^{10} CFU mL^{-1} (Figure 11G). Collectively, the in vitro and in vivo antibacterial experiments demonstrated the effect of the PDT on endophthalmitis therapy, opening new ways in the PDT-mediated treatment of eye diseases due to naturally good light transmission of the eyes. This nanosystem not only introduced ZIF-8 as a biocompatible carrier, but also microporous structure of ZIF-8 was reported as a molecular cage to prevent the self-aggregation of MB as photosensitizer. Recently, this property of ZIF-8 has been used in encapsulating hydrophobic PS squaraine (SQ) to enhance PDT efficacy of SQ against drug-resistant planktonic bacteria and its biofilm.[116]

4.3. Theranostics Applications of ZIF Nanocomposites

Nanotheranostic is the integration of therapeutic and diagnostic modalities into a single nanosystem to achieve imaging-guided therapy.[266] Such nanoplatforms have received a great

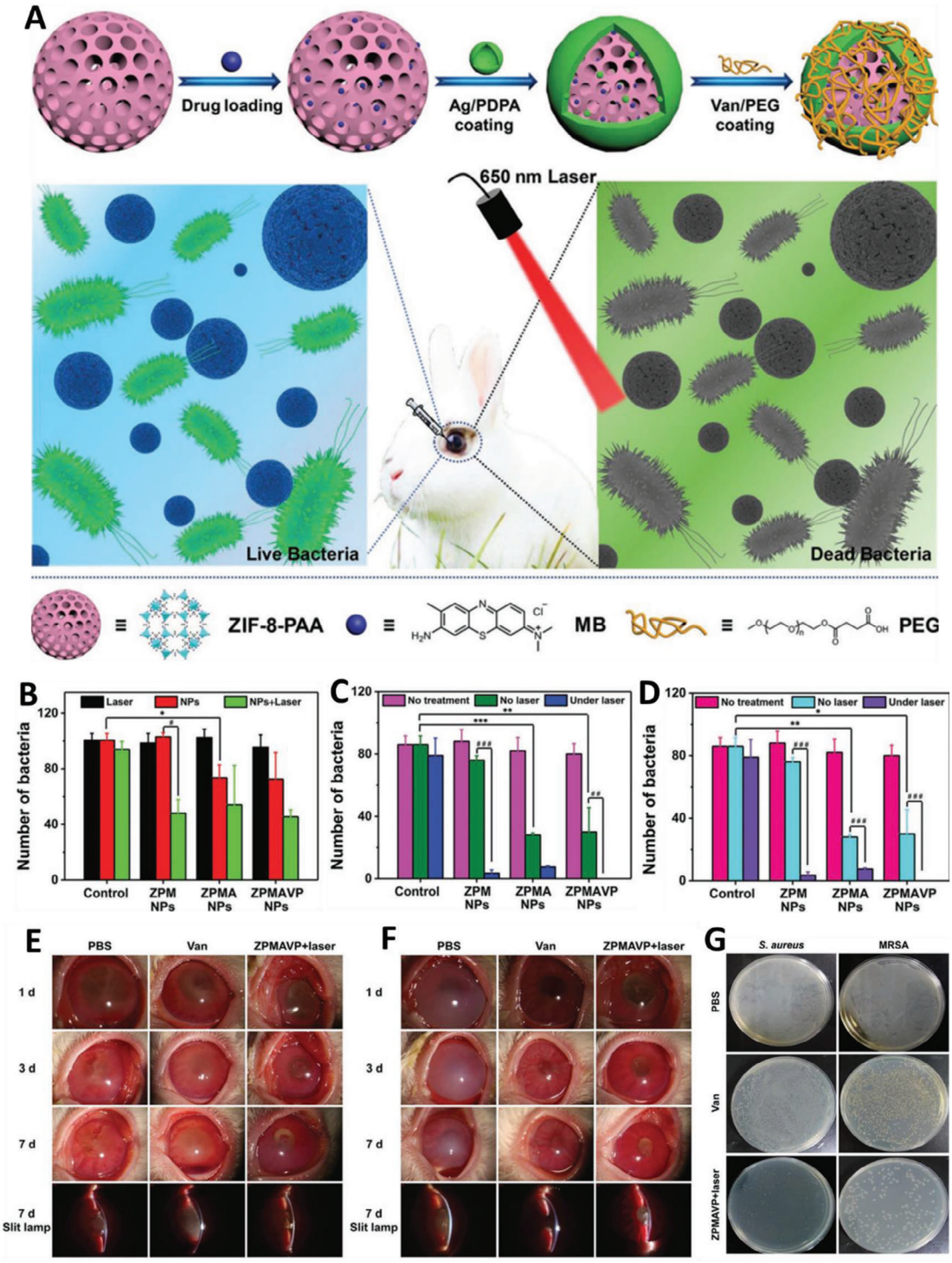

Figure 11. A) Schematic preparation of ZPMAVP nanosystem and its application in combined CPDT of endophthalmitis. Bacterial viability of B) *S. aureus*, C) *E. coli*, and D) MRSA, using plate counting methods ($^{\#}p < 0.05$, $^{\#\#}p < 0.01$, $^{\#\#\#}p < 0.001$, $^{*}p < 0.05$, $^{**}p < 0.01$, $^{***}p < 0.001$) after treatments with ZPM NPs, ZPMA NPs, and ZPMAVP NPs. Photographs and slit lamp micrographs of endophthalmitis caused by E) *S. aureus* and F) MRSA at days 1, 3, and 7 after treatment with PBS, Van, and ZPMAVP+laser. G) Agar plate culturing of *S. aureus* and MRSA at day 7 available in the vitreous fluid after treatment with PBS, Van, and ZPMAVP+laser NPs. The power of the laser in all the experiments was 202 mW cm^{-2}. Reproduced with permission.[262] Copyright 2019, Wiley-VCH.

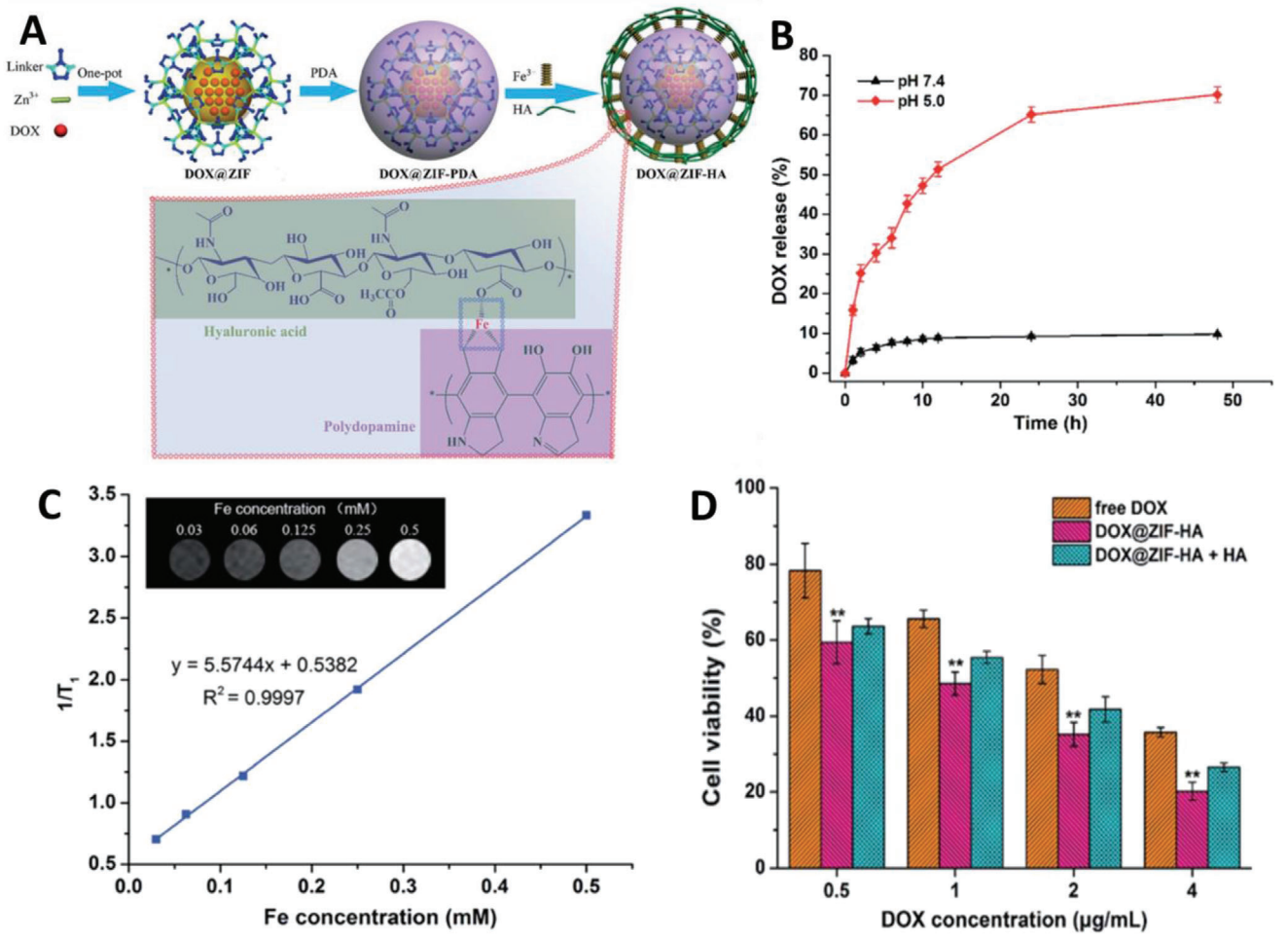

Figure 12. A) Schematic illustration of the construction of DOX@ZIF-HA and Fe^{3+}-mediated coordination interaction between PDA and HA. B) DOX release profiles of DOX@ZIF-HA under different pH conditions. C) The in vitro MR imaging ability of DOX@ZIF-HA. The linear fitting of 1/T1 as a function of Fe concentration. The inset shows corresponding T1-weighted MR images of DOX@ZIF-HA at different Fe concentrations. D) The CCK-8 assay of PC-3 cells treated with free DOX, DOX@ZIF-HA, and DOX@ZIF-HA plus free HA at different drug concentrations. Reproduced with permission.[194] Copyright 2018, The Royal Society of Chemistry.

promise in real-time monitoring and treating cancer and other hard-to-treat diseases, while playing a pivotal role in the development of personalized medicines.[266] Recently, nanoscaled MOFs (NMOFs), including ZIFs, have emerged as one of the most promising nanotheranostic systems due to their huge porosity, large surface area, tunable functionality, and good biocompatibility/biodegradability.[4,21,45,200,267–270] Single or even multimodal imaging by ZIF-based theranostic systems has been recently studied.[24,61,194] Herein, we discuss how these multifunctional nanosystems work to simultaneously monitor and treat cancer. Fluorescent carbon nanodots (C-dots) as safe imaging agents, which had strong fluorescence intensity were encapsulated within ZIF-8 and were used as theranostic after 5-FU loading for simultaneous pH-responsive DDS and fluorescence imaging of cancer cells in vitro.[61] In the study, it was also shown that, using a facile two-step method, the size of the ZIF-8 NPs was tuned by changing the initial concentrations of 2-MeIm and Zn^{2+} ions and it was confirmed that fluorescence intensity C-dots encapsulated ZIF-8 was adjustable by varying the amount of C-dots.

Although there are many examples on the construction of core–shell structures using ZIFs for theranostic applications, these systems might suffer from complexity and high cost of the methods. Surface modification of ZIFs is an alternative approach to incorporate imaging agents on ZIFs to make multifunctional theranostic nanosystems.[21] Similar to the report of Zheng et al.[100] discussed in the previous sections, Shu et al.[194] loaded DOX into ZIF-8 through a one-pot process and then the resultant DOX@ZIF-8 was subsequently coated with PDA. In order to add a magnetic resonance imaging (MRI) agent, the PDA coated DDS was successively chelated with Fe^{3+} and further conjugated with HA (DOX@ZIF-8-HA) (**Figure 12**A). The HA acted as targeting ligand toward the PC-3 prostate cancer cell line, proved by confocal laser scanning microscopy and flow cytometry. Innate acid degradability of ZIF-8 caused pH-responsive release of DOX from the multifunctional DDS (Figure 12B). Furthermore, the Fe^{3+} functioned as a contrast agent for MRI (Figure 12C). Therapeutic activity of DOX@ZIF-8-HA was assessed using the cell counting kit-8 (CCK-8), demonstrating targeting

ability of the nanosystem toward CD44 overexpressed PC-3 cells and improving its intracellular uptake and enhancing its in vitro chemotherapeutic efficacy, as compared to the free DOX. (Figure 12D). In addition, free HA had a negligible impact on the therapeutic efficacy of DOX@ZIF-HA.

In addition to the above-explained example, diverse single modal imaging agents, such as upconversion NPs (UCNPs),[198,200,201] CuS NPs,[175] cobalt ferrite ($CoFe_2O_4$) NPs,[203] cadmium sulfide (CdS) NPs,[28] and chromium-doped zinc gallogermanate (ZGGO) NIR persistent luminescent NPs,[204] have been employed to prepare core–shell nanotheranostics after their coating by ZIFs and encapsulation of chemotherapeutic drugs.

As a result of the high effectiveness, noninvasiveness, and concurrent fluorescence imaging property of PDT, this method has gained great attention to be part of theranostic systems for cancer therapy. A PS, oxygen, and light are key components for successful PDT.[271] However, one of the main challenges in PDT is the self-aggregation of PSs in aqueous environments because of its hydrophobic nature, leading to quick quenching of PDT and poor efficiency of the systems.[272] Xu et al.[177] utilized ZIF-8 NPs as a stabilizer to encapsulate and separate water-insoluble photosensitizer zinc(II) phthalocyanine (ZnPc) molecules inside nanoscale molecular cages of ZIF-8 to maintain the PS as monomeric in aqueous solution for efficient PDT. The ZnPc@ZIF-8 nanosystem showed highly efficient cytotoxic singlet oxygen generation capability and excellent photodynamic activity towards HepG-2 cancer cells. This system also exhibited red fluorescent emission after endocytosing by the cancer cells, paving a way to overcome self-aggregation/bioavailability problems of PSs for imaging-guided PDT. It should be noted that the self-aggregation of PSs and hypoxia at the tumor sites are the main limitations in the development of cancer PDT methods. As a result of the degradation of manganese oxides (MnO_2) into Mn^{2+} ions in an acid solution of H_2O_2, such chemistry can boost the concentration of O_2 in TME, therefore increasing the efficiency of PDT process.[273–275] In addition, released Mn^{2+} ions were exploited as contrast agent for MRI. Utilizing the nanoenzyme-like/O_2-generating behavior of MnO_2, BSA-MnO_2 NPs were loaded onto the surface of Ce6, a hydrophobic photosensitizer, encapsulated-ZIF-8 (BSA-MnO_2/Ce6@ZIF-8) NPs for MRI-guided PDT of cancer (**Figure 13**A).[276] The successful synthesis of BSA-MnO_2/Ce6@ZIF-8 was confirmed by TEM, dynamic light scattering (DLS) and energy-dispersive X-ray spectroscopy (EDS) (Figure 13B–D). For example, EDS revealed the presence of O, N, Zn, S, and Mn, proving the existence of BSA-MnO_2 NPs on the surface of Ce6@ZIF-8 NPs (Figure 13C). As shown in Figure 13E, BSA-MnO_2/Ce6@ZIF-8 NPs were able to produce more oxygen at pH 5.0 than the pH 7.4. Such behavior was attributed to the simultaneous presence of H^+ and H_2O_2 that triggered the catalase-like activity of nanosystem, confirming the O_2-generating capability of the BSA-MnO_2/Ce6@ZIF-8 NPs to relieve hypoxia in cancer therapy using PDT methods. Both cell viability and in vivo tumor growth inhibition studies confirmed the outstanding killing effect derived from the PDT under 650 nm NIR laser irradiation (Figure 13F–H). Moreover, MRI after injection of the NPs proved that the BSAMnO_2/Ce6@ZIF-8 could effectively accumulate in the tumor sites, holding great promise in MRI-guided cancer therapy (Figure 13I).[276]

Visible-light photosensitizer graphitic carbon nitride (g-C_3N_4) nanosheets, as a photodynamic therapeutic agent, were encapsulated within ZIF-8 by growing ZIF-8 components in the presence of g-C_3N_4 nanosheets.[180] Chemo-photo combination therapy was conducted by DOX-loaded g-C_3N_4@ZIF-8 NPs, generating singlet oxygen for PDT and delivering DOX with a pH-sensitive manner for chemotherapy. Blue fluorescence of g-C_3N_4 nanosheets and red fluorescence of DOX rendered nanotheranostic property to the particles due to the combined imaging-guided chemo/phototherapy of cancer cells.

It is important to consider that sufficient interaction between ZIF-8 and drugs is essential to achieve high drug encapsulation through ship-in-bottle approaches, i.e., concurrent drug loading and ZIF construction. However, only drugs containing polar functional groups (PFG), e.g. carboxylic acid, carbonyl, and sulfonic groups, have shown satisfactory results in the loading step. Therefore, drug molecules without these functional groups need to be functionalized with appropriate PFGs to reach acceptable drug loading. Zhang et al.[187] developed a versatile prodrug strategy, using cytarabine as a model drug that had insufficient loading in ZIF-8, and was covalently attached with new indocyanine green (IR820), containing sulfonic groups to produce a prodrug via an amide linkage. Sulfonic groups of prodrugs coordinated with the zinc ions in ZIF-8-IR820, strengthening the interaction of prodrug with ZIF-8, thereby resulting in a high drug loading content of 39.8%. Importantly, due to light to heat conversion capability and fluorescence emission capability of IR820, the developed DDS, after functionalizing with HA as targeting ligand, was successfully applied in fluorescence imaging-guided CPTT in vitro breast cancer.

Although single-modality therapies, i.e., chemotherapy, PTT, or PDT, have attracted much attention in cancer therapy, each modality has its own disadvantages, which force the usage of multi-therapies to induce a synergistic effect.[1] The combination of chemotherapy, PDT, PTT, and immunotherapy by ZIF-8 as a nanomedicine platform was developed by Yang et al.[24] (**Figure 14**). DOX, CuS NPs, and protoporphyrin IX (PpIX) used as chemotherapy, PTT, and PDT agent, respectively, were loaded within ZIF-8. The CuS NPs not only served as PTT agent to convert light (808 nm) to heat, but also accelerated DOX release under NIR irradiation. The resulting DOX-CuS-PpIX@ZIF-8 was coated by unmethylated cytosine phosphate-guanine (CpG) oligonucleotide as immune adjuvant through electrostatic interaction for immunotherapy with the aim of preventing cancer metastasis/recurrence. To realize MR imaging, MnO_2 nanosheets were grown on the CpG coated NPs after surface modification of the NPs by the PDA layer. The PDA acted as a gatekeeper to prevent the drug leakage before reaching to cancer sites and enhanced the PTT effect. Therefore, an "all-in-one" nanotheranostic was successfully utilized for MRI-guided chemo/photothermal/photodynamic/immunotherapy of cancer with anti-metastasis/recurrence property. This example clearly demonstrated how the interior and exterior surfaces of ZIF-8 can truly be exploited to construct multifunctional nanocomposites intended for concurrent diagnosis and multi-modal therapy.

One of the main advantages of multifunctional NPs is multimodal imaging, enabling them to combine two or more imaging modalities for simultaneous imaging and therapy. As each imaging modality has its own intrinsic limitations, therefore

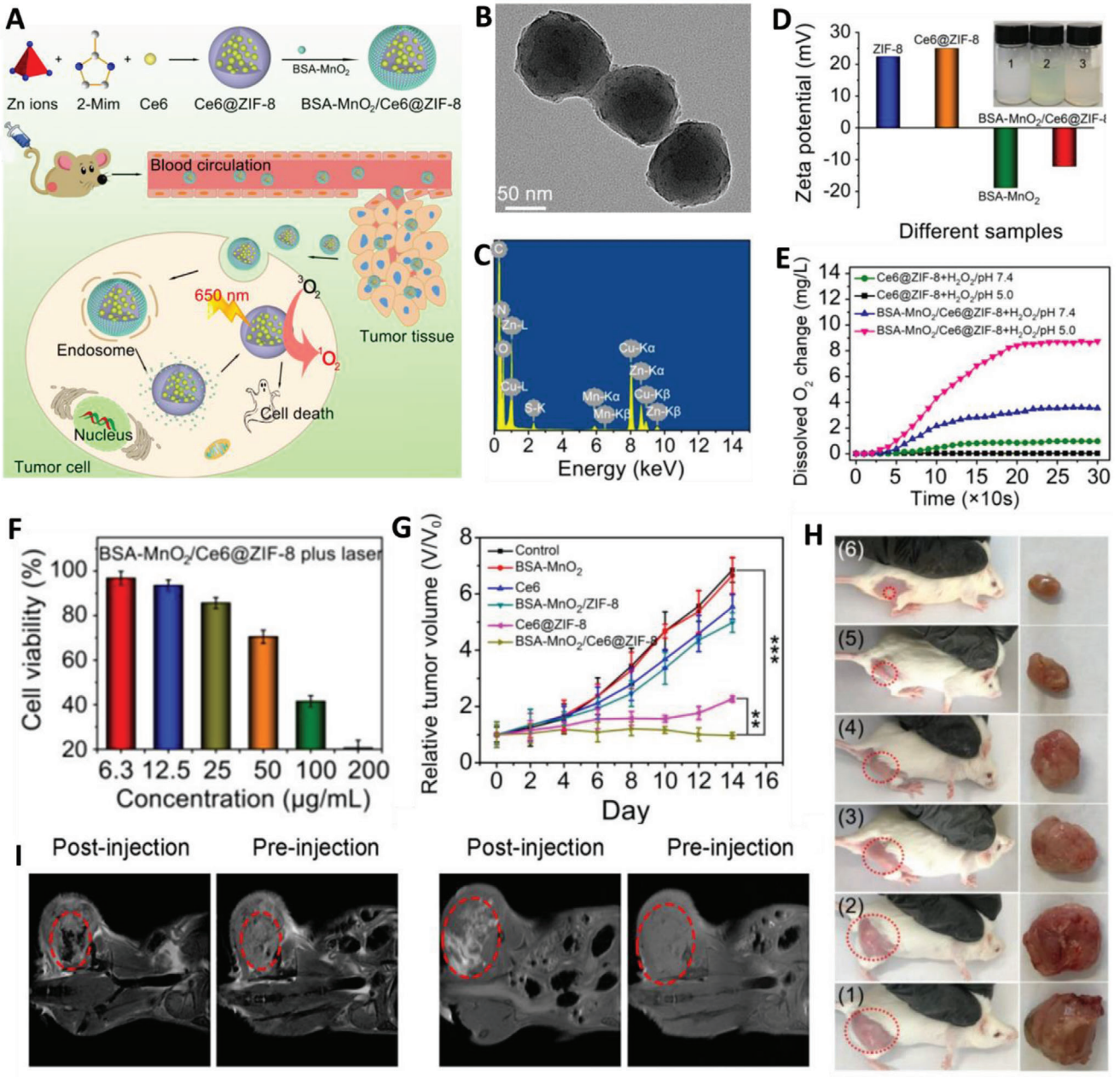

Figure 13. A) Schematic illustration of BSA-MnO_2/Ce6@ZIF-8 synthesis and nanoenzyme-like behavior of the nanosystem upon irradiation with 650 nm NIR laser intended for MRI-guided PDT of cancer. B) TEM and C) EDS images of BSA-MnO_2/Ce6@ZIF-8 NPs. D) Zeta-potential measurements of ZIF-8, Ce6@ZIF-8, BSA-MnO_2, and BSA-MnO_2/Ce6@ZIF-8. Insets are the corresponding photographic images of bare ZIF-8 NPs 1), Ce6@ZIF-8 NPs 2), and BSA-MnO_2/Ce6@ZIF-8 NPs 3). E) Oxygen generation by the Ce6@ZIF-8 NPs and BSA-MnO_2/Ce6@ZIF-8 NPs in the presence of H_2O_2 at different pH values of 7.4 and 5. F) Viability of HeLa cells after incubation with different concentration of BSA-MnO_2/Ce6@ZIF-8 under 650 nm laser irradiation. G) Time-dependent tumor growth curves in tumor-bearing mice treated differently. H) The representative photographic images of tumor tissue in tumor-bearing mice after the different treatments. I) In vivo T1- and T2-weighted MRI before and after injection with the BSA-MnO_2/Ce6@ZIF-8 nanoplatform. Reproduced with permission.[276] Copyright 2019, American Chemical Society.

the integration of several imaging agents within a single system may allow more accurate diagnosis of diseases through.[1] For the first time, the intrinsic two-photon fluorescence imaging property of ZIF-8 NPs derived from 2-MeIm was reported by Zhao et al.[182] Such an intrinsic property holds great potential for the fabrication of novel theranostic platforms. Inspired by the excellent advantages of ZIF-8 in the constriction of multifunctional NPs, Bian et al.[23] prepared an "all-in-one" imaging system, i.e., Fe_3O_4@PAA/AuNCs/ZIF-8, integrating trimodal imaging of MRI, CT, and optical imaging (OI), where Fe_3O_4 and AuNCs acted as MRI and CT/OI agents, respectively. To prepare the nanocomposite, oleic acid (OA) capped Fe_3O_4

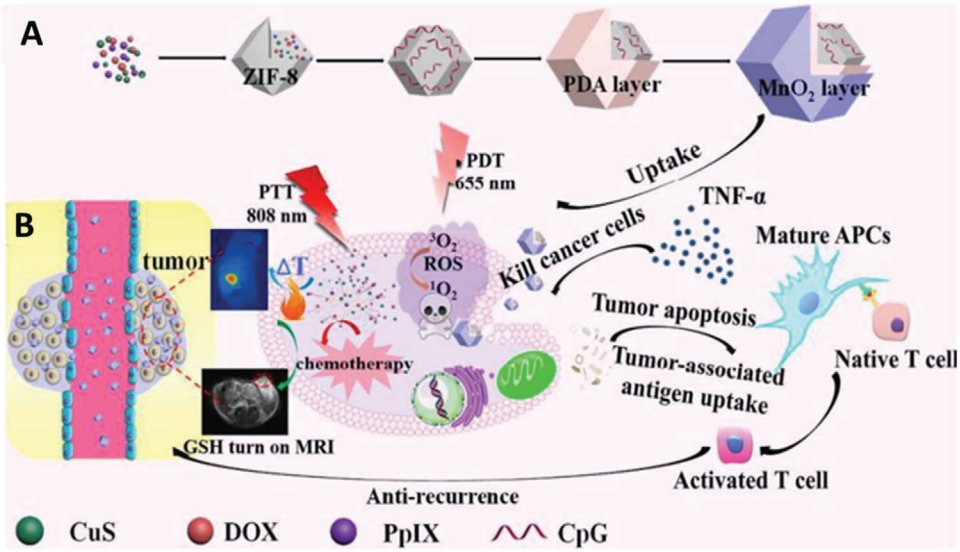

Figure 14. A) Schematic depiction of preparing "all-in-one" nanocomposite of DOX-CuS-PpIX@ZIF-8-PDA-MnO_2. B) Theranostic property of the nanocomposite for MRI-guided chemo/photothermal/photodynamic/immunotherapy to eliminate the primary solid tumor. Reproduced with permission.[24] Copyright 2018, The Royal Society of Chemistry.

NPs were firstly modified by CTAB surfactant. After the coating of the CTAB-functionalized NPs by PAA molecules, the Fe_3O_4@PAA core–shell NPs were obtained. Subsequently, the resultant Fe_3O_4@PAA NPs were incorporated by glutathione capped AuNCs to form Fe_3O_4@PAA/AuNC NPs. Finally, the Fe_3O_4@PAA/AuNCs/ZIF-8 nanocomposite was prepared by the addition of Zn^{2+} and 2-MeIm. The nanocomposite showed ultrahigh DOX loading (1.54 mg DOX per 1 mg of NPs) and high magnetic property. In addition, the NPs showed low systematic toxicity in vivo and suppressed the tumor growth effectively by DOX delivery into the tumor tissue of Balb/c mice through intravenous injection. DOX-loaded Fe_3O_4@carbon@ZIF-8 multifunctional nanotheranostics were also fabricated by He et al.[202] for pH-triggered release of DOX in vitro. The superparamagnetic iron oxide nanocrystals and carbon dots acted as MR and fluorescence imaging contrast agents, respectively. In addition, the remarkable inhibition of tumor growth without side effects was obtained in vivo in the A549 lung cancer mice model after intravenous injection.

As mentioned in the previous sections, one of the main obstacles of cancer CDT is the insufficient concentration of H_2O_2 in TME, leading to the poor performance of this technique.[221] Artificial in situ generation of H_2O_2 in TME, for example, through the conversion of β-D-glucose to gluconic acid and H_2O_2 by GOx, is a reliable way to overcome the shortcomings of CDT.[221] In 2018, Zhang et al.[277] developed an ATP-responsive autocatalytic Fenton nanosystem, called GOx@ZIF@MPN, by the incorporating of GOx in ZIF-8, and then, coating the whole system with Fe(III)/TA polyphenol network (MPN) for suppressing tumor growth mediated by enhanced chemodynamic-starvation therapy (**Figure 15**A,B). As a result of the ATP upregulation in tumor cells, as compared to normal cells, and potential degradation of Fe(III)/TA MPNs in overproduced ATP environments, the MPN shell of the designated nanosystem was degraded into Fe(III) and TA in tumor cells while the internal GOx was exposed. Afterwards, GOx was reacted with the endogenous glucose to generate sufficient H_2O_2 for CDT, while TA as reducing agent converted Fe(III) to Fe(II) to further push forward the Fenton reaction to generate highly toxic hydroxyl radical ($^{\bullet}OH$) by Fe(II) as a catalyst. It should be noted that TA played a crucial role in accelerating Fe(III)/Fe(II) conversion to guarantee highly efficient Fenton reaction mediated CDT. ATP-responsive degradation of GOx@ZIF@MPN was shown by the release of iron at different ATP concentrations (Figure 15C). The iron release was increased when ATP concentration and treating time increased, demonstrating the ATP-responsive property of the nanosystem, due to the strong binding affinity of ATP to Fe(III). After intravenous injection of Cy5.5-loaded GOx@ZIF@MPN NPs to 4T1 tumor-bearing mice, the fluorescence intensity was gradually enhanced over time and then weakened, but still retained in a desirable level after 24 h, confirming long time blood circulation of the NPs (Figure 15D). In addition, the MRI signal was detected after 10 min of the post-injection due to the T1-weighted contrast effect of GOx@ZIF@MPN after intratumoral injection. The MRI signal was gradually enhanced over time till 30 min, demonstrating rapid degradation of the MPN shell in response to ATP at the tumor site and generation of excellent T1-weighted imaging signal for tumor diagnosis (Figure 15E). As shown in Figure 15F,G, studies on 4T1 cells treated with GOx@ZIF@MPN showed that the nanosystem had very high toxicity against the cancer cells both in vitro and in vivo, when compared to control groups of GOx@ZIF and ZIF@MPN, confirming a synergistic effect of CDT and starvation therapy on the cancer ablation. Such an enhanced therapeutic effect was also observed by the photographic imaging of harvested tumors from each treatment group after sacrificing mice (Figure 15G). Very recently, a biomimetic cascade nanoreactor based on ZIFs, i.e., DOX-loaded GOx@ZIF camouflaged by the tumor cell membrane, was also developed for synergistic chemotherapy and starvation therapy.[125] Indeed, the biomimetic membrane endowed the NPs with superior immune

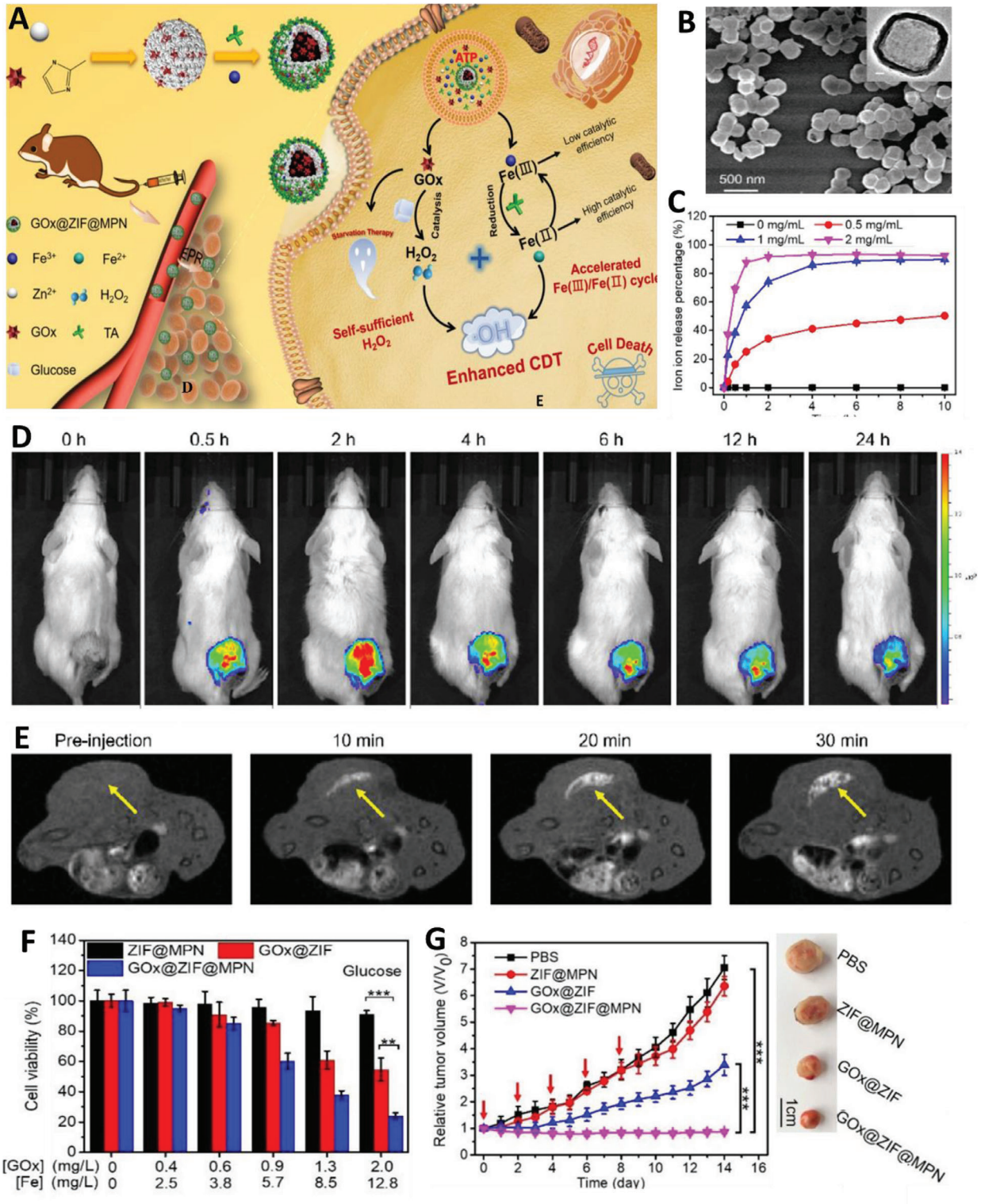

Figure 15. A) Schematic representation of GOx@ZIF@MPN synthesis as an ATP-responsive nanotheranostic for Fenton reaction mediated CDT and detailed description of glucose consumption, H_2O_2 generation and Fe(III) to Fe(II) conversion processes. B) The TEM image of GOx@ZIF@MPN NPs. C) Fe(III) release from GOx@ZIF@MPN at different ATP concentration levels. D) In vivo fluorescence images of tumor-bearing mice after intravenous injection of Cy5.5-doped GOx@ZIF@MPN NPs at various times. E) T1-weighted MRI images after intratumoral injection of GOx@ZIF@MPN NPs at various times. F) In vitro viability of 4T1 cells after incubating with different samples in the presence of glucose. G) Tumor volume growth curve of mice in different groups and photographic images of 4T1 tumor tissues in different groups after 14 days of treatment. Reproduced with permission.[277] Copyright 2018, American Chemical Society.

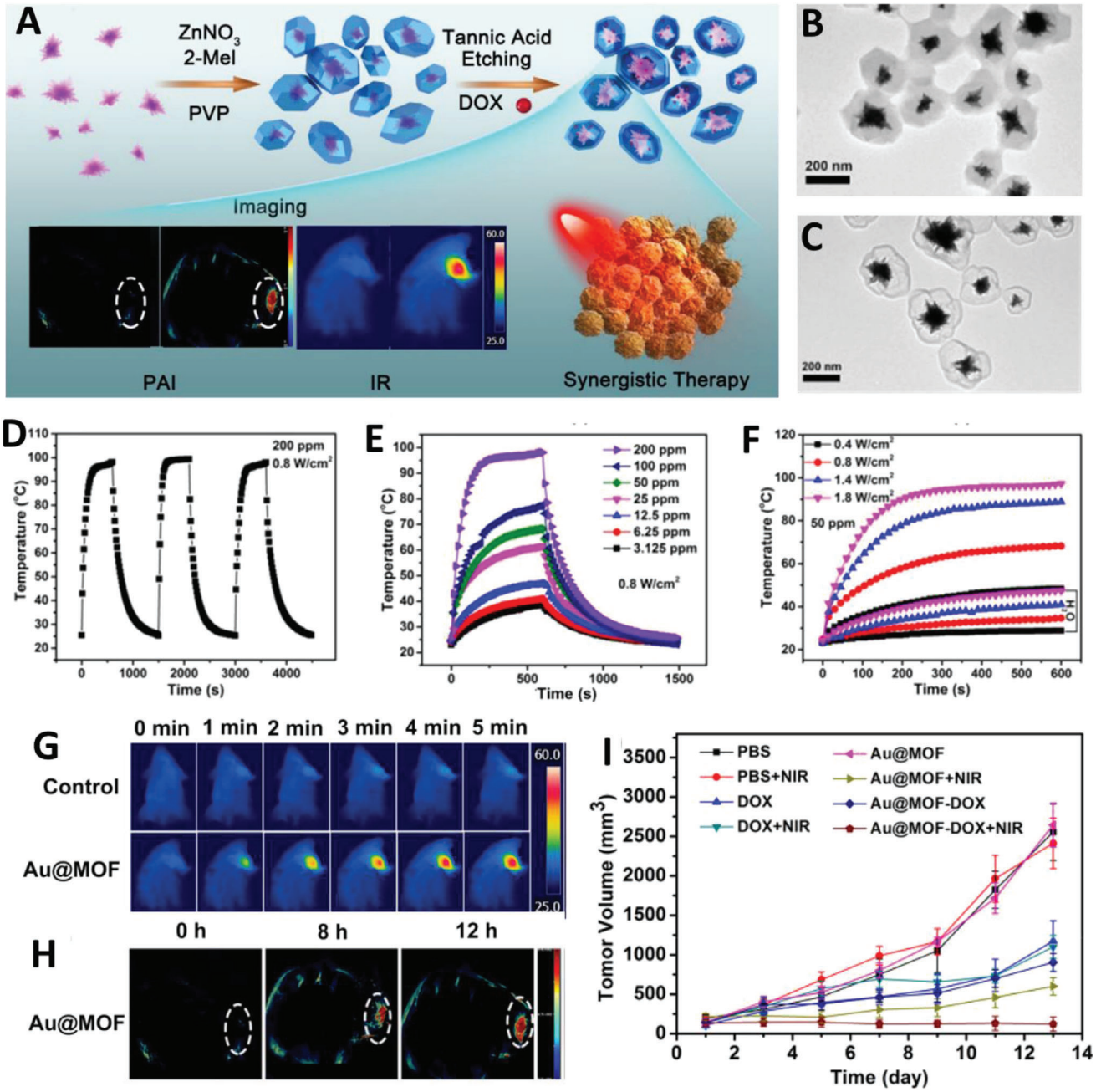

Figure 16. A) Schematic illustration of the Au@MOF-DOX synthesis and its imaging and synergistic anticancer property. B) TEM images Au@MOF and C) yolk-shell structural Au@MOF. D) The heating and cooling curves of Au@MOF (200 ppm of Au) irradiated at 1064 nm NIR laser. E) Temperature change profile of Au@MOF with different concentrations of Au and F) the profile at various power densities for 10 min with 50 ppm of Au concentration exposed to 1064 nm NIR laser. G) In vivo ITI images of H22 tumor-bearing mice. The mice were intravenously injected with PBS or Au@MOF NPs irradiated with 0.8 W cm^{-2} 1064 nm laser for 5 min. H) In vivo PAI images of Balb/c nude mice. The mice were intravenously injected with Au@MOF NPs. I) Time-dependent tumor growth curves of tumor-bearing mice in different groups. Reproduced with permission.[282] Copyright 2019, American Chemical Society.

evasion and homologous targeting capacities, thereby introducing a novel and efficient method for precise tumor therapy.

Yolk–shell nanocomposites (YSCs), integrating different compositions and functionalities in a single system have attracted wide attention in biological research.[278,279] In fact, the hollow cavity of the YSCs can act as a container for loading more cargos and the shell can serve as a protective layer for the yolk, which can be made of a wide variety of NPs.[280,281] Recently, an interesting multifunctional YSC was constructed by integrating star-shaped gold (Au star) NPs and ZIF-8 as the shell[282] (**Figure 16**A). As a result of the acid-degradability of ZIF-8 NPs, the part of the ZIF-shell was selectively removed by TA as an etchant

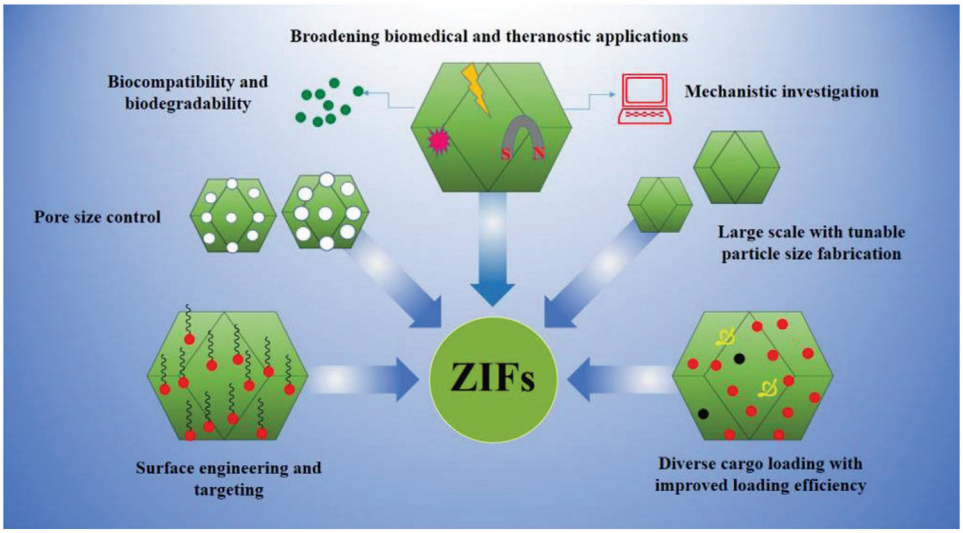

Scheme 2. Schematic illustration of the facing challenges and future progresses of ZIF-based nanostructures for biomedical applications.

to obtain the yolk-shell structures (Au@MOF) (Figure 16B,C). The yolk-shell Au@MOF nanocomposite not only worked as a photothermal agent at NIR-I (750–1000 nm), but also showed very high photothermal transformation efficiency at NIR-II region (1000–1700 nm; Figure 16D–F), which is of particular importance in deeper tissue penetration and higher spatiotemporal resolution than NIR-I region. Moreover, due to the strong NIR light absorbance of the Au yolk, the nanosystem was able to be used for ITI and PAI of cancer tissue (Figure 16G,H). After DOX encapsulation and upon the laser irradiation at NIR-II window (1064 nm), the Au@MOF exhibited outstanding synergistic tumor ablation effect based on the light to heat conversion property of the Au yolks and anti-cancer property of DOX (Figure 16I), which caused a remarkable synergistic anticancer effect through combined chemo-phototherapy.

5. Conclusions

Recently, the scientific community has witnessed the considerable achievements of ZIFs for versatile biomedical applications, especially in the stimuli-responsive DDSs and biomineralization of elegant bio-macromolecules due to their unique features, including tunable pore size, large surface area, high thermal stability, and favorable biodegradability/biocompatibility. Herein, we have comprehensively discussed the very recent developments for the controlling of the physicochemical properties of ZIFs and their impact on diverse cargo loading and the release trend of various molecules, including drugs, bio-macromolecules, photosensitizers, and photothermal agents, in order to produce optimized DDSs for the treatment of different diseases, such as cancer and infection. Although the study of biomedical applications of ZIFs is in its infancy phase, it has opened promising and intriguing prospects based on their high performance in many applications, which was discussed in this review paper (Tables 1 and 2). However, despite the growing interest and impressive advancements in this field, some critical issues and foreseeable challenges are crucial to be considered and addressed for the rational design of ZIF-based nanosystems for versatile biomedical applications (**Scheme 2**). First, broadening the biomedical applications of ZIFs and improving the therapeutic efficacy of its derived nanomedicines should be further investigated. The intrinsic characteristics of ZIFs endow them with superior capability in the loading of different cargos in a single particle to exploit them as multifunctional carriers. For example, in the case of cancer therapy or bacterial infection, efficient boosting of the therapeutic efficacy might be achieved by the integration of immunotherapeutic and starvation agents with chemo and phototherapeutic cargos to increase the efficacy of the ZIF nanosystems. While the current advancements on the of the ZIFs have focused on the abovementioned diseases, other biomedical applications, including biosensing, brain disease therapy, tissue engineering, inflammation alleviation, etc., are yet to be investigated. In addition, the synthesis of other novel and multifunctional derivatives of ZIF NPs rather than ZIF-8 might expand the applications of the porous ZIF-based nanomaterials in nanomedicine. In this context, the physicochemical properties of ZIFs, including particle size, pore size, surface modification/targeting, compositional and morphological features must be carefully tuned to meet standard requirements for in vivo studies.

The second issue is related to the large scale preparation of ZIFs with adjustable particle diameter and pore size and the exploration of new targeting ligands for surface modification of the ZIFs. This issue can affect the drug loading into the ZIFs, alter drug accumulation at a specific site, and markedly reduce/increase the uptake of the NPs by RES organs. At present, ZIFs are mainly prepared in a lab-scale and researchers must work on the development of synthesis approaches for the rapid and reproducible production of these nanomaterials in a large scale. Since the toxicity and poor loading are the main concerns for the bench to bedside movement, preparation of HZIFs can be suggested as an alternative to enhance the drug loading efficiency and reduce the frequency of administration, thus overcoming the toxicity concerns of ZIF carriers.

At present, due to the novelty of ZIFs and limited understanding of their biological effects, most of the research is towards

developing "proof-of-concept" studies that are not clinically relevant. For future clinical translation, short and long-term biosafety on different organs, biodegradability, biodistribution, blood half-life, and clearance of the ZIFs must be studied comprehensively. Such studies should be conducted not only in small animals, such as rabbit and mouse, but also in big animals, including pigs and dogs to produce clinically applicable ZIF-based nanoscale formulations. To this end, we do believe that the physicochemical properties of ZIFs are essential factors that should be optimized to push forward these nanosystems for clinical application. Moreover, since the interaction of ZIFs with the immune system has remained largely unknown, the influence of these NPs with immune cells should be clarified before developing new techniques for their large scale production.

Taken all together, the engineering of ZIFs for biomedical applications is still in an infancy stage and there are plenty of opportunities to design and fabricate advanced DDSs in this burgeoning field of nanomedicine. To achieve this goal, closer and strengthened collaboration among experts from diverse fields will highly be imperative if we expect novel clinical innovations and personalized medicine in the near future through revealed therapeutic and diagnostic mechanisms of ZIF-based "magic bullet."

Acknowledgements

A.M. acknowledges the financial support from the Zanjan University of Medical Sciences (Grant no. A-12-968-2). M.-A.S. acknowledges the financial support from the Academy of Finland (Grant no. 317316). H.A.S. acknowledges the financial support from the HiLIFE Research Funds, the Sigrid Jusélius Foundation, and the Academy of Finland (Grant no. 317042).

Conflict of Interest

The authors declare no conflict of interest.

Keywords

antibacterial therapies, biomineralization, cancer therapies, metal-organic frameworks, ZIF nanoparticles

Received: February 14, 2020
Revised: March 25, 2020
Published online: May 7, 2020

[1] D.-E. Lee, H. Koo, I.-C. Sun, J. H. Ryu, K. Kim, I. C. Kwon, *Chem. Soc. Rev.* **2012**, *41*, 2656.
[2] W. Cai, J. Wang, C. Chu, W. Chen, C. Wu, G. Liu, *Adv. Sci.* **2019**, *6*, 1801526.
[3] J. Zhou, G. Tian, L. Zeng, X. Song, X. Bian, *Adv. Healthcare Mater. 7*, **2018**, 1800022.
[4] K. Lu, T. Aung, N. Guo, R. Weichselbaum, W. Lin, *Adv. Mater.* **2018**, *30*, 1707634.
[5] K. S. Park, Z. Ni, A. P. Côté, J. Y. Choi, R. Huang, F. J. Uribe-Romo, H. K. Chae, M. O'Keeffe, O. M. Yaghi, *Proc. Natl. Acad. Sci. USA* **2006**, *103*, 10186.
[6] R. Banerjee, H. Furukawa, D. Britt, C. Knobler, M. O'Keeffe, O. M. Yaghi, *J. Am. Chem. Soc.* **2009**, *131*, 3875.
[7] Y. Li, F. Liang, H. Bux, A. Feldhoff, W. Yang, J. Caro, *Angew. Chem., Int. Ed.* **2010**, *49*, 548.
[8] G. Lu, J. T. Hupp, *J. Am. Chem. Soc.* **2010**, *132*, 7832.
[9] C.-Y. Sun, C. Qin, X.-L. Wang, G.-S. Yang, K.-Z. Shao, Y.-Q. Lan, Z.-M. Su, P. Huang, C.-G. Wang, E.-B. Wang, *Dalton Trans.* **2012**, *41*, 6906.
[10] C. Chizallet, S. Lazare, D. Bazer-Bachi, F. Bonnier, V. Lecocq, E. Soyer, A.-A. Quoineaud, N. Bats, *J. Am. Chem. Soc.* **2010**, *132*, 12365.
[11] Y. V. Kaneti, S. Dutta, M. S. Hossain, M. J. Shiddiky, K. Tung, F. Shieh, C. Tsung, K. C. Wu, Y. Yamauchi, *Adv. Mater.* **2017**, *29*, 1700213.
[12] J. Cravillon, S. Münzer, S.-J. Lohmeier, A. Feldhoff, K. Huber, M. Wiebcke, *Chem. Mater.* **2009**, *21*, 1410.
[13] Y. Pan, Y. Liu, G. Zeng, L. Zhao, Z. Lai, *Chem. Commun.* **2011**, *47*, 2071.
[14] J. Yang, Y.-B. Zhang, Q. Liu, C. A. Trickett, E. Gutiérrez-Puebla, M. Á. Monge, H. Cong, A. Aldossary, H. Deng, O. M. Yaghi, *J. Am. Chem. Soc.* **2017**, *139*, 6448.
[15] O. Karagiaridi, M. B. Lalonde, W. Bury, A. A. Sarjeant, O. K. Farha, J. T. Hupp, *J. Am. Chem. Soc.* **2012**, *134*, 18790.
[16] J. Yao, M. He, H. Wang, *CrystEngComm* **2015**, *17*, 4970.
[17] W. Cai, J. Wang, C. Chu, W. Chen, C. Wu, G. Liu, *Adv. Sci.* **2019**, *6*, 1801526.
[18] J. Zhuang, C.-H. Kuo, L.-Y. Chou, D.-Y. Liu, E. Weerapana, C.-K. Tsung, *ACS Nano* **2014**, *8*, 2812.
[19] M. Zheng, S. Liu, X. Guan, Z. Xie, *ACS Appl. Mater. Interfaces* **2015**, *7*, 22181.
[20] C. Adhikari, A. Das, A. Chakraborty, *Mol. Pharmaceutics* **2015**, *12*, 3158.
[21] L. Gao, Q. Chen, T. Gong, J. Liu, C. Li, *Nanoscale* **2019**, *11*, 21030.
[22] Q. Wu, M. Niu, X. Chen, L. Tan, C. Fu, X. Ren, J. Ren, L. Li, K. Xu, H. Zhong, *Biomaterials* **2018**, *162*, 132.
[23] R. Bian, T. Wang, L. Zhang, L. Li, C. Wang, *Biomater. Sci.* **2015**, *3*, 1270.
[24] J.-C. Yang, Y. Shang, Y.-H. Li, Y. Cui, X.-B. Yin, *Chem. Sci.* **2018**, *9*, 7210.
[25] L. Zhang, S. Wan, C. Li, L. Xu, H. Cheng, X. Zhang, *Nano Lett.* **2018**, *18*, 7609.
[26] Z. Song, Y. Wu, Q. Cao, H. Wang, X. Wang, H. Han, *Adv. Funct. Mater.* **2018**, *28*, 1800011.
[27] Y.-F. Guo, W.-J. Fang, J.-R. Fu, Y. Wu, J. Zheng, G.-Q. Gao, C. Chen, R.-W. Yan, S.-G. Huang, C.-C. Wang, *Appl. Surf. Sci.* **2018**, *435*, 149.
[28] A. Malik, M. Nath, S. Mohiyuddin, G. Packirisamy, *ACS Omega* **2018**, *3*, 8288.
[29] H. Shen, J. Liu, J. Lei, H. Ju, *Chem. Commun.* **2018**, *54*, 9155.
[30] C. Carrillo-Carrión, R. Martínez, M. F. Navarro Poupard, B. Pelaz, E. Polo, A. Arenas-Vivo, A. Olgiati, P. Taboada, M. G. Soliman, Ú. Catalán, *Angew. Chem., Int. Ed.* **2019**, *58*, 7078.
[31] J. Lin, P. Xin, L. An, Y. Xu, C. Tao, Q. Tian, Z. Zhou, B. Hu, S. Yang, *Chem. Commun.* **2019**, *55*, 478.
[32] K. Dong, Z. Wang, Y. Zhang, J. Ren, X. Qu, *ACS Appl. Mater. Interfaces* **2018**, *10*, 31998.
[33] H. Zhang, W. Jiang, R. Liu, J. Zhang, D. Zhang, Z. Li, Y. Luan, *ACS Appl. Mater. Interfaces* **2017**, *9*, 19687.
[34] L. Yan, X. Chen, Z. Wang, X. Zhang, X. Zhu, M. Zhou, W. Chen, L. Huang, V. A. Roy, P. K. Yu, *ACS Appl. Mater. Interfaces* **2017**, *9*, 32990.
[35] Q.-S. Pan, T.-T. Chen, C.-P. Nie, J.-T. Yi, C. Liu, Y.-L. Hu, X. Chu, *ACS Appl. Mater. Interfaces* **2018**, *10*, 33070.
[36] X. Yang, L. Li, D. He, L. Hai, J. Tang, H. Li, X. He, K. Wang, *J. Mater. Chem. B* **2017**, *5*, 4648.
[37] H. Ren, L. Zhang, J. An, T. Wang, L. Li, X. Si, L. He, X. Wu, C. Wang, Z. Su, *Chem. Commun.* **2014**, *50*, 1000.
[38] G. Lu, S. Li, Z. Guo, O. K. Farha, B. G. Hauser, X. Qi, Y. Wang, X. Wang, S. Han, X. Liu, *Nat. Chem.* **2012**, *4*, 310.
[39] W.-H. Chen, G.-F. Luo, M. Vázquez-González, R. Cazelles, Y. S. Sohn, R. Nechushtai, Y. Mandel, I. Willner, *ACS Nano* **2018**, *12*, 7538.

[40] S. K. Alsaiari, S. Patil, M. Alyami, K. O. Alamoudi, F. A. Aleisa, J. S. Merzaban, M. Li, N. M. Khashab, *J. Am. Chem. Soc.* **2018**, *140*, 143.
[41] X. Lian, Y. Fang, E. Joseph, Q. Wang, J. Li, S. Banerjee, C. Lollar, X. Wang, H.-C. Zhou, *Chem. Soc. Rev.* **2017**, *46*, 3386.
[42] P. Horcajada, R. Gref, T. Baati, P. K. Allan, G. Maurin, P. Couvreur, G. Ferey, R. E. Morris, C. Serre, *Chem. Rev.* **2012**, *112*, 1232.
[43] G. Wyszogrodzka, B. Marszałek, B. Gil, P. Dorożyński, *Drug Discovery Today* **2016**, *21*, 1009.
[44] C. He, D. Liu, W. Lin, *Chem. Rev.* **2015**, *115*, 11079.
[45] J. Della Rocca, D. Liu, W. Lin, *Acc. Chem. Res.* **2011**, *44*, 957.
[46] W. Chen, C. Wu, *Dalton Trans.* **2018**, *47*, 2114.
[47] S. Rojas, A. Arenas-Vivo, P. Horcajada, *Coord. Chem. Rev.* **2019**, *388*, 202.
[48] J. Troyano, A. Carné-Sánchez, C. Avci, I. Imaz, D. Maspoch, *Chem. Soc. Rev.* **2019**, *48*, 5534.
[49] R. Wu, T. Fan, J. Chen, Y. Li, *ACS Sustainable Chem. Eng.* **2019**, *7*, 3632.
[50] B. Chen, Z. Yang, Y. Zhu, Y. Xia, *J. Mater. Chem. A* **2014**, *2*, 16811.
[51] M. Eddaoudi, D. F. Sava, J. F. Eubank, K. Adil, V. Guillerm, *Chem. Soc. Rev.* **2015**, *44*, 228.
[52] R. Banerjee, A. Phan, B. Wang, C. Knobler, H. Furukawa, M. O'keeffe, O. M. Yaghi, *Science* **2008**, *319*, 939.
[53] F. Shieh, S. Wang, S. Leo, K. C. Wu, *Chem. - Eur. J.* **2013**, *19*, 11139.
[54] H.-Y. Cho, J. Kim, S.-N. Kim, W.-S. Ahn, *Microporous Mesoporous Mater.* **2013**, *169*, 180.
[55] D. Yamamoto, T. Maki, S. Watanabe, H. Tanaka, M. T. Miyahara, K. Mae, *Chem. Eng. J.* **2013**, *227*, 145.
[56] Y.-R. Lee, M.-S. Jang, H.-Y. Cho, H.-J. Kwon, S. Kim, W.-S. Ahn, *Chem. Eng. J.* **2015**, *271*, 276.
[57] S. Tanaka, K. Kida, T. Nagaoka, T. Ota, Y. Miyake, *Chem. Commun.* **2013**, *49*, 7884.
[58] H. N. Abdelhamid, Z. Huang, A. M. El-Zohry, H. Zheng, X. Zou, *Inorg. Chem.* **2017**, *56*, 9139.
[59] W. Morris, C. J. Doonan, H. Furukawa, R. Banerjee, O. M. Yaghi, *J. Am. Chem. Soc.* **2008**, *130*, 12626.
[60] Y. Li, J. Jin, D. Wang, J. Lv, K. Hou, Y. Liu, C. Chen, Z. Tang, *Nano Res.* **2018**, *11*, 3294.
[61] L. He, T. Wang, J. An, X. Li, L. Zhang, L. Li, G. Li, X. Wu, Z. Su, C. Wang, *CrystEngComm* **2014**, *16*, 3259.
[62] S.-Z. Ren, D. Zhu, X.-H. Zhu, B. Wang, Y.-S. Yang, W.-X. Sun, X.-M. Wang, P.-C. Lv, Z.-C. Wang, H.-L. Zhu, *ACS Appl. Mater. Interfaces* **2019**, *11*, 20678.
[63] Z. Mo, H. Zhou, D. Zhou, R. Lin, P. Liao, C. He, W. Zhang, X. Chen, J. Zhang, *Adv. Mater.* **2018**, *30*, 1704350.
[64] L. Song, J. Zhang, L. Sun, F. Xu, F. Li, H. Zhang, X. Si, C. Jiao, Z. Li, S. Liu, *Energy Environ. Sci.* **2012**, *5*, 7508.
[65] S. Cao, G. Gody, W. Zhao, S. Perrier, X. Peng, C. Ducati, D. Zhao, A. K. Cheetham, *Chem. Sci.* **2013**, *4*, 3573.
[66] Y. Yang, F. Wang, Q. Yang, Y. Hu, H. Yan, Y.-Z. Chen, H. Liu, G. Zhang, J. Lu, H.-L. Jiang, *ACS Appl. Mater. Interfaces* **2014**, *6*, 18163.
[67] W. Zhang, Y. Liu, G. Lu, Y. Wang, S. Li, C. Cui, J. Wu, Z. Xu, D. Tian, W. Huang, *Adv. Mater.* **2015**, *27*, 2923.
[68] Y. Wu, M. Zhou, B. Zhang, B. Wu, J. Li, J. Qiao, X. Guan, F. Li, *Nanoscale* **2014**, *6*, 1105.
[69] Y. Hu, X. Xu, B. Zheng, S. Hou, P. Wang, W. Chen, C. Gao, Z. Gu, Y. Shen, J. Wu, *Small Methods 3*, **2019**, 1800547.
[70] S. Li, K. Wang, Y. Shi, Y. Cui, B. Chen, B. He, W. Dai, H. Zhang, X. Wang, C. Zhong, *Adv. Funct. Mater.* **2016**, *26*, 2715.
[71] W. Xia, J. Zhu, W. Guo, L. An, D. Xia, R. Zou, *J. Mater. Chem. A* **2014**, *2*, 11606.
[72] A. Schejn, L. Balan, V. Falk, L. Aranda, G. Medjahdi, R. Schneider, *CrystEngComm* **2014**, *16*, 4493.
[73] X. Guo, T. Xing, Y. Lou, J. Chen, *J. Solid State Chem.* **2016**, *235*, 107.
[74] N. L. Torad, M. Hu, Y. Kamachi, K. Takai, M. Imura, M. Naito, Y. Yamauchi, *Chem. Commun.* **2013**, *49*, 2521.
[75] S. Tanaka, K. Kida, M. Okita, Y. Ito, Y. Miyake, *Chem. Lett.* **2012**, *41*, 1337.
[76] Y. Pan, D. Heryadi, F. Zhou, L. Zhao, G. Lestari, H. Su, Z. Lai, *CrystEngComm* **2011**, *13*, 6937.
[77] Q. Shi, Z. Song, X. Kang, J. Dong, Y. Zhang, *CrystEngComm* **2012**, *14*, 8280.
[78] R. Chen, J. Yao, Q. Gu, S. Smeets, C. Baerlocher, H. Gu, D. Zhu, W. Morris, O. M. Yaghi, H. Wang, *Chem. Commun.* **2013**, *49*, 9500.
[79] M. Jian, B. Liu, R. Liu, J. Qu, H. Wang, X. Zhang, *RSC Adv.* **2015**, *5*, 48433.
[80] Y. Chen, S. Tang, *J. Solid State Chem.* **2019**, *276*, 68.
[81] R. Wu, X. Qian, X. Rui, H. Liu, B. Yadian, K. Zhou, J. Wei, Q. Yan, X. Feng, Y. Long, *Small* **2014**, *10*, 1932.
[82] H. Yu, X. Qiu, P. Neelakanda, L. Deng, N. M. Khashab, S. P. Nunes, K.-V. Peinemann, *Sci. Rep.* **2015**, *5*, 15275.
[83] H. Hu, B. Y. Guan, X. W. D. Lou, *Chem* **2016**, *1*, 102.
[84] D. Liu, J. Wan, G. Pang, Z. Tang, *Adv. Mater.* **2018**, *31*, 1803291.
[85] H. J. Lee, W. Cho, M. Oh, *Chem. Commun.* **2012**, *48*, 221.
[86] S. Wang, Y. Fan, J. Teng, Y. Fan, J. Jiang, H. Wang, H. Grützmacher, D. Wang, C. Su, *Small* **2016**, *12*, 5702.
[87] C. Li, L. Li, S. Yu, X. Jiao, D. Chen, *Adv. Mater. Technol.* **2016**, *1*, 1600127.
[88] M. Hu, Y. Ju, K. Liang, T. Suma, J. Cui, F. Caruso, *Adv. Funct. Mater.* **2016**, *26*, 5827.
[89] W. Zhang, X. Jiang, Y. Zhao, A. Carné-Sánchez, V. Malgras, J. Kim, J. H. Kim, S. Wang, J. Liu, J.-S. Jiang, *Chem. Sci.* **2017**, *8*, 3538.
[90] A. Carné-Sánchez, I. Imaz, M. Cano-Sarabia, D. Maspoch, *Nat. Chem.* **2013**, *5*, 203.
[91] J. Yang, F. Zhang, H. Lu, X. Hong, H. Jiang, Y. Wu, Y. Li, *Angew. Chem., Int. Ed.* **2015**, *54*, 10889.
[92] J. Liu, Y. Huang, A. Kumar, A. Tan, S. Jin, A. Mozhi, X.-J. Liang, *Biotechnol. Adv.* **2014**, *32*, 693.
[93] D. Schmaljohann, *Adv. Drug Delivery Rev.* **2006**, *58*, 1655.
[94] M. Karimi, A. Ghasemi, P. S. Zangabad, R. Rahighi, S. M. M. Basri, H. Mirshekari, M. Amiri, Z. S. Pishabad, A. Aslani, M. Bozorgomid, *Chem. Soc. Rev.* **2016**, *45*, 1457.
[95] M. Stubbs, P. M. McSheehy, J. R. Griffiths, C. L. Bashford, *Mol. Med. Today* **2000**, *6*, 15.
[96] A. J. Howarth, A. W. Peters, N. A. Vermeulen, T. C. Wang, J. T. Hupp, O. K. Farha, *Chem. Mater.* **2017**, *29*, 26.
[97] J. Zhuang, A. P. Young, C. Tsung, *Small* **2017**, *13*, 1700880.
[98] Y. Wang, J. Yan, N. Wen, H. Xiong, S. Cai, Q. He, Y. Hu, D. Peng, Z. Liu, Y. Liu, *Biomaterials* **2019**, *230*, 119619.
[99] N. Liédana, A. Galve, C. Rubio, C. Téllez, J. Coronas, *ACS Appl. Mater. Interfaces* **2012**, *4*, 5016.
[100] H. Zheng, Y. Zhang, L. Liu, W. Wan, P. Guo, A. M. Nyström, X. Zou, *J. Am. Chem. Soc.* **2016**, *138*, 962.
[101] A. Tiwari, A. Singh, N. Garg, J. K. Randhawa, *Sci. Rep.* **2017**, *7*, 12598.
[102] N. N. Sheno, S. Farhadi, A. Maleki, M. Hamidi, *New J. Chem.* **2019**, *43*, 1956.
[103] H. Kaur, G. C. Mohanta, V. Gupta, D. Kukkar, S. Tyagi, *J. Drug Delivery Sci. Technol.* **2017**, *41*, 106.
[104] H. Zhang, W. Chen, K. Gong, J. Chen, *ACS Appl. Mater. Interfaces* **2017**, *9*, 31519.
[105] Y. Li, Y. Zheng, X. Lai, Y. Chu, Y. Chen, *RSC Adv.* **2018**, *8*, 23623.
[106] Y. Li, N. Xu, W. Zhu, L. Wang, B. Liu, J. Zhang, Z. Xie, W. Liu, *ACS Appl. Mater. Interfaces* **2018**, *10*, 22974.
[107] K. Dong, Y. Zhang, L. Zhang, Z. Wang, J. Ren, X. Qu, *Talanta* **2019**, *194*, 703.
[108] Z. Shi, X. Chen, L. Zhang, S. Ding, X. Wang, Q. Lei, W. Fang, *Biomater. Sci.* **2018**, *6*, 2582.

[109] X. Chen, R. Tong, Z. Shi, B. Yang, H. Liu, S. Ding, X. Wang, Q. Lei, J. Wu, W. Fang, *ACS Appl. Mater. Interfaces* **2018**, *10*, 2328.
[110] X. Chen, Z. Shi, R. Tong, S. Ding, X. Wang, J. Wu, Q. Lei, W. Fang, *ACS Biomater. Sci. Eng.* **2018**, *4*, 4183.
[111] D. F. Sava Gallis, K. S. Butler, J. O. Agola, C. J. Pearce, A. A. McBride, *ACS Appl. Mater. Interfaces* **2019**, *11*, 7782.
[112] N. A. Soomro, Q. Wu, S. A. Amur, H. Liang, A. U. Rahman, Q. Yuan, Y. Wei, *Colloids Surf., B* **2019**, *182*, 110364.
[113] S. Aguado, J. Quirós, J. Canivet, D. Farrusseng, K. Boltes, R. Rosal, *Chemosphere* **2014**, *113*, 188.
[114] A. R. Chowdhuri, B. Das, A. Kumar, S. Tripathy, S. Roy, S. K. Sahu, *Nanotechnology* **2017**, *28*, 095102.
[115] A.-N. Au-Duong, C.-K. Lee, *Mater. Sci. Eng., C* **2017**, *76*, 477.
[116] D. Bagchi, A. Bhattacharya, T. Dutta, S. Nag, D. Wulferding, P. Lemmens, S. K. Pal, *ACS Appl. Bio Mater.* **2019**, *2*, 1772.
[117] B. Wu, J. Fu, Y. Zhou, Y. Shi, J. Wang, X. Feng, Y. Zhao, G. Zhou, C. Lu, G. Quan, *Pharmaceutics* **2019**, *11*, 463.
[118] T. Dutta, D. Bagchi, S. K. Pal, *Biomed. Phys. Eng. Express* **2018**, *4*, 055004.
[119] I. B. Vasconcelos, T. G. da Silva, G. C. Militão, T. A. Soares, N. M. Rodrigues, M. O. Rodrigues, N. B. da Costa, R. O. Freire, S. A. Junior, *RSC Adv.* **2012**, *2*, 9437.
[120] W. Zhu, G. Xiang, J. Shang, J. Guo, B. Motevalli, P. Durfee, J. O. Agola, E. N. Coker, C. J. Brinker, *Adv. Funct. Mater.* **2018**, *28*, 1705274.
[121] C. Tamames-Tabar, D. Cunha, E. Imbuluzqueta, F. Ragon, C. Serre, M. J. Blanco-Prieto, P. Horcajada, *J. Mater. Chem. B* **2014**, *2*, 262.
[122] G. Fan, C. M. Dundas, C. Zhang, N. A. Lynd, B. K. Keitz, *ACS Appl. Mater. Interfaces* **2018**, *10*, 18601.
[123] E. Shearier, P. Cheng, Z. Zhu, J. Bao, Y. H. Hu, F. Zhao, *RSC Adv.* **2016**, *6*, 4128.
[124] T. J. Brunner, P. Wick, P. Manser, P. Spohn, R. N. Grass, L. K. Limbach, A. Bruinink, W. J. Stark, *Environ. Sci. Technol.* **2006**, *40*, 4374.
[125] H. Cheng, X.-Y. Jiang, R.-R. Zheng, S.-J. Zuo, L.-P. Zhao, G.-L. Fan, B.-R. Xie, X.-Y. Yu, S.-Y. Li, X.-Z. Zhang, *Biomaterials* **2019**, *195*, 75.
[126] Z. Jiang, Y. Wang, L. Sun, B. Yuan, Y. Tian, L. Xiang, Y. Li, Y. Li, J. Li, A. Wu, *Biomaterials* **2019**, *197*, 41.
[127] W. Sun, Z. Gu, *Expert Opin. Drug Delivery* **2016**, *13*, 311.
[128] R. Mo, T. Jiang, R. DiSanto, W. Tai, Z. Gu, *Nat. Commun.* **2014**, *5*, 3364.
[129] Y. Luqmani, *Med. Princ. Pract.* **2005**, *14*, 35.
[130] Y. Chen, H. Chen, J. Shi, *Mol. Pharmaceutics* **2014**, *11*, 2495.
[131] G. Szakács, J. K. Paterson, J. A. Ludwig, C. Booth-Genthe, M. M. Gottesman, *Nat. Rev. Drug Discovery* **2006**, *5*, 219.
[132] R. Y. Pelgrift, A. J. Friedman, *Adv. Drug Delivery Rev.* **2013**, *65*, 1803.
[133] A. Bernardos, E. Piacenza, F. Sancenón, M. Hamidi, A. Maleki, R. J. Turner, R. Martínez-Máñez, *Small* **2019**, *15*, 1900669.
[134] H. Deng, S. Grunder, K. E. Cordova, C. Valente, H. Furukawa, M. Hmadeh, F. Gándara, A. C. Whalley, Z. Liu, S. Asahina, *Science* **2012**, *336*, 1018.
[135] S. Yuan, L. Zou, J.-S. Qin, J. Li, L. Huang, L. Feng, X. Wang, M. Bosch, A. Alsalme, T. Cagin, *Nat. Commun.* **2017**, *8*, 15356.
[136] H. Huang, J.-R. Li, K. Wang, T. Han, M. Tong, L. Li, Y. Xie, Q. Yang, D. Liu, C. Zhong, *Nat. Commun.* **2015**, *6*, 8847.
[137] H. Nabipour, M. H. Sadr, G. R. Bardajee, *New J. Chem.* **2017**, *41*, 7364.
[138] B. Soltani, H. Nabipour, N. A. Nasab, *J. Inorg. Organomet. Polym. Mater.* **2018**, *28*, 1090.
[139] R. Riccò, W. Liang, S. Li, J. J. Gassensmith, F. Caruso, C. Doonan, P. Falcaro, *ACS Nano* **2018**, *12*, 13.
[140] Z. Liu, X. Xu, R. Tang, *Adv. Funct. Mater.* **2016**, *26*, 1862.
[141] M. B. Majewski, A. J. Howarth, P. Li, M. R. Wasielewski, J. T. Hupp, O. K. Farha, *CrystEngComm* **2017**, *19*, 4082.
[142] C. Doonan, R. Ricco, K. Liang, D. Bradshaw, P. Falcaro, *Acc. Chem. Res.* **2017**, *50*, 1423.
[143] K. Liang, R. Ricco, C. M. Doherty, M. J. Styles, S. Bell, N. Kirby, S. Mudie, D. Haylock, A. J. Hill, C. J. Doonan, *Nat. Commun.* **2015**, *6*, 7240.
[144] H. He, H. Han, H. Shi, Y. Tian, F. Sun, Y. Song, Q. Li, G. Zhu, *ACS Appl. Mater. Interfaces* **2016**, *8*, 24517.
[145] X. Wu, J. Ge, C. Yang, M. Hou, Z. Liu, *Chem. Commun.* **2015**, *51*, 13408.
[146] C. Zhang, L. Zhang, W. Wu, F. Gao, R. Li, W. Song, Z. Zhuang, C. Liu, X. Zhang, *Adv. Mater. 31*, **2019**, 1901179.
[147] W.-H. Chen, M. Vazquez-Gonzalez, A. Zoabi, R. Abu-Reziq, I. Willner, *Nat. Catal.* **2018**, *1*, 689.
[148] F.-S. Liao, W.-S. Lo, Y.-S. Hsu, C.-C. Wu, S.-C. Wang, F.-K. Shieh, J. V. Morabito, L.-Y. Chou, K. C.-W. Wu, C.-K. Tsung, *J. Am. Chem. Soc.* **2017**, *139*, 6530.
[149] W. Liang, H. Xu, F. Carraro, N. K. Maddigan, Q. Li, S. G. Bell, D. M. Huang, A. Tarzia, M. B. Solomon, H. Amenitsch, *J. Am. Chem. Soc.* **2019**, *141*, 2348.
[150] S. Dutta, J. Kim, P. Hsieh, Y. Hsu, Y. V. Kaneti, F. Shieh, Y. Yamauchi, K. C. Wu, *Small Methods* **2019**, *3*, 1900213.
[151] Y. Pan, H. Li, J. Farmakes, F. Xiao, B. Chen, S. Ma, Z. Yang, *J. Am. Chem. Soc.* **2018**, *140*, 16032.
[152] J. Bai, C. Peng, L. Guo, M. Zhou, *ACS Biomater. Sci. Eng.* **2019**, *5*, 6207.
[153] W. Liang, R. Ricco, N. K. Maddigan, R. P. Dickinson, H. Xu, Q. Li, C. J. Sumby, S. G. Bell, P. Falcaro, C. J. Doonan, *Chem. Mater.* **2018**, *30*, 1069.
[154] Z. Liang, Z. Yang, H. Yuan, C. Wang, J. Qi, K. Liu, R. Cao, H. Zheng, *Dalton Trans.* **2018**, *47*, 10223.
[155] C. Wang, G. Sudlow, Z. Wang, S. Cao, Q. Jiang, A. Neiner, J. J. Morrissey, E. D. Kharasch, S. Achilefu, S. Singamaneni, *Adv. Healthcare Mater.* **2018**, *7*, 1800950.
[156] F. Lyu, Y. Zhang, R. N. Zare, J. Ge, Z. Liu, *Nano Lett.* **2014**, *14*, 5761.
[157] Y. Chen, P. Li, J. A. Modica, R. J. Drout, O. K. Farha, *J. Am. Chem. Soc.* **2018**, *140*, 5678.
[158] T.-T. Chen, J.-T. Yi, Y.-Y. Zhao, X. Chu, *J. Am. Chem. Soc.* **2018**, *140*, 9912.
[159] G. Cheng, W. Li, L. Ha, X. Han, S. Hao, Y. Wan, Z. Wang, F. Dong, X. Zou, Y. Mao, *J. Am. Chem. Soc.* **2018**, *140*, 7282.
[160] M. A. Luzuriaga, R. P. Welch, M. Dharmarwardana, C. E. Benjamin, S. Li, A. Shahrivarkevishahi, S. Popal, L. Tuong, C. Creswell, J. J. Gassensmith, *ACS Appl. Mater. Interfaces* **2019**, *10*, 9740.
[161] Y. Zhang, F. Wang, E. Ju, Z. Liu, Z. Chen, J. Ren, X. Qu, *Adv. Funct. Mater.* **2016**, *26*, 6454.
[162] X. Zhong, Y. Zhang, L. Tan, T. Zheng, Y. Hou, X. Hong, G. Du, X. Chen, Y. Zhang, X. Sun, *J. Controlled Release* **2019**, *300*, 81.
[163] Y. Feng, H. Wang, S. Zhang, Y. Zhao, J. Gao, Y. Zheng, P. Zhao, Z. Zhang, M. J. Zaworotko, P. Cheng, *Adv. Mater.* **2019**, *31*, 1805148.
[164] S. Li, M. Dharmarwardana, R. P. Welch, C. E. Benjamin, A. M. Shamir, S. O. Nielsen, J. J. Gassensmith, *ACS Appl. Mater. Interfaces* **2018**, *10*, 18161.
[165] K. Liang, J. J. Richardson, J. Cui, F. Caruso, C. J. Doonan, P. Falcaro, *Adv. Mater.* **2016**, *28*, 7910.
[166] K. Liang, J. J. Richardson, C. J. Doonan, X. Mulet, Y. Ju, J. Cui, F. Caruso, P. Falcaro, *Angew. Chem., Int. Ed.* **2017**, *56*, 8510.
[167] S. Li, M. Dharmarwardana, R. P. Welch, Y. Ren, C. M. Thompson, R. A. Smaldone, J. J. Gassensmith, *Angew. Chem., Int. Ed.* **2016**, *55*, 10691.
[168] J.-M. Choi, S.-S. Han, H.-S. Kim, *Biotechnol. Adv.* **2015**, *33*, 1443.
[169] S. S. Nadar, V. K. Rathod, *Enzyme Microb. Technol.* **2018**, *108*, 11.
[170] G. Zhu, M. Zhang, Y. Bu, L. Lu, X. Lou, L. Zhu, *Chem. - Asian J.* **2018**, *13*, 2891.

[171] H. Ranji-Burachaloo, A. Reyhani, P. A. Gurr, D. E. Dunstan, G. G. Qiao, *Nanoscale* **2019**, *11*, 5705.
[172] R. H. Fang, A. V. Kroll, W. Gao, L. Zhang, *Adv. Mater.* **2018**, *30*, 1706759.
[173] H. Yan, D. Shao, Y. Lao, M. Li, H. Hu, K. W. Leong, *Adv. Sci.* **2019**, 1900605.
[174] K. Yang, K. Yang, S. Chao, J. Wen, Y. Pei, Z. Pei, *Chem. Commun.* **2018**, *54*, 9817.
[175] W. Jiang, H. Zhang, J. Wu, G. Zhai, Z. Li, Y. Luan, S. Garg, *ACS Appl. Mater. Interfaces* **2018**, *10*, 34513.
[176] Z. Wang, X. Tang, X. Wang, D. Yang, C. Yang, Y. Lou, J. Chen, N. He, *Chem. Commun.* **2016**, *52*, 12210.
[177] D. Xu, Y. You, F. Zeng, Y. Wang, C. Liang, H. Feng, X. Ma, *ACS Appl. Mater. Interfaces* **2018**, *10*, 15517.
[178] M.-R. Song, D.-Y. Li, F.-Y. Nian, J.-P. Xue, J.-J. Chen, *J. Mater. Sci.* **2018**, *53*, 2351.
[179] J. Fang, Y. Yang, W. Xiao, B. Zheng, Y.-B. Lv, X.-L. Liu, J. Ding, *Nanoscale* **2016**, *8*, 3259.
[180] R. Chen, J. Zhang, Y. Wang, X. Chen, J. A. Zapien, C.-S. Lee, *Nanoscale* **2015**, *7*, 17299.
[181] C. Zheng, Y. Wang, S. Z. F. Phua, W. Q. Lim, Y. Zhao, *ACS Biomater. Sci. Eng.* **2017**, *3*, 2223.
[182] G. Zhao, H. Wu, R. Feng, D. Wang, P. Xu, H. Wang, Z. Guo, Q. Chen, *ACS Omega* **2018**, *3*, 9790.
[183] J. S. Silva, J. Y. Silva, G. F. de Sá, S. S. Araújo, M. A. G. Filho, C. M. Ronconi, T. C. Santos, S. A. Júnior, *ACS Omega* **2018**, *3*, 12147.
[184] Y. Chen, J. Deng, F. Liu, P. Dai, Y. An, Z. Wang, Y. Zhao, *Adv. Healthcare Mater.* **2019**, *8*, 1900366.
[185] Z. Tian, X. Yao, K. Ma, X. Niu, J. Grothe, Q. Xu, L. Liu, S. Kaskel, Y. Zhu, *ACS Omega* **2017**, *2*, 1249.
[186] W. Zhou, L. Wang, F. Li, W. Zhang, W. Huang, F. Huo, H. Xu, *Adv. Funct. Mater.* **2017**, *27*, 1605465.
[187] H. Zhang, Q. Li, R. Liu, X. Zhang, Z. Li, Y. Luan, *Adv. Funct. Mater.* **2018**, *28*, 1802830.
[188] L. Wang, H. Guan, Z. Wang, Y. Xing, J. Zhang, K. Cai, *Mol. Pharmaceutics* **2018**, *15*, 2503.
[189] F. Liu, L. Lin, Y. Zhang, S. Sheng, Y. Wang, C. Xu, H. Tian, X. Chen, *Biomaterials* **2019**, *223*, 119470.
[190] J. Feng, W. Yu, Z. Xu, F. Wang, *Chem. Sci.* **2020**, *11*, 1649,.
[191] X. Jia, Z. Yang, Y. Wang, Y. Chen, H. Yuan, H. Chen, X. Xu, X. Gao, Z. Liang, Y. Sun, *ChemMedChem* **2018**, *13*, 400.
[192] Z. Zou, S. Li, D. He, X. He, K. Wang, L. Li, X. Yang, H. Li, *J. Mater. Chem. B* **2017**, *5*, 2126.
[193] Y.-C. Ma, Y.-H. Zhu, X.-F. Tang, L.-F. Hang, W. Jiang, M. Li, M. I. Khan, Y.-Z. You, Y.-C. Wang, *Biomater. Sci.* **2019**, *7*, 2740.
[194] F. Shu, D. Lv, X.-L. Song, B. Huang, C. Wang, Y. Yu, S.-C. Zhao, *RSC Adv.* **2018**, *8*, 6581.
[195] Z. Tian, X. Yao, Y. Zhu, *Microporous Mesoporous Mater.* **2017**, *237*, 160.
[196] R. Li, X. Ren, J. Zhao, X. Feng, X. Jiang, X. Fan, Z. Lin, X. Li, C. Hu, B. Wang, *J. Mater. Chem. A* **2014**, *2*, 2168.
[197] S. Gao, Y. Jin, K. Ge, Z. Li, H. Liu, X. Dai, Y. Zhang, S. Chen, X. Liang, J. Zhang, *Adv. Sci.* **2019**, *6*, 1902137.
[198] H.-J. Cai, T.-T. Shen, J. Zhang, C.-F. Shan, J.-G. Jia, X. Li, W.-S. Liu, Y. Tang, *J. Mater. Chem. B* **2017**, *5*, 2390.
[199] Y.-T. Qin, H. Peng, X.-W. He, W.-Y. Li, Y.-K. Zhang, *ACS Appl. Mater. Interfaces* **2019**, *11*, 34268.
[200] Z. Xie, X. Cai, C. Sun, S. Liang, S. Shao, S. Huang, Z. Cheng, M. Pang, B. Xing, A. A. A. Kheraif, *Chem. Mater.* **2019**, *31*, 483.
[201] A. R. Chowdhuri, D. Laha, S. Pal, P. Karmakar, S. K. Sahu, *Dalton Trans.* **2016**, *45*, 18120.
[202] M. He, J. Zhou, J. Chen, F. Zheng, D. Wang, R. Shi, Z. Guo, H. Wang, Q. Chen, *J. Mater. Chem. B* **2015**, *3*, 9033.
[203] J.-C. Yang, Y. Chen, Y.-H. Li, X.-B. Yin, *ACS Appl. Mater. Interfaces* **2017**, *9*, 22278.
[204] Y. Lv, D. Ding, Y. Zhuang, Y. Feng, J. Shi, H. Zhang, T.-L. Zhou, H. Chen, R.-J. Xie, *ACS Appl. Mater. Interfaces* **2018**, *11*, 1907.
[205] L. Su, Q. Wu, L. Tan, Z. Huang, C. Fu, X. Ren, N. Xia, Z. Chen, X. Ma, X. Lan, *ACS Appl. Mater. Interfaces* **2019**, *11*, 10520.
[206] J. Redfern, L. Geerts, J. W. Seo, J. Verran, L. Tosheva, L. H. Wee, *ACS Appl. Nano Mater.* **2018**, *1*, 1657.
[207] X. Xu, H. Chen, X. Wu, S. Chen, J. Qi, Z. He, S. Zou, L. Xie, K. Xu, H. Yuan, *Neural Plast.* **2018**, *2018*, 1.
[208] D. Peer, J. M. Karp, S. Hong, O. C. Farokhzad, R. Margalit, R. Langer, *Nat. Nanotechnol.* **2007**, *2*, 751.
[209] L. Brannon-Peppas, J. O. Blanchette, *Adv. Drug Delivery Rev.* **2012**, *64*, 206.
[210] X. Xu, J. Wu, Y. Liu, M. Yu, L. Zhao, X. Zhu, S. Bhasin, Q. Li, E. Ha, J. Shi, *Angew. Chem., Int. Ed.* **2016**, *55*, 7091.
[211] H. Meng, W. X. Mai, H. Zhang, M. Xue, T. Xia, S. Lin, X. Wang, Y. Zhao, Z. Ji, J. I. Zink, *ACS Nano* **2013**, *7*, 994.
[212] C. He, K. Lu, D. Liu, W. Lin, *J. Am. Chem. Soc.* **2014**, *136*, 5181.
[213] H. Yang, P. E. Kruger, S. G. Telfer, *Inorg. Chem.* **2015**, *54*, 9483.
[214] X. Wang, X. Li, X. Liang, J. Liang, C. Zhang, J. Yang, C. Wang, D. Kong, H. Sun, *J. Mater. Chem. B* **2018**, *6*, 1000.
[215] L. Tang, J. Shi, X. Wang, S. Zhang, H. Wu, H. Sun, Z. Jiang, *Nanotechnology* **2017**, *28*, 275601.
[216] Z. Jiang, H. Sun, Z. Qin, X. Jiao, D. Chen, *Chem. Commun.* **2012**, *48*, 3620.
[217] I. Imaz, M. Rubio-Martínez, L. García-Fernández, F. García, D. Ruiz-Molina, J. Hernando, V. Puntes, D. Maspoch, *Chem. Commun.* **2010**, *46*, 4737.
[218] Z. Tang, Y. Liu, M. He, W. Bu, *Angew. Chem., Int. Ed.* **2019**, *58*, 946.
[219] C. Zhang, W. Bu, D. Ni, S. Zhang, Q. Li, Z. Yao, J. Zhang, H. Yao, Z. Wang, J. Shi, *Angew. Chem., Int. Ed.* **2016**, *55*, 2101.
[220] C. Keum, S. Park, S. Lee, *Chem. - Asian J.* **2018**, *13*, 2641.
[221] L.-H. Fu, C. Qi, J. Lin, P. Huang, *Chem. Soc. Rev.* **2018**, *47*, 6454.
[222] P. Di Mascio, G. R. Martinez, S. Miyamoto, G. E. Ronsein, M. H. Medeiros, J. Cadet, *Chem. Rev.* **2019**, *119*, 2043.
[223] Q. Chen, M. G. Espey, A. Y. Sun, J.-H. Lee, M. C. Krishna, E. Shacter, P. L. Choyke, C. Pooput, K. L. Kirk, G. R. Buettner, *Proc. Natl. Acad. Sci. USA* **2007**, *104*, 8749.
[224] Y. Ma, J. Chapman, M. Levine, K. Polireddy, J. Drisko, Q. Chen, *Sci. Transl. Med.* **2014**, *6*, 222ra18.
[225] D. Sobot, S. Mura, P. Couvreur, *J. Mater. Chem. B* **2016**, *4*, 5078.
[226] Q. He, J. Shi, *Adv. Mater.* **2014**, *26*, 391.
[227] Y. Chen, H. Chen, J. Shi, *Expert Opin. Drug Delivery* **2014**, *11*, 917.
[228] J. E. Lee, N. Lee, T. Kim, J. Kim, T. Hyeon, *Acc. Chem. Res.* **2011**, *44*, 893.
[229] H. Wang, Y. Chen, H. Wang, X. Liu, X. Zhou, F. Wang, *Angew. Chem., Int. Ed.* **2019**, *58*, 7380.
[230] J.-J. Hu, Y.-J. Cheng, X.-Z. Zhang, *Nanoscale* **2018**, *10*, 22657.
[231] X. Huang, I. H. El-Sayed, W. Qian, M. A. El-Sayed, *J. Am. Chem. Soc.* **2006**, *128*, 2115.
[232] M. Soleymaniha, M. Shahbazi, A. R. Rafieerad, A. Maleki, A. Amiri, *Adv. Healthcare Mater.* **2019**, *8*, 1801137.
[233] H. Lin, Y. Wang, S. Gao, Y. Chen, J. Shi, *Adv. Mater.* **2018**, *30*, 1703284.
[234] C. Yang, Y. Chen, W. Guo, Y. Gao, C. Song, Q. Zhang, N. Zheng, X. Han, C. Guo, *Adv. Funct. Mater.* **2018**, *28*, 1706827.
[235] Z. Guo, S. Zhu, Y. Yong, X. Zhang, X. Dong, J. Du, J. Xie, Q. Wang, Z. Gu, Y. Zhao, *Adv. Mater.* **2017**, *29*, 1704136.
[236] M. A. Shahbazi, L. Faghfouri, M. P. A. Ferreira, P. Figueiredo, H. Maleki, F. Sefat, J. Hirovonen, H. A. Santos, *Chem. Soc. Rev.* **2020**, *49*, 1253.

[237] Y. Lyu, Y. Fang, Q. Miao, X. Zhen, D. Ding, K. Pu, *ACS Nano* **2016**, *10*, 4472.
[238] J. Yan, X. Zhang, Y. Liu, Y. Ye, J. Yu, Q. Chen, J. Wang, Y. Zhang, Q. Hu, Y. Kang, *Nano Res.* **2019**, *12*, 1313.
[239] Y. Chen, L. Wang, J. Shi, *Nano Today* **2016**, *11*, 292.
[240] S. Wei, Q. Wang, J. Zhu, L. Sun, H. Lin, Z. Guo, *Nanoscale* **2011**, *3*, 4474.
[241] A. Bansal, Y. Zhang, *Acc. Chem. Res.* **2014**, *47*, 3052.
[242] Z. Fan, H. Zhang, *Chem. Soc. Rev.* **2016**, *45*, 63.
[243] J. Zhou, Z. Lu, X. Zhu, X. Wang, Y. Liao, Z. Ma, F. Li, *Biomaterials* **2013**, *34*, 9584.
[244] Q. Tian, F. Jiang, R. Zou, Q. Liu, Z. Chen, M. Zhu, S. Yang, J. Wang, J. Wang, J. Hu, *ACS Nano* **2011**, *5*, 9761.
[245] D. Yang, G. Yang, S. Gai, F. He, G. An, Y. Dai, R. Lv, P. Yang, *Nanoscale* **2015**, *7*, 19568.
[246] Z. A. I. Mazrad, C. A. Choi, S. H. Kim, G. Lee, S. Lee, I. In, K.-D. Lee, S. Y. Park, *J. Mater. Chem. B* **2017**, *5*, 7099.
[247] S. Bhadra, D. Khastgir, N. K. Singha, J. H. Lee, *Prog. Polym. Sci.* **2009**, *34*, 783.
[248] H. Chen, Z. Liu, S. Li, C. Su, X. Qiu, H. Zhong, Z. Guo, *Theranostics* **2016**, *6*, 1096.
[249] X. Wang, Y. Ma, X. Sheng, Y. Wang, H. Xu, *Nano Lett.* **2018**, *18*, 2217.
[250] W.-L. Chiang, T.-T. Lin, R. Sureshbabu, W.-T. Chia, H.-C. Hsiao, H.-Y. Liu, C.-M. Yang, H.-W. Sung, *J. Controlled Release* **2015**, *199*, 53.
[251] M. Wang, *Polymers* **2016**, *8*, 373.
[252] X. Chen, M. Zhang, S. Li, L. Li, L. Zhang, T. Wang, M. Yu, Z. Mou, C. Wang, *J. Mater. Chem. B* **2017**, *5*, 1772.
[253] Y. Liu, P. Bhattarai, Z. Dai, X. Chen, *Chem. Soc. Rev.* **2019**, *48*, 2053.
[254] W. Guo, F. Wang, D. Ding, C. Song, C. Guo, S. Liu, *Chem. Mater.* **2017**, *29*, 9262.
[255] Y. Zhang, F. Huang, C. Ren, L. Yang, J. Liu, Z. Cheng, L. Chu, J. Liu, *ACS Appl. Mater. Interfaces* **2017**, *9*, 13016.
[256] J. Liu, L. Zhang, J. Lei, H. Shen, H. Ju, *ACS Appl. Mater. Interfaces* **2017**, *9*, 2150.
[257] L. Wang, M. Huo, Y. Chen, J. Shi, *Adv. Healthcare Mater.* **2018**, *7*, 1701156.
[258] Z. Xie, S. Liang, X. Cai, B. Ding, S. Huang, Z. Hou, P. Ma, Z. Cheng, J. Lin, *ACS Appl. Mater. Interfaces* **2019**, *11*, 31671.
[259] H. Lin, Y. Chen, J. Shi, *Chem. Soc. Rev.* **2018**, *47*, 1938.
[260] B. Yang, Y. Chen, J. Shi, *Adv. Mater. 31*, **2019**, 1901778.
[261] X. Wang, D. Miao, X. Liang, J. Liang, C. Zhang, J. Yang, D. Kong, C. Wang, H. Sun, *Biomater. Sci.* **2017**, *5*, 658.
[262] H. Chen, J. Yang, L. Sun, H. Zhang, Y. Guo, J. Qu, W. Jiang, W. Chen, J. Ji, Y. Yang, *Small 15*, **2019**, 1903880.
[263] C. A. Lemley, D. P. Han, *Retina* **2007**, *27*, 662.
[264] M. Ramappa, A. B. Majji, S. I. Murthy, P. K. Balne, S. Nalamada, C. Garudadri, A. Mathai, U. Gopinathan, P. Garg, *Ophthalmology* **2012**, *119*, 564.
[265] Y. Xie, Y. Liu, J. Yang, Y. Liu, F. Hu, K. Zhu, X. Jiang, *Angew. Chem., Int. Ed.* **2018**, *57*, 3958.
[266] J. Xie, S. Lee, X. Chen, *Adv. Drug Delivery Rev.* **2010**, *62*, 1064.
[267] H. Zhang, X.-T. Tian, Y. Shang, Y.-H. Li, X.-B. Yin, *ACS Appl. Mater. Interfaces* **2018**, *10*, 28390.
[268] W. Zhu, Y. Yang, Q. Jin, Y. Chao, L. Tian, J. Liu, Z. Dong, Z. Liu, *Nano Res.* **2019**, *12*, 1307.
[269] H. Zhang, Q. Zhang, C. Liu, B. Han, *Biomater. Sci.* **2019**, *7*, 1696.
[270] H. Zhao, G. Shu, J. Zhu, Y. Fu, Z. Gu, D. Yang, *Biomaterials* **2019**, *217*, 119332.
[271] D. E. Dolmans, D. Fukumura, R. K. Jain, *Nat. Rev. Cancer* **2003**, *3*, 380.
[272] M. Lismont, L. Dreesen, S. Wuttke, *Adv. Funct. Mater.* **2017**, *27*, 1606314.
[273] G. Yang, L. Xu, Y. Chao, J. Xu, X. Sun, Y. Wu, R. Peng, Z. Liu, *Nat. Commun.* **2017**, *8*, 902.
[274] J. Liu, P. Du, T. Liu, B. J. C. Wong, W. Wang, H. Ju, J. Lei, *Biomaterials* **2019**, *192*, 179.
[275] Z. He, Y. Xiao, J.-R. Zhang, P. Zhang, J.-J. Zhu, *Chem. Commun.* **2018**, *54*, 2962.
[276] Q. Sun, H. Bi, Z. Wang, C. Li, C. Wang, J. Xu, D. Yang, F. He, S. Gai, P. Yang, *ACS Appl. Mater. Interfaces* **2019**, *11*, 36347.
[277] L. Zhang, S.-S. Wan, C.-X. Li, L. Xu, H. Cheng, X.-Z. Zhang, *Nano Lett.* **2018**, *18*, 7609.
[278] S. Lu, D. Tu, P. Hu, J. Xu, R. Li, M. Wang, Z. Chen, M. Huang, X. Chen, *Angew. Chem., Int. Ed.* **2015**, *54*, 7915.
[279] J. Liu, S. Z. Qiao, J. S. Chen, X. W. D. Lou, X. Xing, G. Q. M. Lu, *Chem. Commun.* **2011**, *47*, 12578.
[280] Y. Chang, Y. Cheng, Y. Feng, H. Jian, L. Wang, X. Ma, X. Li, H. Zhang, *Nano Lett.* **2018**, *18*, 886.
[281] L. Lin, X. Yang, Z. Zhou, Z. Yang, O. Jacobson, Y. Liu, A. Yang, G. Niu, J. Song, H. Yang, *Adv. Mater.* **2017**, *29*, 1606681.
[282] X. Deng, S. Liang, X. Cai, S. Huang, Z. Cheng, Y. Shi, M. Pang, P. Ma, J. Lin, *Nano Lett.* **2019**, *19*, 6772.